

NASA CR 182, 107

NASA CR-182-107

NASA-CR-182107
19880014446

ARCJET THRUSTER RESEARCH AND TECHNOLOGY

PHASE I FINAL REPORT

NAS 3-24631

87-R-1175

Prepared for:

NASA Lewis Research Center
21000 Brook Park Road
Cleveland, OH 44135

LIBRARY COPY

APR 25 1988

September 30, 1987

LANGLEY RESEARCH CENTER
LIBRARY NASA
HAMPTON, VIRGINIA



Redmond, Washington

ROCKET RESEARCH COMPANY



NF00904

ARCJET THRUSTER RESEARCH AND TECHNOLOGY

Phase I Final Report

NAS 3-24631

87-R-1175

Prepared for:

NASA Lewis Research Center
21000 Brook Park Road
Cleveland, OH 44135

September 30, 1987

Prepared by:



Steven C. Knowles
Project Manager

Approved by:



W. W. Smith, Director
Electric Propulsion

KEM#43

N98-23830 #

FORWARD

The work described in this report was performed by Rocket Research Company under Phase I of contract NAS3-24631 for the Lewis Research Center of the National Aeronautics and Space Administration. The reporting period covers the time between September, 1985 and March, 1987. Dr. Frank M. Curran of NASA was the program technical manager.

The work was accomplished under the direction of W. W. Smith and S. C. Knowles. The persons having principle research responsibilities were:

Arcjet Design:	N. R. Arnot D. S. Stenseth J. E. Philp
Materials:	A. W. Voigt
VNAP2 Nozzle Analysis:	D. K. Carlson
Reaction Kinetics Modelling:	M. A. Simon
Vortex Analysis:	C. R. Roberts
Thermal Modelling:	F. R. Schwam K. W. Arasim M. A. Simon
Testing:	M. S. Hiatt M. A. Simon S. C. Knowles
PCU Development:	M. S. Hiatt S. C. Knowles

TABLE OF CONTENTS

	<u>PAGE</u>
1.0 SUMMARY	1-1
2.0 INTRODUCTION	2-1
3.0 PROGRESS	3-1
3.1 Analysis	3-1
3.2 Design/Fabrication/Assembly	3-17
3.3 Operational/Lifetime Testing	3-23
3.4 Performance Testing	3-32
3.5 PCU Development	3-56
4.0 CONCLUSIONS	4-1
5.0 FUTURE WORK	5-1
REFERENCES	R-1
APPENDIX A	A-1
APPENDIX B	B-1
APPENDIX C	C-1

FIGURES

	<u>PAGE</u>
1-1 Phase 1/Arcjet Technology Progress Assessment	1-2
1-2 Phase 1/Program Highlights	1-4
2-1 Phase 1/Task Interrelationships	2-2
2-2 Arcjet Analysis Summary	2-4
3-1 Arcjet Energy Balance Model Arcjet III	3-3
3-2 VNAP2 Inlet Conditions	3-5
3-3 VNAP2 Output, Case 1	3-6
3-4 VNAP2 Results, Cases 1, 3, and 4	3-7
3-5 VNAP2 Results, Cases 2, 5, and 6	3-8
3-6 CREK1D N ₂ H ₄ Data	3-11
3-7 Arcjet TMG Model	3-15
3-8 TMG Arcjet Surface Temperature Profiles	3-16
3-9 Low Power Hydrazine Arcjet	3-19
3-10 N ₂ H ₄ Arcjet Design	3-20
3-11 Typical Geometries	3-22
3-12 Propellant System Schematic	3-24
3-13 Flow Meter Calibration	3-26
3-14 N ₂ H ₄ Analysis Report	3-27
3-15 Pressure Pulse Startup	3-30
3-16 Cathode and Anode, 8 Hour Steady State Test 2.1	3-33
3-17 W/25 Re Anode, Test 5.2	3-34
3-18 Mo/41 Re Anode, Test 6.1	3-35
3-19 EP Test Cell 10	3-36
3-20 Null Balance Thrust Stand	3-38
3-21 Specific Impulse vs. Power/Flow Rate, Test 10.2	3-40
3-22 Specific Impulse vs. Chamber Pressure, Test 10.2	3-41
3-23 Thrust vs. Power/Flow Rate, Test 10.2	3-42
3-24 N ₂ H ₄ Arcjet Performance Curve	3-43

FIGURES (Continued)

	<u>PAGE</u>
3-25 Voltage vs. Current, Tests 10.2, 16.2 and 18.4	3-44
3-26 Voltage vs. Current, Tests 9.2, 17.1 and 18.4	3-46
3-27 Efficiency vs. Power/Flow Rate, Test 18.4	3-47
3-28 Efficiency vs. Chamber Pressure, Test 18.4	3-48
3-29 Efficiency vs. Power/Flow Rate, Tests 14.2 and 18.4	3-49
3-30 Efficiency vs. Power/Flow Rate, Test 10.2	3-51
3-31 Efficiency vs. Current/Flow Rate, Test 18.4	3-52
3-32 Thermal Efficiency vs. Current, Test 10.2	3-54
3-33 Thermal Efficiency vs. Current, Test 18.4	3-55
3-34 DC/Dynamic Arcjet Characteristics	3-57
3-35 Simplified PCU/Arcjet System	3-59
3-36 PCU Block Diagram	3-62
3-37 N_2H_4 Arcjet/PCU Breakdown Data	3-64
3-38 PCU Startup Trace	3-66
3-39 PCU Startup Ramp Behavior	3-67
3-40 Steady State Current/Voltage Traces	3-69
3-41 PCU Current Traces	3-70
3-42 PCU Current Traces	3-71
5-1 Phase II/Task Breakdown	5-2

TABLES

	<u>PAGE</u>
3-1 Arcjet Analyses	3-1
3-2 VNAP2 Nozzle Profiles	3-2
3-3 Reaction Rate Data	3-10
3-4 Materials List	3-21
3-5 Instrumentation List	3-28
3-6 Materials Test Summary	3-31
3-7 Performance Test Configurations	3-39
3-8 Breadboard Arcjet Laboratory PCU Specification	3-61

1.0 SUMMARY

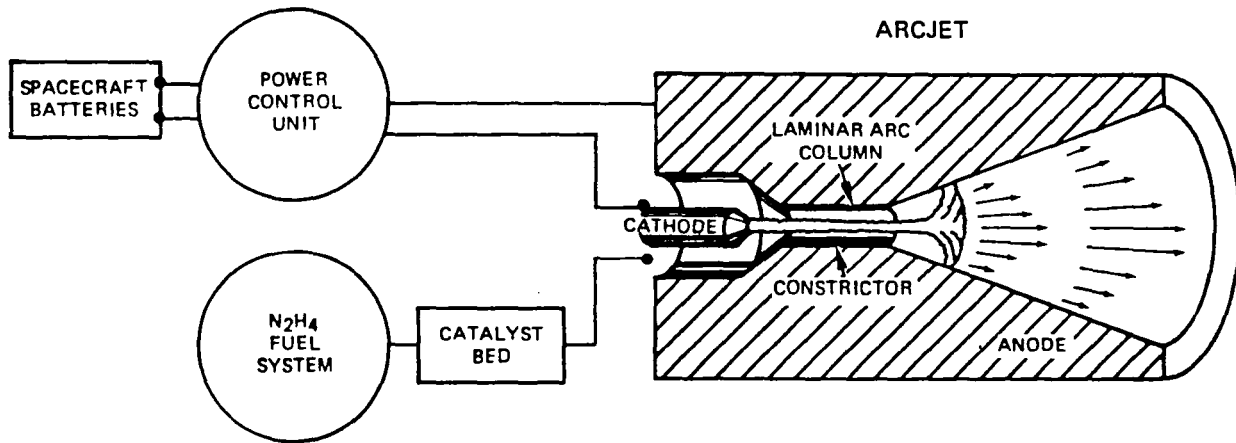
This report documents the results of work performed at Rocket Research Company during Phase I of contract NAS 3-24631, under the technical direction of the NASA Lewis Research Center. The overall objectives of this two phase program are to identify technical problem areas for a long life, high efficiency and performance, storable propellant arcjet, to conduct the research necessary to develop solutions to these problems, and to demonstrate technology readiness for practical application. There were two principle objectives for Phase I:

1. Evaluate analytically and experimentally the operation, performance, and lifetime of arcjet thrusters operating between 0.5 and 3.0 kW with catalytically decomposed hydrazine (N_2H_4).
2. Begin development of the requisite power control unit (PCU) technology.

These objectives were fully met by the Phase I efforts, as summarized in Figure 1-1. The results obtained brought the N_2H_4 arcjet much closer to being a near term flight ready technology.

Fundamental analyses were performed of the arcjet nozzle, the gas kinetic reaction effects, the thermal environment, and the arc stabilizing vortex. The VNAP2 flow code was used to analyze arcjet nozzle performance with non-uniform entrance profiles. Viscous losses become dominant beyond expansion ratios of 50:1 because of the low Reynolds numbers (< 800). A survey of vortex phenomena and analysis techniques identified viscous dissipation and vortex breakdown as two flow instabilities that could affect arcjet operation. Analysis of these effects is very complex, and was beyond the scope of this program. The gas kinetics code CREKID was exercised to study the gas kinetics of high temperature N_2H_4 decomposition products. The arc/gas energy transfer is a non-equilibrium process because of the reaction rate constants and the short gas residence times (≈ 1 microsecond). A thermal analysis code was used to guide design work and to provide a means to back out power losses at the anode fall based on test thermocouple data. The low flow rate and large thermal masses made optimization of a regenerative heating scheme unnecessary.

Phase I Arcjet Technology Progress Assessment



TECHNOLOGY ISSUES, BEGINNING OF PHASE I

- IS AN N_2H_4 ARCJET FEASIBLE?
- WILL EXISTING N_2H_4 GRADES BE ACCEPTABLE?
- CAN THE N_2H_4 ARCJET BE NONEROSIVELY & RELIABLY STARTED?
- WILL PERFORMANCE BE ACCEPTABLE?
- CAN THE ARCJET OPERATE AT LOW (<2 kW) POWER?
- WHAT ROLE DOES POWER CONDITIONING PLAY?
- IS THE ARCJET SYSTEM COMPATIBLE WITH EXISTING N_2H_4 PROPULSION SYSTEMS?
- WHAT IS THE DOMINANT ISSUE FOR FLIGHT APPLICATION?

STATUS, END OF PHASE I

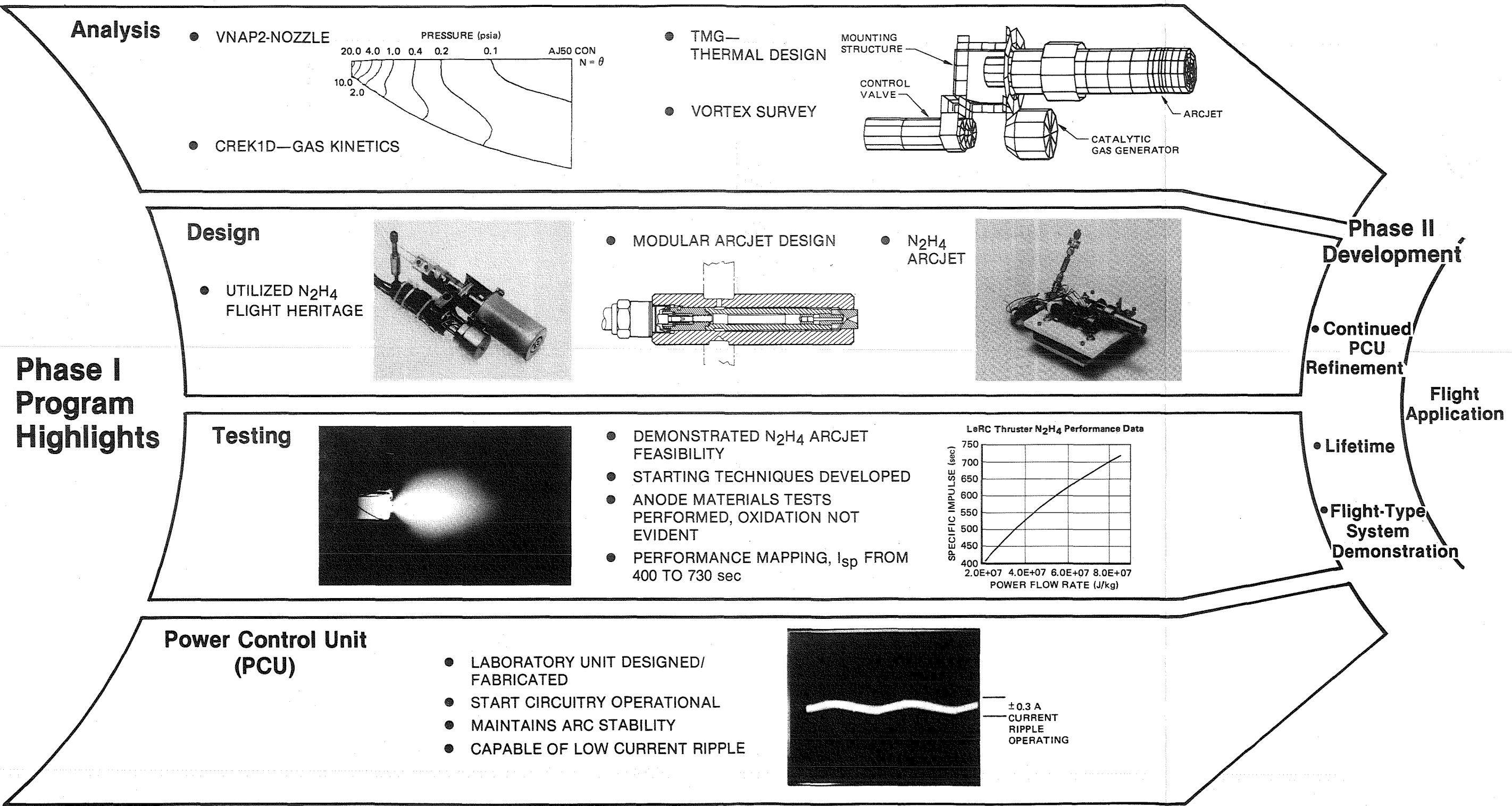
- YES. STABLE OPERATION DEMONSTRATED FOR MANY CONFIGURATIONS.
- YES. NO OXIDATION SEEN WITH MIL-SPEC N_2H_4 .
- YES. TWO TECHNIQUES DEMONSTRATED
- YES. I_{sp} FROM 400 TO 730 SECONDS MEASURED
- YES. OPERATED FROM 1,000 TO 3,000 W.
- SIGNIFICANT. PCU AFFECTS RELIABLE STARTS. STEPS UP VOLTAGE, MAINTAINS DYNAMIC ARC STABILITY.
- YES. CAN USE FLIGHT-PROVEN N_2H_4 TECHNOLOGY, POWER CONDITIONING REQUIREMENTS ARE MODERATE.
- LIFETIME. PHASE II EFFORTS FOCUSED ON THIS ISSUE

A N_2H_4 arcjet was designed and fabricated that incorporated a flight qualified solenoid valve and catalytic gas generator from the Augmented Catalytic Thruster (ACT), which is a resistojet. The arcjet design was highly modular to allow parametric studies, to maintain very tight electrode tolerances, and to permit rapid assembly and disassembly.

Three phases of testing were completed. During the first period of operational tests, arc stability was demonstrated, a non-erosive startup technique was developed, and anode material compatibility with N_2H_4 was shown to not be affected by the approximately 1% H_2O content of the propellant. The thruster performance was mapped during a second phase of testing. Specific impulse levels from 400 to 730 sec. were measured. For a given ratio of input power to flow rate (P/\dot{m}), the performance was relatively insensitive to the exact electrode geometry and flow field. The efficiency is principally determined by frozen flow effects, followed by thermal and viscous nozzle losses, which are of comparable magnitude, and by nozzle expansion losses. Overall efficiency varied little with P/\dot{m} because of competing effects. During the third test sequence, a laboratory switch mode PCU was developed under this contract by Space Power, Inc. The unit was used to study arcjet/PCU stability and startup. Starting voltages at steady state propellant flow pressures were up to 2000 V. Both DC and dynamic stability criteria were identified.

Figure 1-2 summarizes the program highlights.

Phase II efforts presently underway are resolving key issues for multi-hundred hour lifetimes, are continuing to investigate arcjet/PCU interactions, and will demonstrate duty cycle N_2H_4 arcjet/PCU operation in a simulated flight mode for lifetimes consistent with initial applications.



A N_2H_4 arcjet was designed and fabricated that incorporated a flight qualified solenoid valve and catalytic gas generator from the Augmented Catalytic Thruster (ACT), which is a resistojet. The arcjet design was highly modular to allow parametric studies, to maintain very tight electrode tolerances, and to permit rapid assembly and disassembly.

Three phases of testing were completed. During the first period of operational tests, arc stability was demonstrated, a non-erosive startup technique was developed, and anode material compatibility with N_2H_4 was shown to not be affected by the approximately 1% H_2O content of the propellant. The thruster performance was mapped during a second phase of testing. Specific impulse levels from 400 to 730 sec. were measured. For a given ratio of input power to flow rate (P/\dot{m}), the performance was relatively insensitive to the exact electrode geometry and flow field. The efficiency is principally determined by frozen flow effects, followed by thermal and viscous nozzle losses, which are of comparable magnitude, and by nozzle expansion losses. Overall efficiency varied little with P/\dot{m} because of competing effects. During the third test sequence, a laboratory switch mode PCU was developed under this contract by Space Power, Inc. The unit was used to study arcjet/PCU stability and startup. Starting voltages at steady state propellant flow pressures were up to 2000 V. Both DC and dynamic stability criteria were identified.

Figure 1-2 summarizes the program highlights.

Phase II efforts presently underway are resolving key issues for multi-hundred hour lifetimes, are continuing to investigate arcjet/PCU interactions, and will demonstrate duty cycle N_2H_4 arcjet/PCU operation in a simulated flight mode for lifetimes consistent with initial applications.

2.0 INTRODUCTION

Low power arcjet technology offers a promising and heretofore unexplored path to achieving a high performance on-orbit propulsion option. Substantial performance benefits to both near-term and far-term space missions with large ΔV attitude control and stationkeeping requirements are foreseen. By effectively containing a high temperature arc plasma through gas dynamic effects and geometric design, the arcjet is capable of exceeding previous specific impulse levels of thruster control systems by 200 to 400 seconds. This increased performance can provide valuable propellant mass savings to satellite missions and in some cases may be mission enabling.

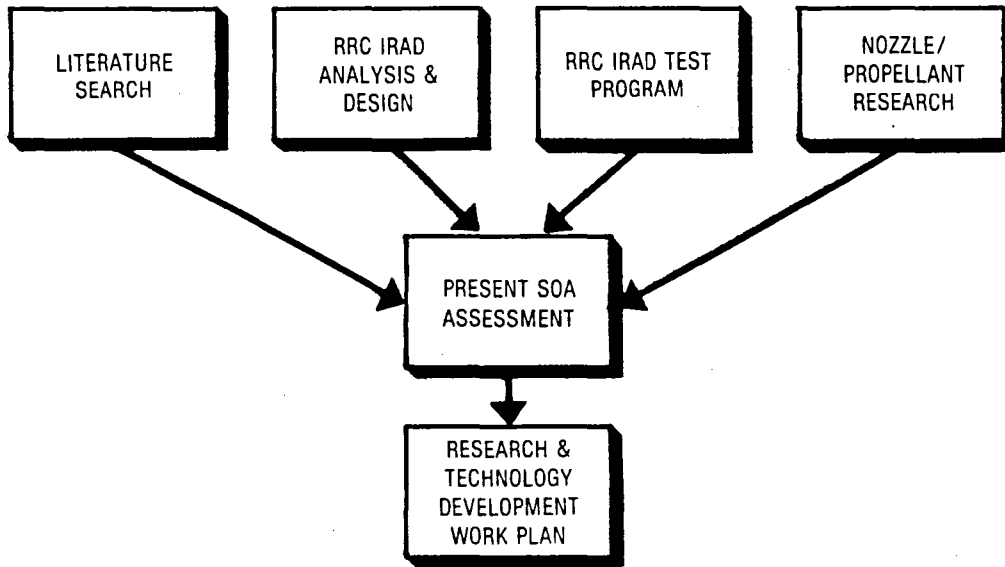
Previous development efforts in the 1960's focused principally on the 30 kw power level for orbit transfer. Only a small amount of work was done at the 1-2 kw power level with H_2 and NH_3 ¹. The measured performance was to over 1000 seconds specific impulse with H_2 . A lifetime test of 150 hours was successfully completed at 2 kw but documentation on this test, conducted in 1963, was difficult to obtain. More recent increases in spacecraft power availability and in the stationkeeping and attitude control requirements for larger satellites have increased the need for storable propellant, low power arcjet technology.

The arcjet is an electrothermal device that transfers electrical energy into a gaseous propellant through direct contact with an electric arc passing through the throat of the nozzle. The arc is initiated at the negative cathode, passes through the constrictor, where it is stabilized by vortex and wall induced pressure forces, then enters the nozzle and attaches to the nozzle wall. Steep enthalpy and velocity profiles exist at the constrictor exit, where centerline temperatures may be as high as 30000 K. These profiles result in bulk average temperatures that exceed materials limits. Because the hottest gases are contained in a cooler outer flow, the arcjet can function for long periods without significant erosion.

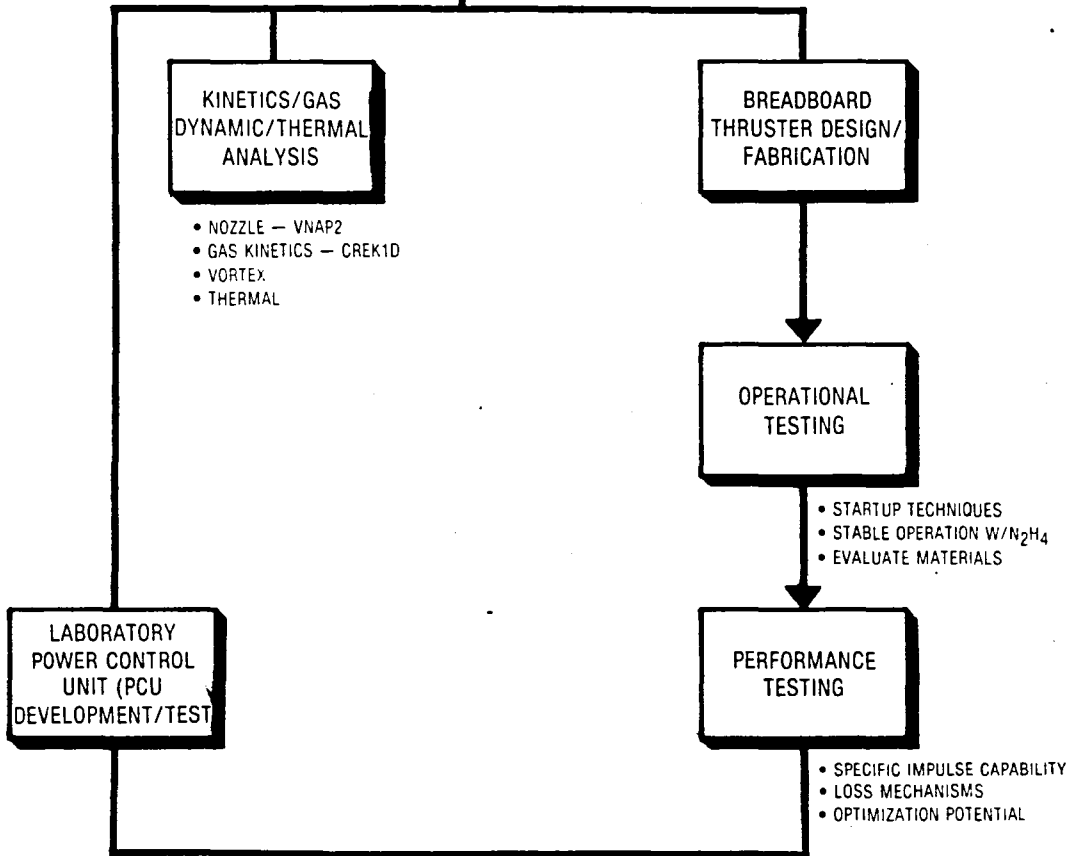
Flight application of the N_2H_4 arcjet system requires multi-hundred hour lifetimes, adequate performance, a reliable restart capability, and an efficient power control unit to interface between the spacecraft batteries and the arcjet. The analytical and experimental program conducted under Phase I was structured to demonstrate or move towards demonstration of these capabilities, and to improve the fundamental understanding of arcjet physics. Figure 2-1 shows the Phase I task interrelationships.

PHASE I Task Interrelationships

TASK 1



TASK 2



PHASE II

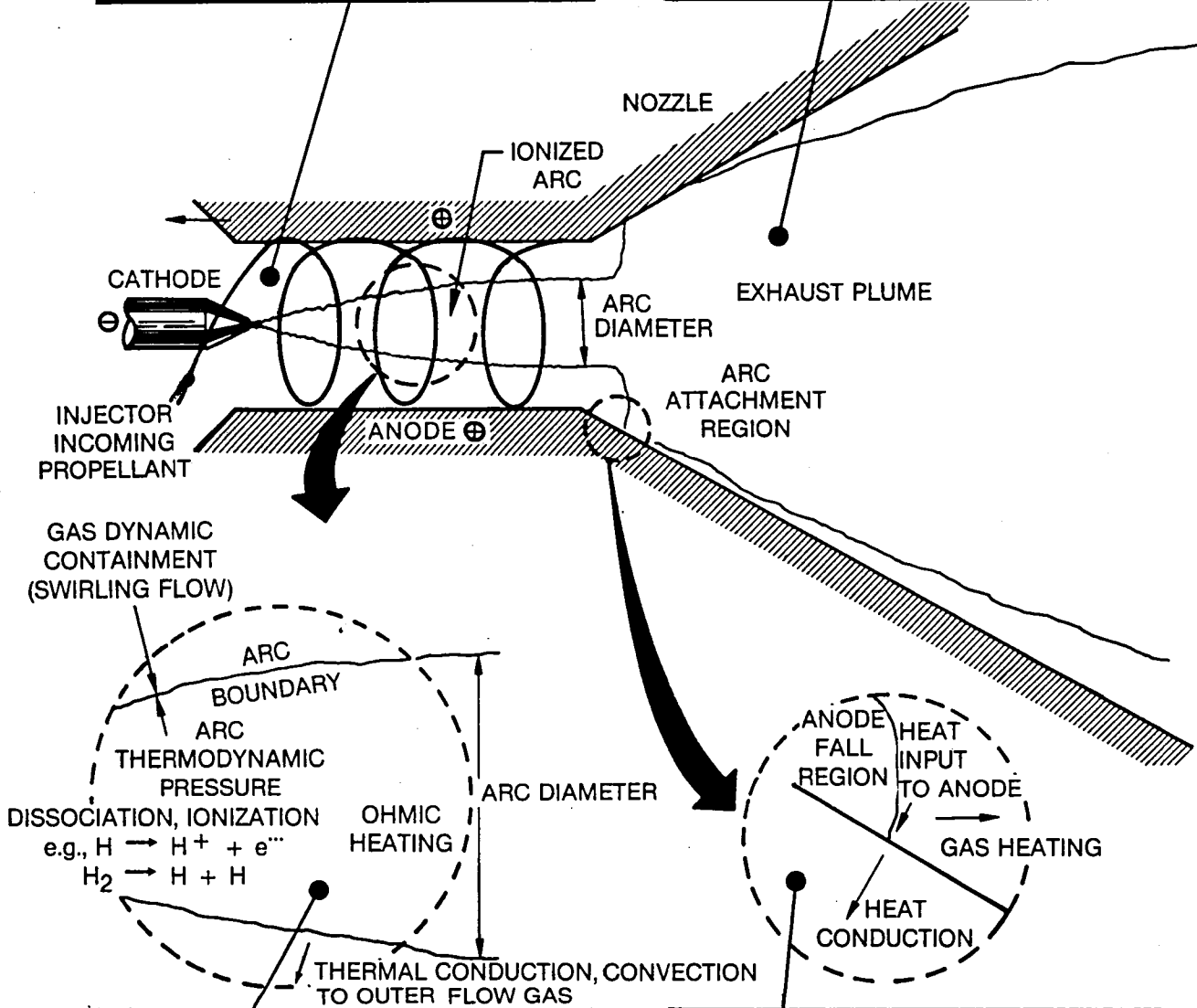
Analyses of gas dynamic, gas kinetic, and thermal effects were performed, as summarized in Figure 2-2. A breadboard N_2H_4 arcjet thruster was designed and fabricated. Three phases of testing were successfully completed with this unit. Operational testing focused on the startup process, arc stability, and materials evaluation. Performance testing was conducted to map the specific impulse and efficiency of several configurations over a broad power range, and to isolate the energy loss mechanisms. A third testing phase was completed with a laboratory PCU that was developed during the program. The PCU circuitry was similar to what might be expected for a flight unit, in contrast to the commercial supply and ballast resistor used for previous testing. Arcjet/PCU stability and startup capabilities were demonstrated.

As the detailed results in the following sections demonstrate, the N_2H_4 arcjet technology base has grown substantially during this phase of the program, and with it, the promise for near term flight application. Continuing efforts under Phase II are resolving lifetime issues for multi-hundred hour operation, are continuing to investigate the arcjet/PCU system, and will demonstrate a simulated flight capability through duty cycle operation.

Arcjet Analysis Summary

- Vortex — Literature Survey
 - Arc stabilization
 - Injector design
 - Startup

- Nozzle — VNAP2
 - Nonuniform profile affects
 - Nozzle performance
 - Optimized design



- Gas Kinetics — CREK1D
 - Arc gas heat transfer
 - Nonequilibrium effects
 - Frozen flow losses

- Thermal — TMG
 - Thermal design
 - Anode arc attachment heat losses

3.0 PROGRESS

3.1 ANALYSIS

Several analysis tasks were performed to better understand fundamental arcjet physics, and to guide design and testing. Four areas were addressed as summarized in Table 3-1. An extensive literature evaluation was also completed.

Table 3-1
ARCJET ANALYSES

Analysis	Method	Results
Nozzle Performance	VNAP2 code, 2-D Navier-Stokes model, parametric study of nonuniform effects and nozzle profiles.	Viscous losses dominate beyond $\epsilon = 50$, low Reynold's numbers (< 800), larger nozzle angles are more efficient.
Reaction Kinetics	CREK1D, gas phase chemical kinetics code.	Arcjet energy transfer is a chemically non-equilibrium process -- short gas residence times compared to reaction rate constants.
Vortex	Literature review	Vortex flow instabilities possible -- recirculation, viscous dissipation, numerical analysis very complex and beyond present program scope.
Thermal	Thermal Model Generator (TMG) code.	Established design margins for temperature sensitive components (solenoid valve, seals), provided estimates of thermal losses by backing out anode power deposition.

3.1.1 Literature Search

More than 300 literature sources on arcjet and related technologies were reviewed. The major technical issues of interest were:

- Design concepts
- Test data
- Nozzle design
- Analytical modeling

- Materials
- Nonequilibrium effects
- Startup techniques
- Experimental techniques
- Transport/thermodynamic data
- Electrode phenomena

These sources were used to help focus the analysis and testing tasks.

3.1.2 VNAP2 Nozzle Analysis

Analysis of low power arcjet nozzle performance was performed using the VNAP2 computer code². VNAP2 solves the two dimensional, time-dependent, compressible Navier-Stokes equations for turbulent, laminar, inviscid, steady, and unsteady flows. The nozzle inlet conditions were calculated using ARCJET III, RRC's arc energy balance code. This is an in-house computer model that solves the coupled energy, momentum and continuity equations within the constrictor of the arcjet using a finite difference scheme. The model is summarized in Figure 3-1. It calculates axisymmetric enthalpy and velocity profiles as energy is added through ohmic heating from the arc. The calculated constrictor exit conditions are then input into VNAP2 at the nozzle entrance.

The six nozzle contours listed in Table 3-2 were analyzed using the same inlet conditions. The objective was to see if significant performance improvements could be expected by optimizing the arcjet nozzle. VNAP2 takes initially prescribed radial temperature, density, and velocity profiles and expands in space and time the flow through a user defined grid pattern. The program also requires the user to define the back pressure at the nozzle exit.

Table 3-2
VNAP2 NOZZLE PROFILES

Number	Nozzle	Half Angle	Area Ratio
1	Conical	20°	20
2	Conical	20°	50
3	Conical	20°	100
4	Conical	10°	50
5	Conical	30°	50
6	Contour	--	50

ARC ENERGY BALANCE MODEL ARCJET III

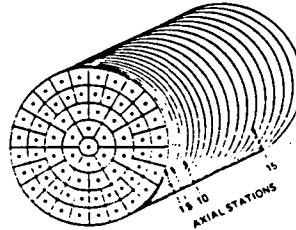
FINITE DIFFERENCE FORMULATION

COUPLED ENERGY, MOMENTUM, CONTINUITY EQUATIONS

$$\frac{\rho u}{\partial z} \frac{\partial h_t}{\partial z} + \frac{\rho v}{\partial r} \frac{\partial h_t}{\partial r} = \frac{i^2 \sigma}{(f_A \sigma dA)^2} + \frac{1}{r} \frac{\partial \psi}{\partial r} + \frac{\partial^2 \psi}{\partial r^2} - \text{radiation}$$

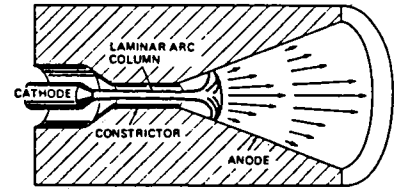
$$\rho u \frac{\partial u}{\partial z} + \frac{\rho v}{\partial r} \frac{\partial u}{\partial r} = - \frac{dp}{dz} + \frac{1}{r} \frac{\partial}{\partial r} \left(r \mu \frac{\partial u}{\partial r} \right)$$

$$\int_A \rho u dA = \dot{m}; \quad \psi = \int k dT$$



11163-78
 • BASED ON WATSON/PEGOT MODEL (NASA TN - D - 4042)

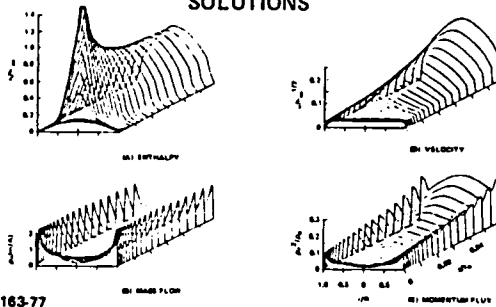
OPERATING CONDITIONS



33004-80

- INLET PROFILES
- CURRENT
- CONSTRUCTOR SIZING
- PRESSURE
- PROPELLANT
- MASS FLOW RATE
- WALL CONDITIONS

NUMERICAL MODEL SOLUTIONS



11163-77

NUMERICAL MODEL SOLUTIONS

- PROFILE DEVELOPMENT
- EXIT ENTHALPY
- WALL HEAT FLUX
- PERFORMANCE IMPACT OF I, \dot{m} , P, T_{wall} , INLET CONDITIONS, CONSTRUCTOR L&D
- CHOKE POINT
- ELECTRIC FIELD STRENGTH
- RADIATION FLUX

VNAP2 first solves the nozzle expansion problem using isentropic relations. This solution gives an initial (P), density (ρ), and temperature (T) profile in the nozzle. The isentropic solution is then used as an initial estimate for the solution of the Navier-Stokes and continuity equations at each of the predefined nodes at time "t", and in turn generates another set of profiles in the nozzle. These will then be used to solve the same equations, except at $t + \Delta t$. The program will continue to do this at progressive locations in time. The user may compare profiles at different iteration points in order to determine if VNAP2 has converged upon a solution. A solution is obtained when there is little or no change between the P, ρ and T profiles generated at successive iterations.

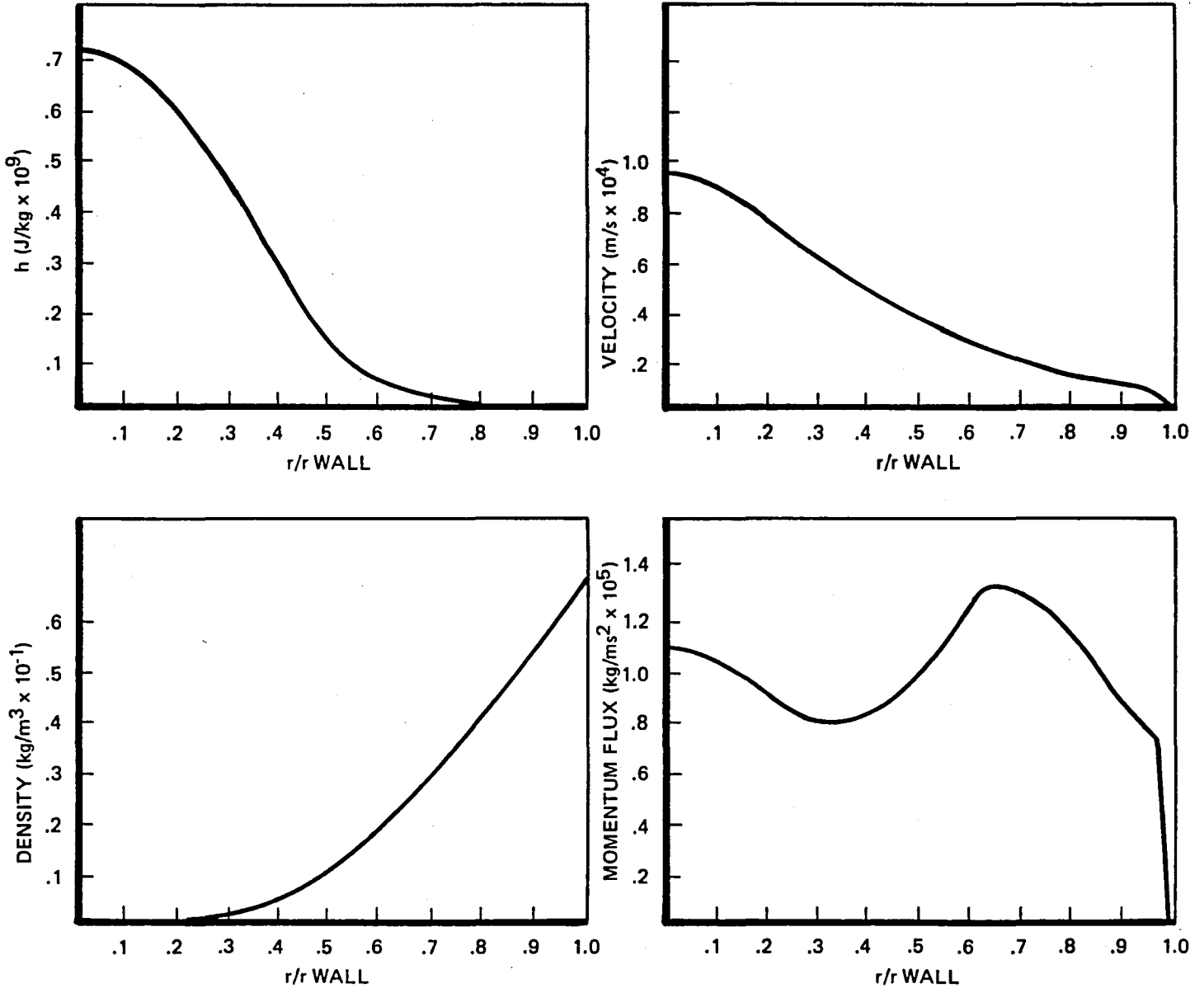
Convergence is a function of the specified boundary conditions of the initial estimate of the solution. The steep profiles of the arcjet made convergence more difficult than with a more uniform flow. A method was developed by which the number of iterations was reduced significantly by using a better initial estimate of the solution that is derived from previous VNAP2 runs. For example, a 50:1, 10° conical nozzle solution from VNAP2 (which would have taken 8,000 iterations to solve), is then "stretched" by a proportioning scheme to give an initial estimate for a 100:1, 10° nozzle. By using this method, iterations are cut by up to 400%.

Identical inlet conditions were used for each run. The initial enthalpy, velocity, density, and momentum flux profiles based on a 2 kW NH_3 arcjet operating conditions are shown in Figure 3-2. The flow is fully laminar. Each parameter varies by an order of magnitude across the constrictor.

Figure 3-3 gives the density, pressure, and temperature profiles for the first of the six nozzles analyzed. The remainder are found in Appendix B. Figures 3-4 and 3-5 plot the calculated specific impulse as a function of area ratio. A comparison of cases 1, 2, and 3 indicates that viscous losses begin to dominate expansion gains for expansion ratios greater than about 50:1 for a 20° half-angle. However, all three specific impulse values are within 15 sec of each other for only a 2 to 3% total variation.

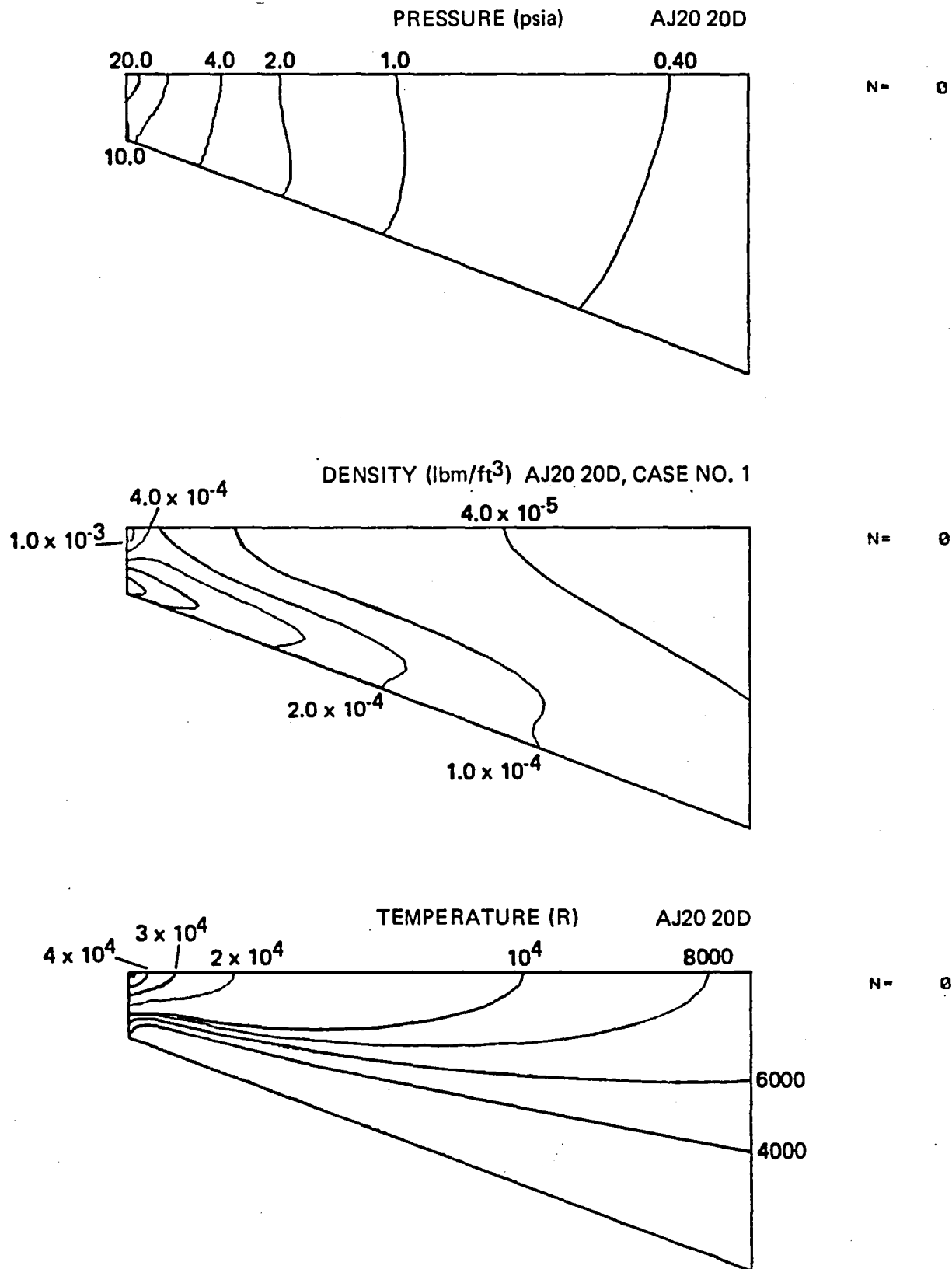
Cases 2, 4, and 5 show that the half-angle has a significant effect on performance and that the onset of dominant viscous losses is more marked at smaller angles. The 30° nozzle shows a 60 sec, or 11%, gain over the 10° nozzle. Eventually, cosine losses will dominate the decrease in viscous losses caused by the reduced nozzle length.

VNAP2 INLET CONDITIONS CALCULATED WITH ARCJET III

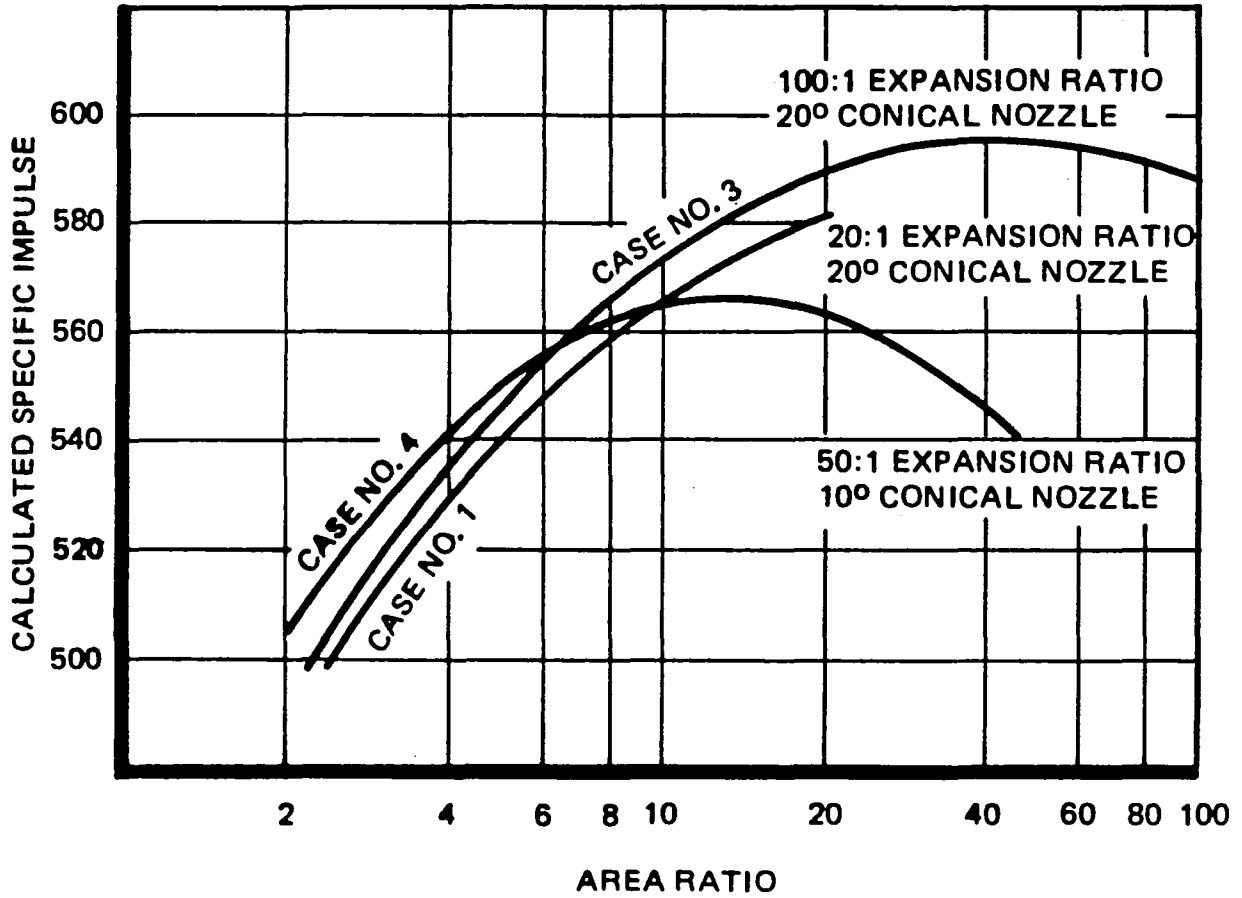


$I = 30$ amps
 $\dot{m} = 2.27 \times 10^{-5}$ kg/s
 $D_{CONSTRICTOR} = 7.62 \times 10^{-4}$ m
 $L_{CONSTRICTOR} = 8.73 \times 10^{-4}$ m
 $L/D = 1.13$

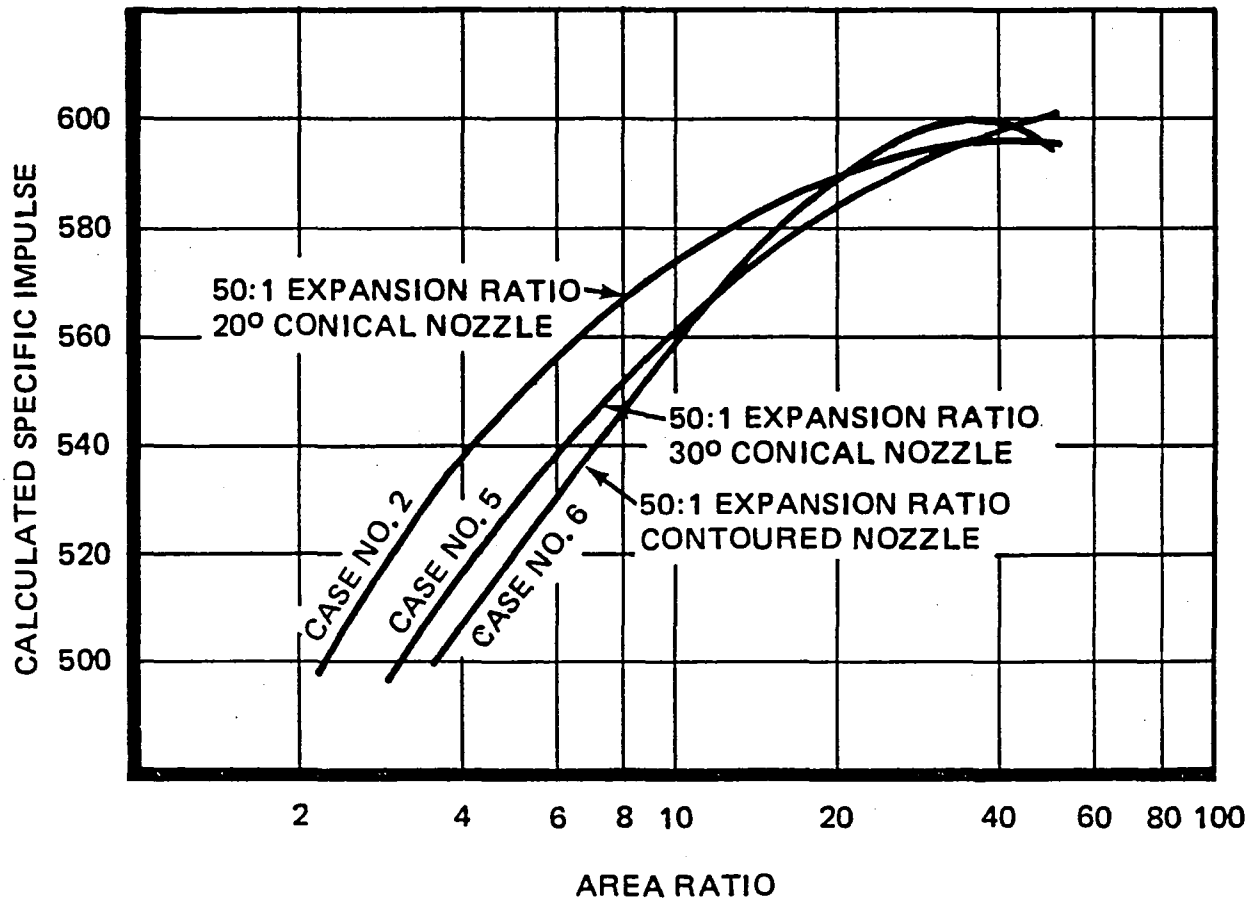
VNAP2 OUTPUT
 PRESSURE, DENSITY, AND TEMPERATURE PROFILE, CASE 1



VNAP2 ANALYSIS RESULTS
 I_{sp} VARIATION WITH AREA RATIO; CASES 1, 3 AND 4



VNAP2 ANALYSIS RESULTS
 I_{sp} VARIATION WITH AREA RATIO; CASES 2, 5 AND 6



The contoured nozzle has a Rao profile. The calculated specific impulse was 5 seconds less than the 30° conical nozzle for the same expansion ratio. Viscous losses start to be significant near the end of the contoured nozzle.

The preliminary conclusion reached based on this work is that nozzle optimization is somewhat limited by the low Reynold's numbers and associated viscous losses. Nozzle contours will not strongly affect performance. However, testing should be conducted to verify the model predictions about expansion ratios and nozzle half-angles. Future analysis work in this area could lead to a better understanding of the anode attachment region.

3.1.3 Gas Kinetics

Gas kinetics were found to play an important role in arcjet performance relative to traditional N_2H_4 thrusters. These effects govern the manner by which the electrical energy is converted into thermal energy in the propellant. Frozen flow losses, which result from energy loss to ionization and dissociation, make up the largest power loss term in the overall efficiency relation. Gas kinetic effects also determine the dynamic characteristics of the arc. This is important to PCU designs. And finally, chemical erosion of the electrodes may depend on the kinetic behavior of the propellant.

The computer model CREK1D was used to study these effects. It is a singlepoint, batch process, adiabatic, constant pressure, homogeneous, gas phase chemical kinetics model. It was selected because of its possible application as a subroutine in RRC's arc energy balance model in order to calculate nonequilibrium plasma conditions. Initial molal concentrations, temperature, and reaction rate constants are input to the program. The program then calculates the state of the mixture as a function of time.

An initial catalogue of dissociation reactions and rate constants were assembled from a review of rate data for N-H systems³. These are given in Table 3-3. The O-H-N reactions are included to simulate the small amount of H_2O present in hydrazine.

Table 3-3
REACTION RATE DATA

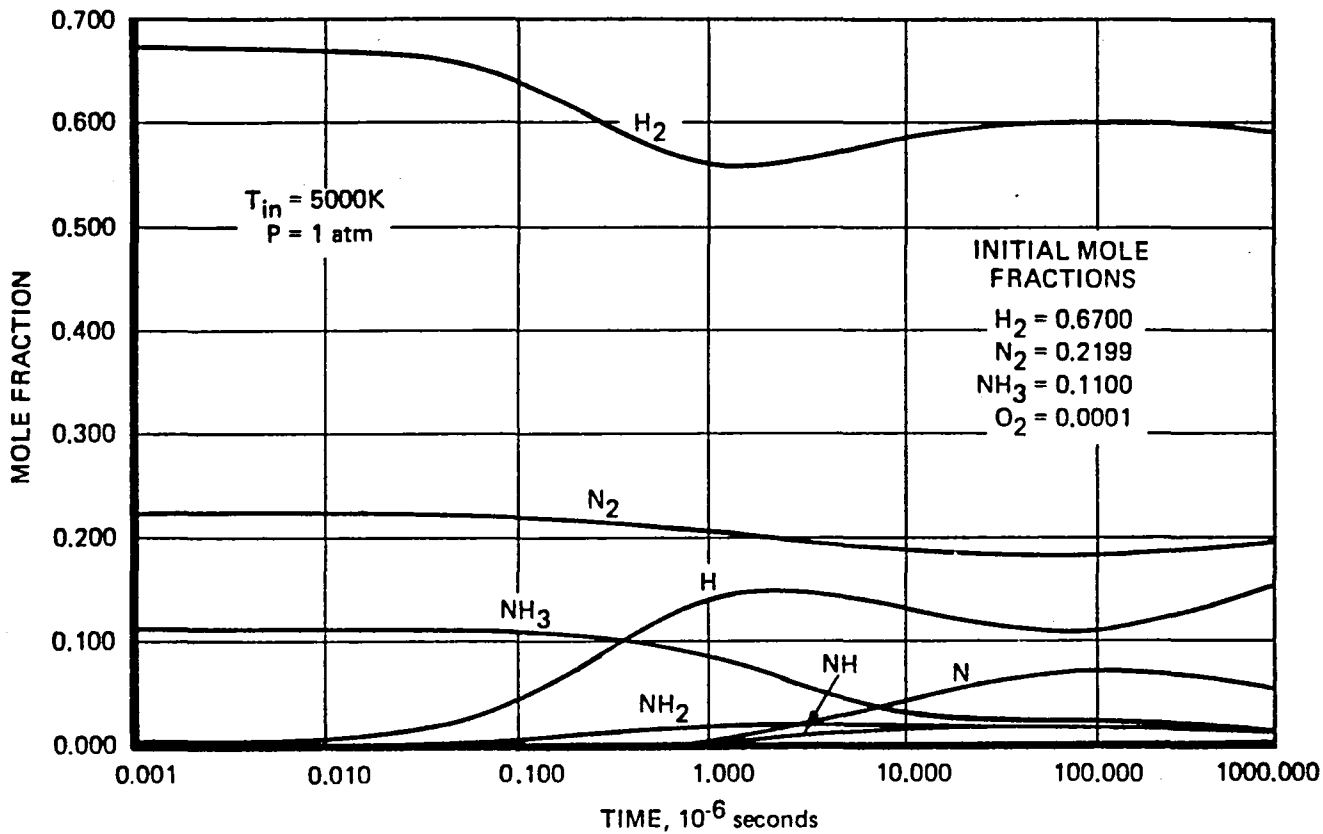
$$k = A T^N e^{-(E/RT)}$$

Reaction	A	N	E kcal/mol
$\text{NH}_3 + \text{M} = \text{NH}_2 + \text{H} + \text{M}^*$	E 14.52	0	84.2
$\text{NH}_2 + \text{NH}_2 = \text{NH}_3 + \text{NH}^*$	E 12.60	0	5.56
$\text{H} + \text{NH}_3 = \text{NH}_2 + \text{H}_2^*$	E 12.0	0	6.23
$\text{H} + \text{NH}_2 = \text{NH} + \text{H}_2$	E 10.92	0	5.60
$\text{H} + \text{O}_2 = \text{O} + \text{OH}$	E 14.34	0	16.492
$\text{H}_2 + \text{O} = \text{H} + \text{OH}$	E 13.48	0	19.339
$\text{H}_2\text{O} + \text{O} = \text{OH} + \text{OH}$	E 13.92	0	18.121
$\text{H} + \text{H}_2\text{O} = \text{H}_2 + \text{OH}$	E 14.0	0	19.870
$\text{N} + \text{O}_2 = \text{NO} + \text{O}$	E 9.81	1.0	6.25
$\text{N}_2 + \text{O} = \text{N} + \text{NO}$	E 13.85	0	75.506
$\text{NO} + \text{M} = \text{N} + \text{O} + \text{M}$	E 20.6	-1.5	149.025
$\text{H} + \text{H} + \text{M} = \text{H}_2 + \text{M}$	E 18.0	-1.0	0.0
$\text{O} + \text{O} + \text{M} = \text{O}_2 + \text{M}$	E 18.14	-1.0	0.340
$\text{H} + \text{OH} + \text{M} = \text{H}_2\text{O} + \text{M}$	E 23.88	-2.6	0.0
$\text{H}_2 + \text{O}_2 = \text{OH} + \text{OH}$	E 13.0	0	4.3

A typical output is shown in Figure 3-6. The initial mole fractions are: NH_3 , 0.11; H_2 , 0.67; N_2 , 0.2199, O_2 , .0001. This is typical of the decomposition products exiting the catalytic gas generator used for the arcjet. The initial temperature is set at 5,000 K. In the first 10 microseconds, the NH_3 mole fraction drops from 0.11 to 0.04, the H_2 fraction decreases from 0.67 to 0.58, the NH_2 level rises to 0.02, the H fraction rises to 0.12, and the N_2 fraction drops to 0.20.

Gas residence times within the arc region are calculated to be on the order of 1 to 10 microseconds, depending on the radial position inside the constrictor. The energy transfer times from the electrons in the arc to the incoming molecules are several orders of magnitude faster. Yet the chemical reaction times are of the same order or slower. This results in a plasma that is in temperature equilibrium, but not in chemical equilibrium.

CREK 1D N₂H₄ DATA



- COMPARISON RUN MADE BY NASA LeRC WITH GCKP84. AGREEMENT WITHIN 1.5%
- CONCLUSION
 - REACTION KINETICS PLAY DOMINANT ROLE IN DETERMINING SPECIES, ENERGY DEPOSITION IN ARCJETS

In time, the thermal energy is used to overcome the bond energies, until chemical equilibrium is reached. However, as the results of the CREKID analysis indicate, the gas does not reside in the constrictor long enough for equilibrium to occur before expansion processes occur in the nozzle. The result is that some thermal energy may be converted to directed kinetic energy without suffering the inherent losses of chemical equilibrium. This may reduce frozen flow losses by lowering the percentage of the propellant that dissociates.

Rate reaction times may also play a role in determining the chemical compatibility of the electrode materials. As will be discussed in paragraph 3.3, Operational Testing, oxidation was not observed on the constrictor walls, although the temperatures are high enough to cause this reaction with tungsten. Reaction rates and short contact times may be responsible.

The dynamic behavior of the arc is determined by the arc's reaction to current transients. Carbon arcs in air are reported to have a positive voltage/current characteristic at an input frequency of 1 kHz⁴. This arises because the input current oscillation period is comparable to the ionization times of the plasma species. The arc cannot respond to the current change, so a phase shift results between the voltage and the current. Ionization reactions were not investigated under this program. However, a comparison of their rates to the input current ripple frequency may be helpful to PCU stability analyses and design.

3.1.4 Vortex Analysis

Experimental data has indicated the need for a swirling gas flow to stabilize the arc column in an arcjet. Arc stability requirements and the influence of swirl flow intensity on arcjet performance, however, have not been well characterized. At the onset of this study, there were three areas of interest:

1. Develop vortex generation parameters to guide design of injector and vortex chamber.
2. Establish the influence of swirl intensity and constrictor geometry on vortex stability and dissipation.
3. Assess arc-vortex interaction factors.

The intent was to develop predictive tools for basic hardware design, test planning and data analysis.

Based on a brief literature review, some general observations on vortex action were made.

1. Mass flow through a choked constrictor/nozzle can be sharply reduced by vorticity in the flow.
2. Local flow reversal can be produced in a circular duct or nozzle by introducing a sufficiently high degree of swirl into the flow. Depending on the geometries involved, this phenomena has been attributed to either vortex breakdown transition or the formation of complex two-cell vortex flow patterns. Theories and data on vortex instability expressed in the literature are often contradictory and do not seem to present a coherent method for prediction.
3. Viscous effects will reduce arc stabilizing pressure gradients for constrictors with large l/d if secondary injection is not provided.

Each of these effects of vortex flow may influence the design and operation of an arcjet. The analytical and experimental pursuit of these complex phenomena was not within the scope of this program. Appendix C summarizes several of the analytic techniques described in the literature.

Conclusions

1. Accurate characterization of the interaction between an arc column and an applied vortex flow field is not amenable to simple analytic techniques and will require a detailed numerical solution.
2. Due to the complexity of the flow geometry in the injector and constrictor inlet zones a numerical flow analysis of even a cold flow field may be difficult. Based on VNAP2 analyses done at RRC, the numerical solution of converging two-dimensional, compressible flow fields is difficult even with simple boundary geometries. The addition of swirl flow and a central blunt body (cathode) will significantly complicate the analysis. Basic flow patterns would best be determined experimentally.
3. Several approximate techniques for determining limiting constrictor inlet velocity profiles which will avoid potential vortex breakdown have been identified from the literature. These techniques should be developed further and experimentally verified.
4. As a supplement to any further analytic work, experimental determination of flow fields within the arcjet injector, constrictor and nozzle zones is warranted. Experimental validation of any flow analyses is required before they can be confidently applied for design and data correlation purposes.

3.1.5 Thermal Modeling

A detailed thermal model of the research thruster was developed using the Thermal Model Generator (TMG) code. TMG is a finite difference thermal analysis program that is format compatible with most structural codes and is able to generate conductive, convective, and radiative networks based on a mesh description. This code is routinely used at RRC for flight production resistojets and monopropellant thrusters, and compares well with test thermocouple data.

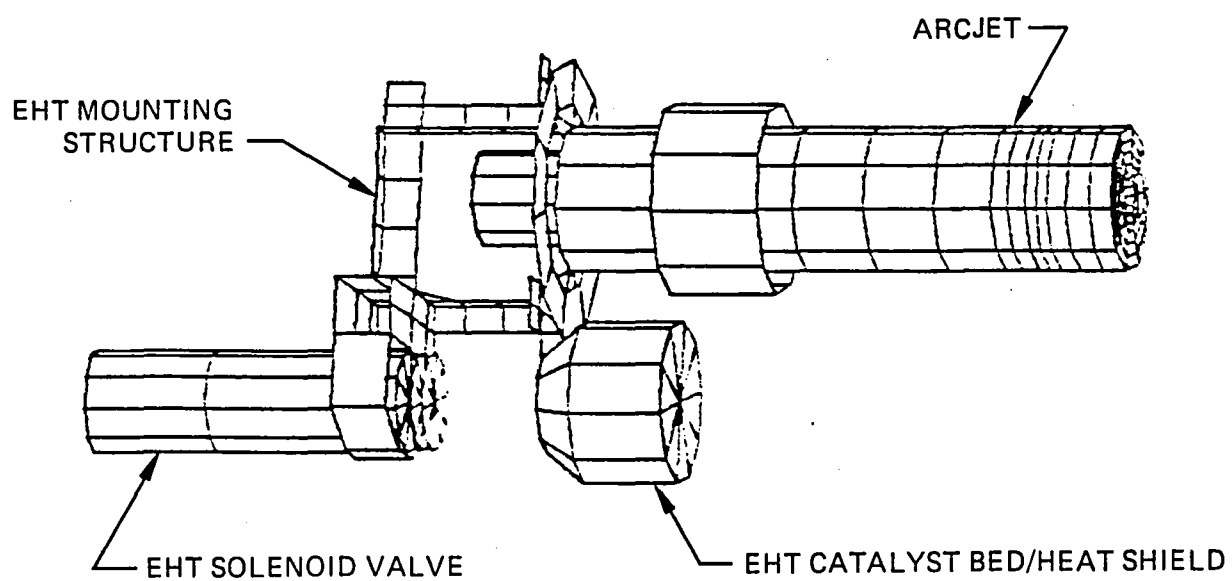
Figure 3-7 shows the NISA mesh generated of the arcjet, N_2H_4 decomposition bed, solenoid valve and mounting structure for analysis. This design will be discussed in greater detail under paragraph 3.2, Design/Fabrication/Assembly. The arcjet TMG model was applied by specifying the mass flow, external radiation environments, a point power input at the anode to simulate the anode fall, and a fixed cathode tip temperature to simulate the molten zone. Since the anode input power is dependent on specific operating conditions, a range of simulated power levels was investigated. Anode fall voltages are typically estimated at between 15 and 25 volts⁴. At a 30A current level, this would conservatively result in an anode heat load of 750 W. A worst-case of 1,000 W was chosen for this study.

The model served several purposes. It was used initially to characterize the transient and steady-state thermal environment of the design. Certain key areas are temperature critical, such as the solenoid valve, seals, and the catalyst bed injection capillary tube. Worst-case conditions of maximum power input at a minimum flow rate, then shutting off both the flow and the anode power input, were simulated. Thermal soakback was checked to make sure it did not exceed the safe limit for the valve ($150^{\circ}C$). It was shown that even under worst conditions, soakback on shutdown would not overheat critical areas.

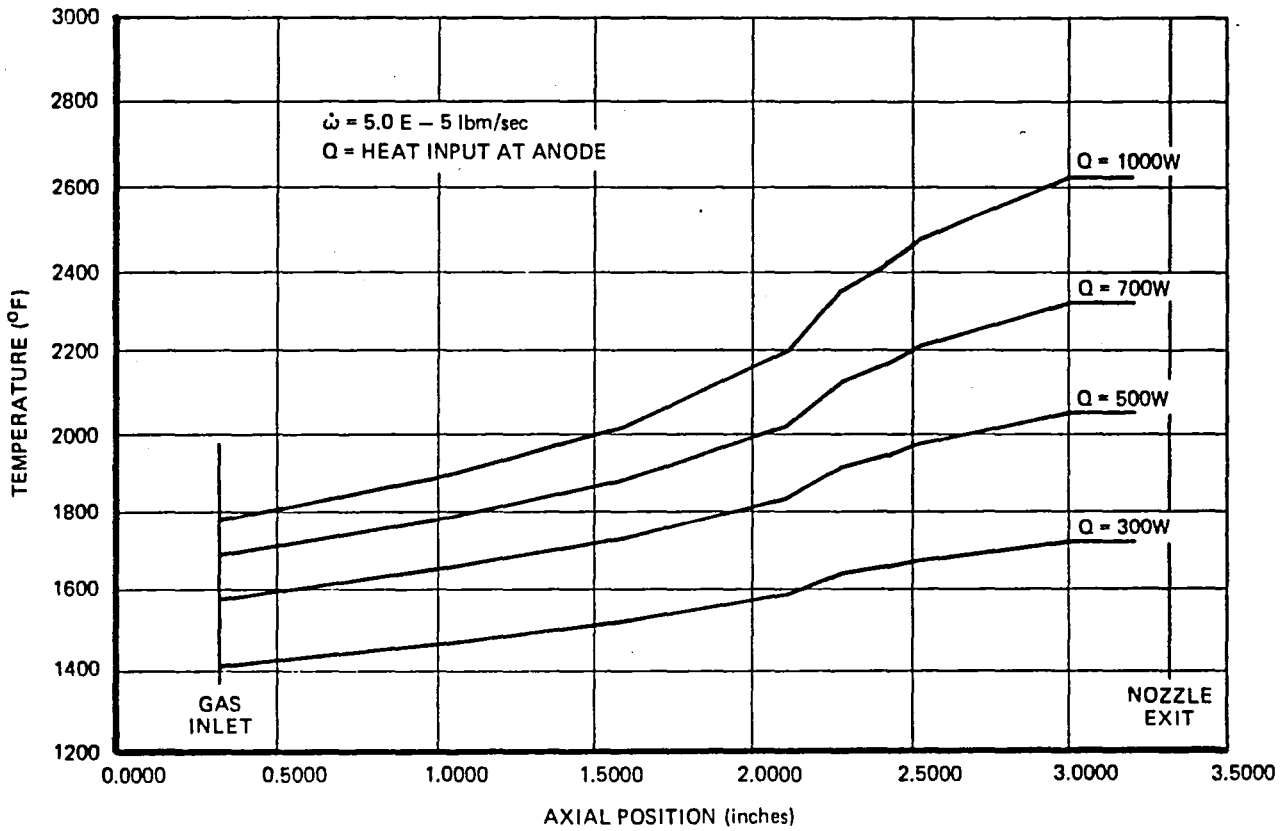
The model also provided temperature data on seal areas. At the aft end of the arcjet, thermal cycles to $593^{\circ}C$ would be produced. At the gas inlet, temperatures to $760^{\circ}C$ were predicted.

Figure 3-8 shows surface temperature profiles of the arcjet itself for several anode input power levels at a worst case low flow rate of 2.27×10^{-5} kg/s. Even at 1,000 W input, which would correspond to a low thermal efficiency of 66% at 3,000 W total power, the maximum temperature predicted is $1,440^{\circ}C$. This is at the recrystallization temperature of TZM ($0.5 T_j$, 0.1 Zr, Mo), but is far below its melting temperature.

NISA GENERATED N_2H_4 ARCJET TMG MODEL



TMG ARCJET SURFACE TEMPERATURE PROFILES



A second study was performed to evaluate the regenerative heating capacity of the design. The propellant passes through an annular passage near the outer surface. A hydrazine flow rate of 4.5×10^{-5} kg/s at an ammonia dissociation fraction of 80% was assumed. The local Reynold's numbers ranged from 49 to 224 in the passage, indicating laminar flow conditions exist throughout. The resulting heat transfer coefficients and surface areas caused the temperature of the slowly moving gas to approach that of the arcjet structure. The gas was heated to within 14°C of the maximum temperature of the gas passage.

These results indicate that little performance advantage could be gained by optimizing the regenerative heating of the low power arcjet operating at the temperatures predicted. Some performance gains would result from raising the structure temperatures through shielding or by reducing the radiative area. However, this would impose a harsher environment on the materials.

A third use of the thermal model was to determine thermal efficiencies based on thermocouple data taken during testing. Anode power losses were calculated based on a comparison of experimental and calculated temperature profiles. These results are discussed in paragraph 3.4, Performance Testing.

3.2 DESIGN/FABRICATION/ASSEMBLY

3.2.1 Design Guidelines

Several design requirements were identified for the laboratory N_2H_4 arcjet. The first design requirement was that because of the large number of parameteric studies planned, the design should be highly modular. This allows variation of key components without perturbing the supporting hardware.

A second design requirement was that repeatable operation required very close tolerances on the parts and on the assembly. The relationship between the cathode, anode, and injector was of primary importance.

A third design requirement was that assembly and setup times were to be kept to a minimum. This was again driven by the large number of parametric tests planned.

A final requirement was to rely on existing flight proven N_2H_4 gas generator technology. To this end, the mounting structure, catalyst bed, and solenoid valve were all taken from the Electrothermal Hydrazine Thruster (EHT), which is a resistojet.

The resulting design met each of these requirements.

3.2.2 Design Description

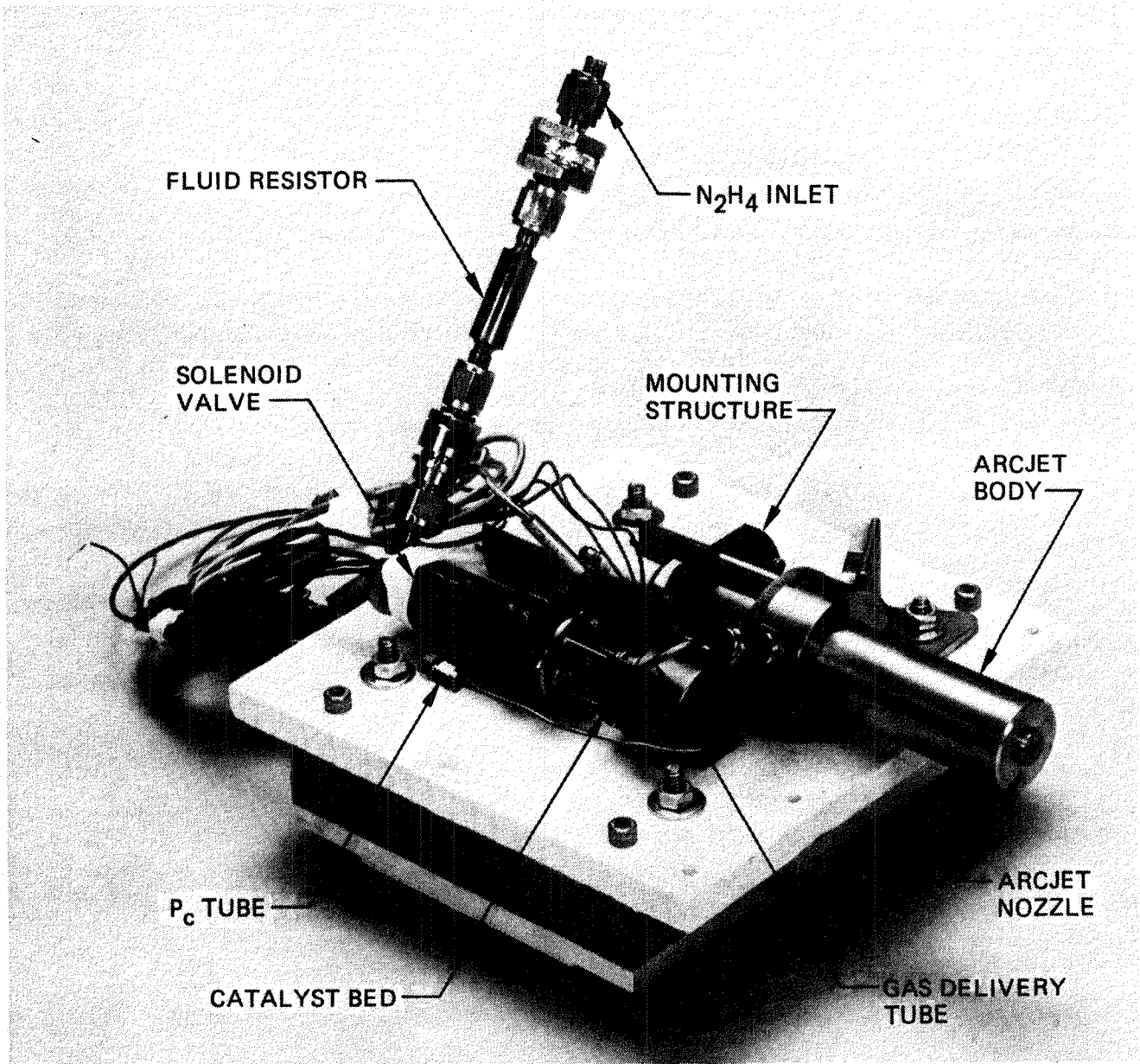
Figure 3-9 shows the assembled N_2H_4 arcjet developed under this program. Liquid N_2H_4 passes through the fluid resistor into the solenoid valve. This is a dual seat, flight qualified valve operating on 28 VDC. The propellant is then injected into the catalyst bed through a capillary tube. The N_2H_4 decomposes to an $800^\circ C$ ($1,500^\circ F$) gaseous mixture composed of NH_3 , H_2 , N_2 , and O_2 . The gases are vented through the gas delivery tube into the arcjet.

Figure 3-10 shows a cross section of the arcjet. The hot gases enter about 7.5 cm from the nozzle exit, then pass through an annulus between a boron nitride insert and the outer TZM body. The cross-sectional area of this passage is nominally 0.3 cm^2 .

It is then injected into the arc chamber area through a tungsten insert. There are hemispherical grooves cut tangentially into the injector. The injector faces up against the anode to form the passages.

Table 3-4 lists the possible materials identified for each component. The standard materials used were 2% thoriated tungsten for cathodes, pure tungsten for anodes, high purity boron nitride for insulators, and TZM for the outer body and cathode holder. Several molybdenum and rhenium alloys were identified for both the cathode and the anode because of their increased resistance to oxidation. It was not known at that time if the approximately 1% H_2O content of MIL-P-26536C, Amendment 2, High Purity grade N_2H_4 would pose a compatibility problem.

LOW POWER HYDRAZINE ARCJET



N_2H_4 ARCJET DESIGN

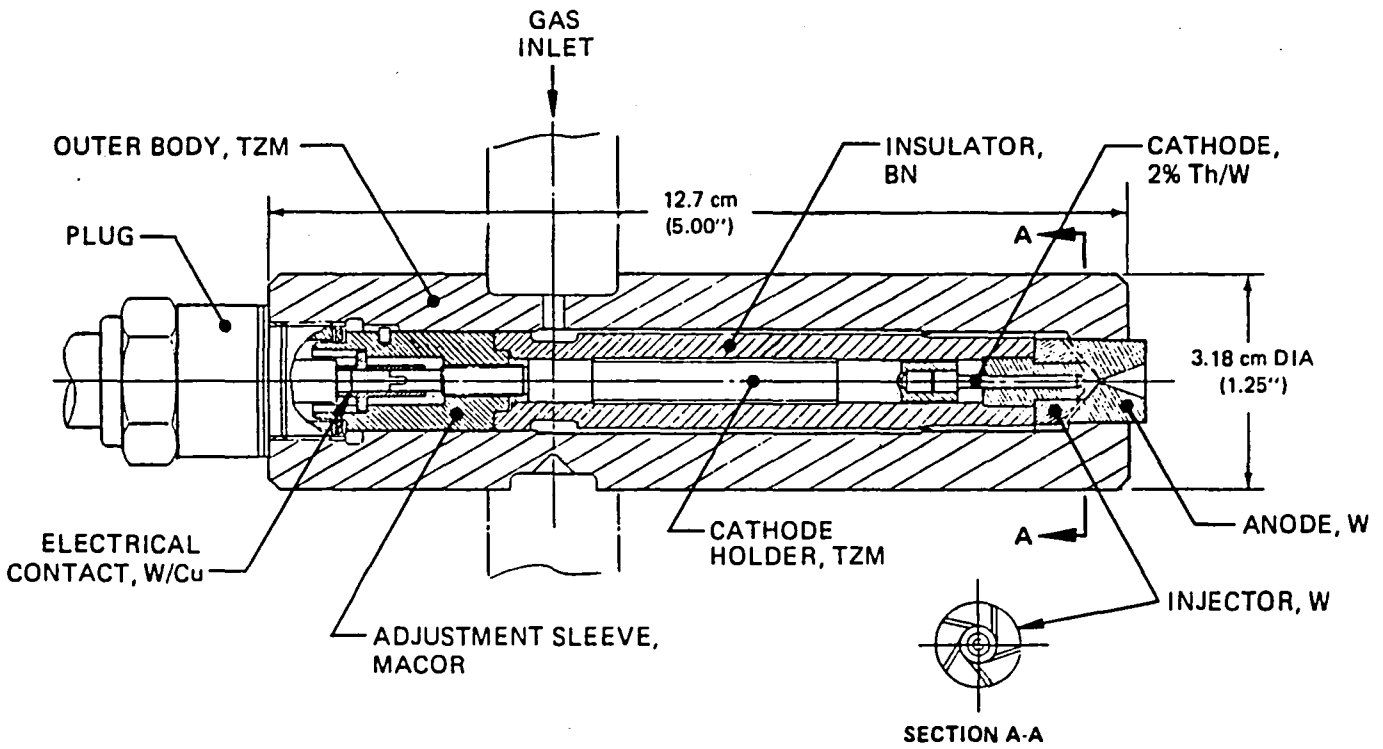


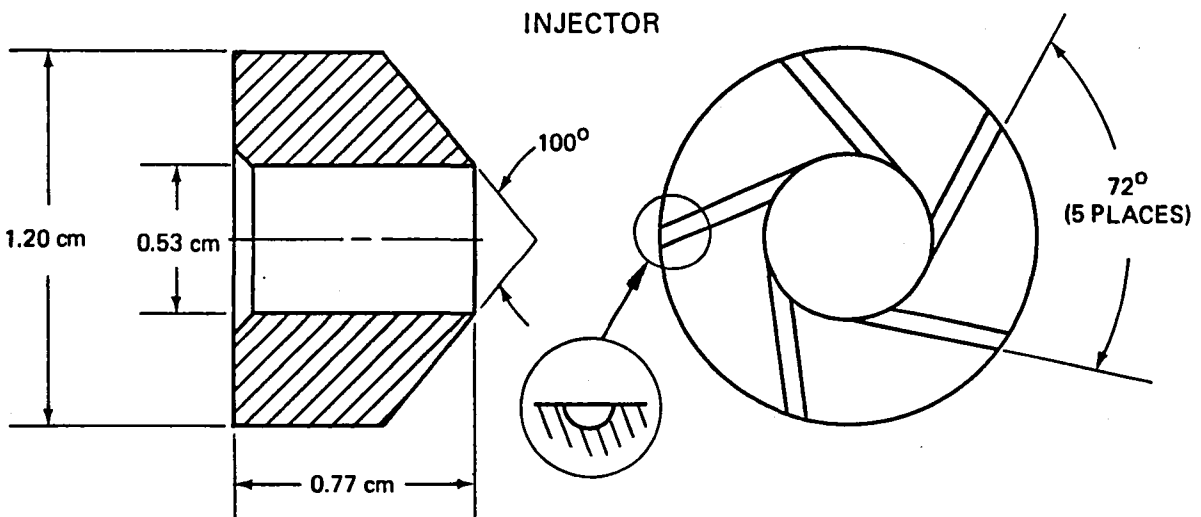
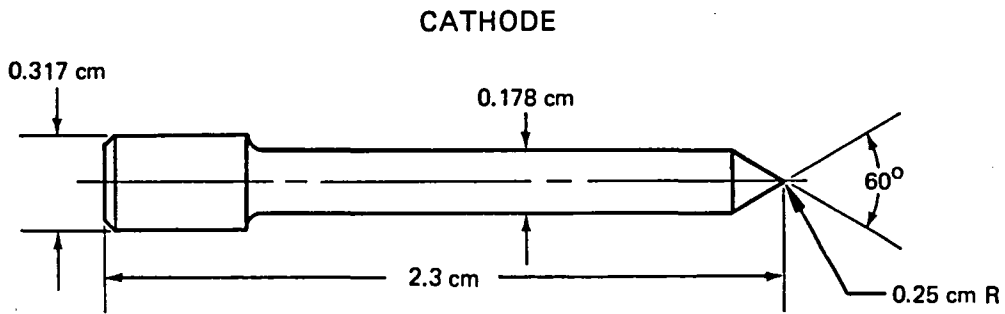
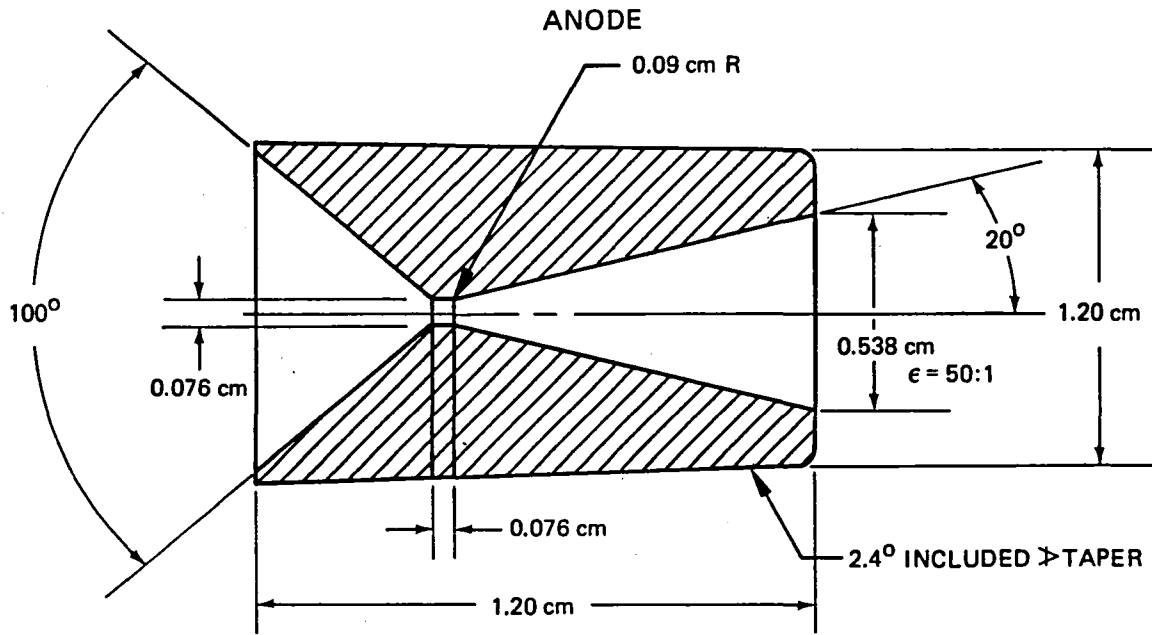
Table 3-4
MATERIALS LIST

Cathode:	2% Th/W 2% Th/W/5% Re 2% Th/W/26% Re 2% Th/Re
Anode:	Pure W W/26% Re Pure Re Moly/41% Re
Insulators:	High purity boron nitride
Outer body, Cathode holder:	TZM

Referring again to Figure 3-10, the anode is mated to the TZM main body by a positive taper press-fit. This anode/main body design allows for the same main body to be used with several different anodes. The cathode employs a two piece design for similar reasons. A boron nitride sheath with a modular gas injector is used to insulate the cathode and to generate a vortex flow field in the arc. Macor is used in the aft quarter to sheath the cathode and to interface with the end plug. The Macor is threaded, along with the cathode holder, in order to adjust the arc gap setting. A tungsten-copper terminal provides the electrical connection from the plug to the cathode. The plug is a modified spark plug that serves as the electrical feed through and provides the mating surface for the end seal of the arcjet. A later design modification replaced this plug with a boron nitride powder compression seal. A carbon paper gasket is compressed between the plug and the main body to form a seal. The propellant line/main body seal is also accomplished using this material. A tensioning ring with a threaded fitting is used to form a face seal on the side of the arcjet body.

Typical geometries for the anode, cathode, and injector are found in Figure 3-11. These components were inspected prior to assembly. All parts were thoroughly cleaned and assembled by personnel trained in clean room practices. A fabrication and

TYPICAL GEOMETRIES



assembly document controlled the assembly of each thruster. This lists the part serial numbers, verifies that all steps have been completed, documents leak tests results, is used to record the runout on the cathode holder/cathode assembly (0.005 cm acceptance criterion), and provides a record of the gap setting procedure. A similar document controls the disassembly and inspection process.

3.3 OPERATIONAL/LIFETIME TESTING

Three periods of arcjet testing were conducted: operational/lifetime, performance, and PCU evaluation. The objectives met during the first period were to develop non-erosive, repeatable starting techniques, to demonstrate stable arcjet operation, and to evaluate materials compability with N_2H_4 . Thrust measurements were not made during these tests.

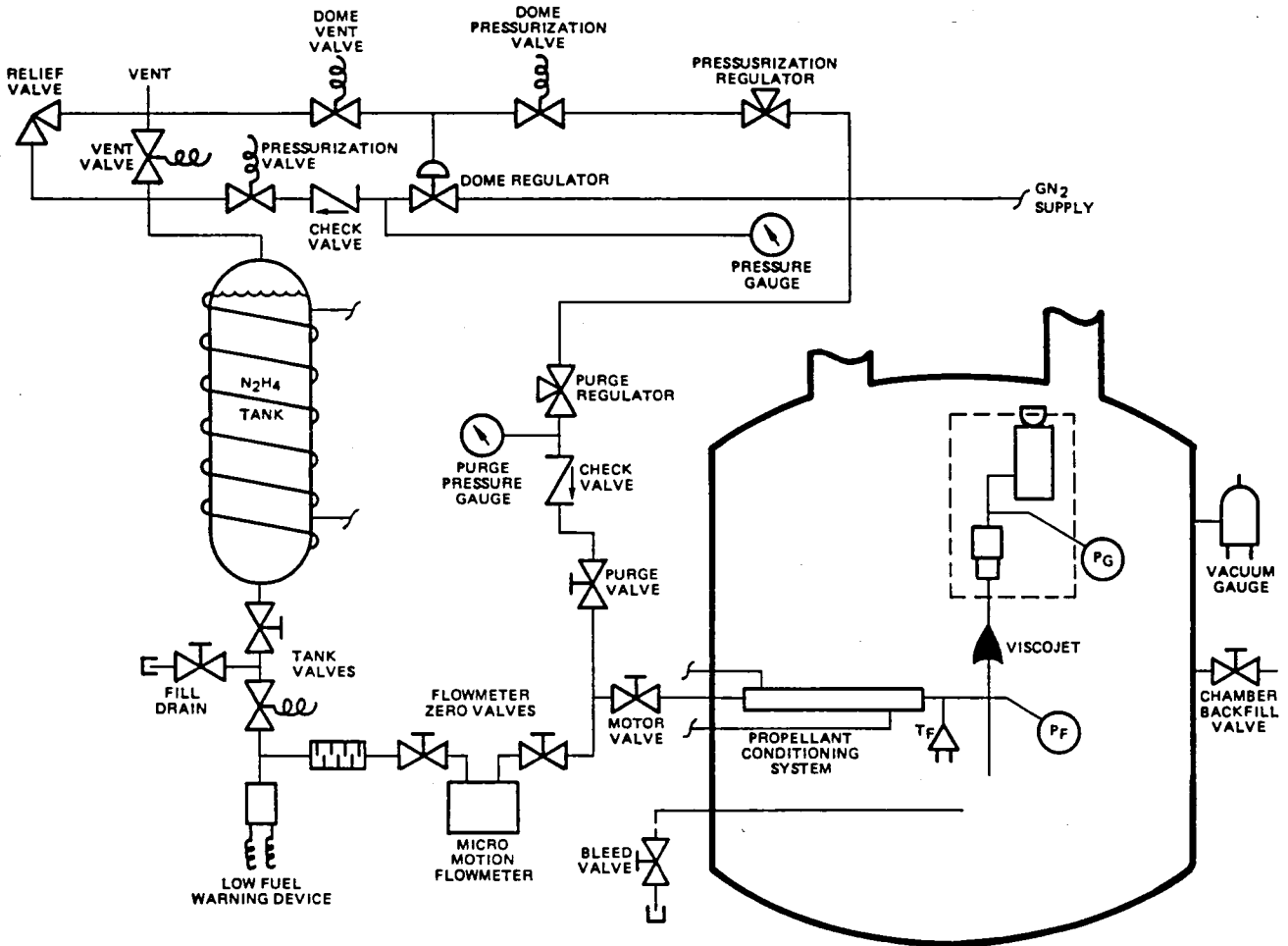
3.3.1 Facility

Operational/lifetime testing was performed in cell 6 at the RRC test facility. The thruster was mounted on a fixed post in the center of the vacuum chamber. Quartz windows allowed visual observation. The vacuum was maintained by 3 Stokes pumps with a capacity of 10580 cfm, which produced a 60 mTorr vacuum pressure at a nominal flow rate of $4.5E-5$ kg/sec.

The propellant delivery system is shown in Figure 3-12. The pressurized liquid N_2H_4 passes through two latch valves and a filter prior to entering the flow meter. The flow meter has valves on either side, which are closed when a flow zero is recorded. Downstream of the flow meter is a remotely controlled motorized needle valve which is used to set the flow rate. Most of the propellant line inside the chamber is conditioned with water jackets. The unjacketed tubing is wrapped to protect it from exposure to thermal radiation from the thruster or the plume. These precautions were taken to prevent thermal flow transients that could cause unsteady thruster operation or flow measurement errors.

Downstream of the cooling jackets are the fluid resistor, solenoid valve, catalyst bed, and arcjet. The thruster is described in section 3.2, Design/Fabrication/Assembly. The fluid resistor is used to ensure adequate fuel system back pressures (> 50 psia) at low mass flow rates.

PROPELLANT SYSTEM SCHEMATIC



The flow meter used was first calibrated with water. The meter measures the mass flow by monitoring the Coreolis deflection of an oscillating U-tube through which the propellant flows. It is made by Micro Motion. The results of the calibration are shown in Figure 3-13. The output is accurate to within +/- 2% at $4.5E-5$ kg/sec.

All testing used MIL-P-26536C, Amendment 2, Hi-Purity grade N_2H_4 . Periodic chemical analyses were conducted to ensure that the propellant met this specification at all times. Figure 3-14 shows the results of a completed analysis.

The parameters measured are shown in Table 3-5. Data were recorded on stripchart recorders and on a digital data system which cycles through 32 channels once every millisecond. By assigning more than one channel to a parameter, sample periods less than a millisecond were obtained. An oscilloscope was also used to monitor the transients. Temperatures were measured using type K chromel-alumel thermocouples.

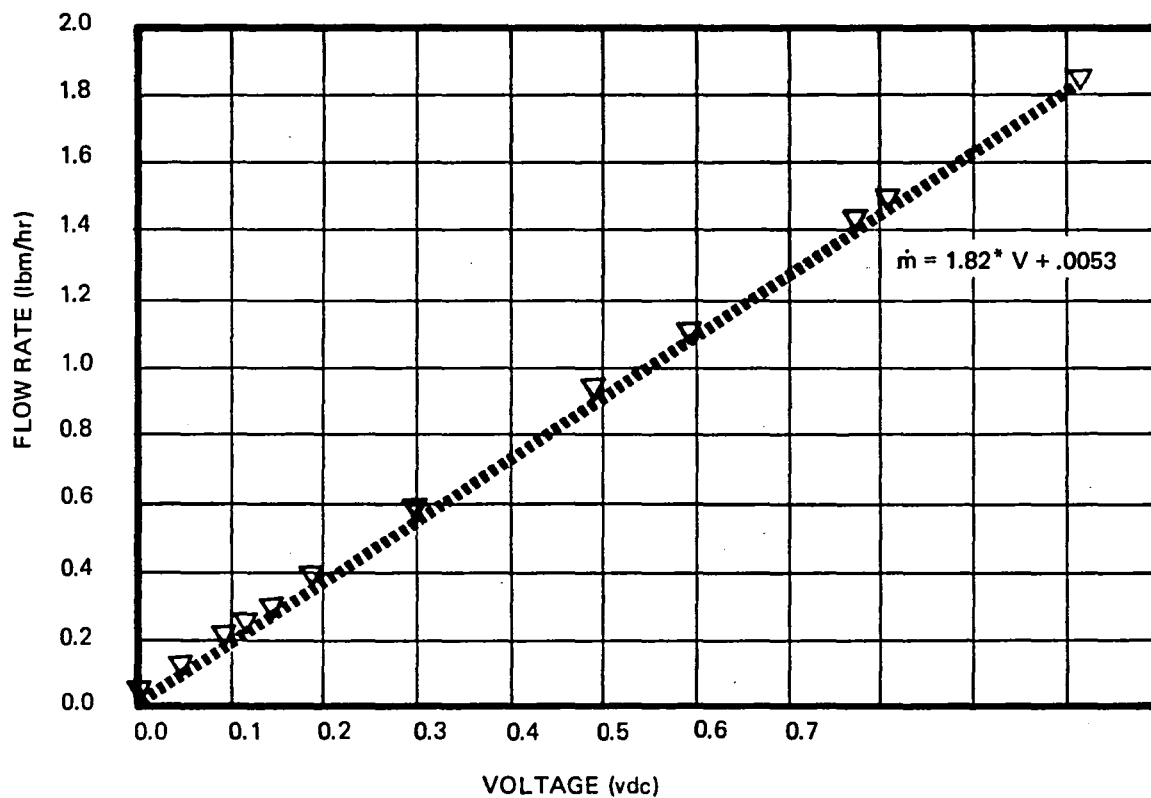
A high voltage starting capacitor network was connected in parallel with a Sorensen DCA 150-70 commercial power supply to operate the arcjet. A ballast resistor was used in series with the arcjet to provide the impedance matching needed to maintain arc stability.

3.3.2 Startup Testing

There are several means of establishing an arc. An overvoltage method was selected for the arcjet because of its relative simplicity. A high DC potential of from 600 to 2500 V is applied across the electrodes. The electric field causes electrons to leave the cathode through field processes. The field imparts energy to the electrons, which then collide with the propellant neutrals to form ions. Some of these ions are then accelerated back into the cathode, causing a local temperature rise. At a high enough temperature thermionic emission occurs, which greatly increases the electron flux. A cascade effect ionizes a path to the anode surface. If the source of electrons is sufficient, with the flow field, electrode geometry, and PCU permitting, a stable arc is formed.

Startup erosion occurs when localized heating of the electrodes causes evaporation or melting to occur. This was found to be a strong function of the initial current transient and the gas flow field. The arc first attaches at or near the upstream edge of the

MICROMOTION FLOWMETER CALIBRATION



N₂H₄ ANALYSIS REPORT

ROCKET RESEARCH COMPANY
HYDRAZINE ANALYTICAL FORM
FOR HYDRAZINE MEETING MIL - P - 26536, AMENDMENT 2

Date Sampled: 4-4-86 Originator: P. MEHL Approval: Ray Mehl

Date Due: _____ Sample ID: DRUM H 8050

Date Received: _____ Charge No.: 121581-2210 Control No.: 64162

Disposition of Sample: DESTROY

ANALYSES REQUESTED	CHK.	ACCEPTABLE VALUES MONOPELLANT GRADE		RESULTS	<input checked="" type="checkbox"/> ← Check Upper Box For All	ACCEPTABLE VALUES HIGH PURITY GRADE		RESULTS
		% BY WEIGHT	ppm			% BY WEIGHT	ppm	
N ₂ H ₄		99.50 min.	N/A	%		99.00 min.	N/A	99.04 %
H ₂ O		1.00 max.	N/A	%		1.00 max.	N/A	.81 %
NH ₃		0.40 max.	N/A	%		0.40 max.	N/A	.15 %
Trace Organics Excluding Aniline		0.020 max.	200	ppm		0.005 max.	50	1.2 # ppm
Aniline		0.50 max.	N/A	%		0.005 max.	50	18 ppm
Total Non-volatiles (NVR)		0.0020 max.	20	ppm		0.0010 max.	10	5 ppm
Particulate		1 mg/L max.	N/A	mg/L		1 mg/L max.	N/A	0 mg/L
Corrosivity		0.00125 % Fe max.	12.5	ppm		0.00125 % Fe max.	12.5	1.5 ppm
Chloride		0.0005 max.	5	ppm		0.0005 max.	5	0.5 ppm
Iron		0.0002 max.	2	ppm		0.0002 max.	2	< 1.5 ppm
CO ₂		0.0030 max.	30	ppm		0.0030 max.	30	7.5 ppm
Silicon (OPTIONAL)		0.000005 max.	0.05	ppm		0.000005 max.	0.05	< 0.05 ppm

Analysis Completed And Reviewed

Signature: A. Fields Date: 4-8-86

Table 3-5
NASA LeRC LOW POWER ARCJET
INSTRUMENTATION LIST

Parameter	Symbol	Range	Recorder	
			SCR	DDS
A. Temperatures				
Propellant line				
1) at entrance to test cell	TPI	0-65°C		X
2) downstream of last cooling jacket	TF	0-65°C		X
3) just upstream of valve	TP3	0-65°C	X	X
4) valve	TP4	0-65°C	X	X
5) just upstream of GG	TP5	0-65°C	X	X
6) just downstream of GG	TP6	0-1230°C		X
Engine (12)				
o Type K TC's	TE1-TE12	0-1230°C	X	X
B. Flow Rate, Micromotion flowmeter	m	0-1.0E-4kg/sec	X	X
C. Pressure -				
1) downstream of GG	Pc	0-100 psia	X	X
2) upstream of viscojet	Pf	0-500 psia	X	
D. Arc Voltage	V	0-900V	X	4X
E. Arc Current	I	0-100A	X	4X

constrictor on the anode. Because of the higher pressures and high field concentrations, the arc attachment is most likely columnar at this point. During a proper start, the arc is then quickly swept downstream by the gas flow through the constrictor into the nozzle, where a noncolumnar attachment occurs. If the arc resides upstream too long, or if the transient current level is too high, the heating caused by the anode fall potential becomes excessive, and melting of the surface can occur. Qualitatively, minimizing the transition time from initial breakdown to stable nozzle attachment, and controlling the initial current surge are needed to produce non-erosive starts.

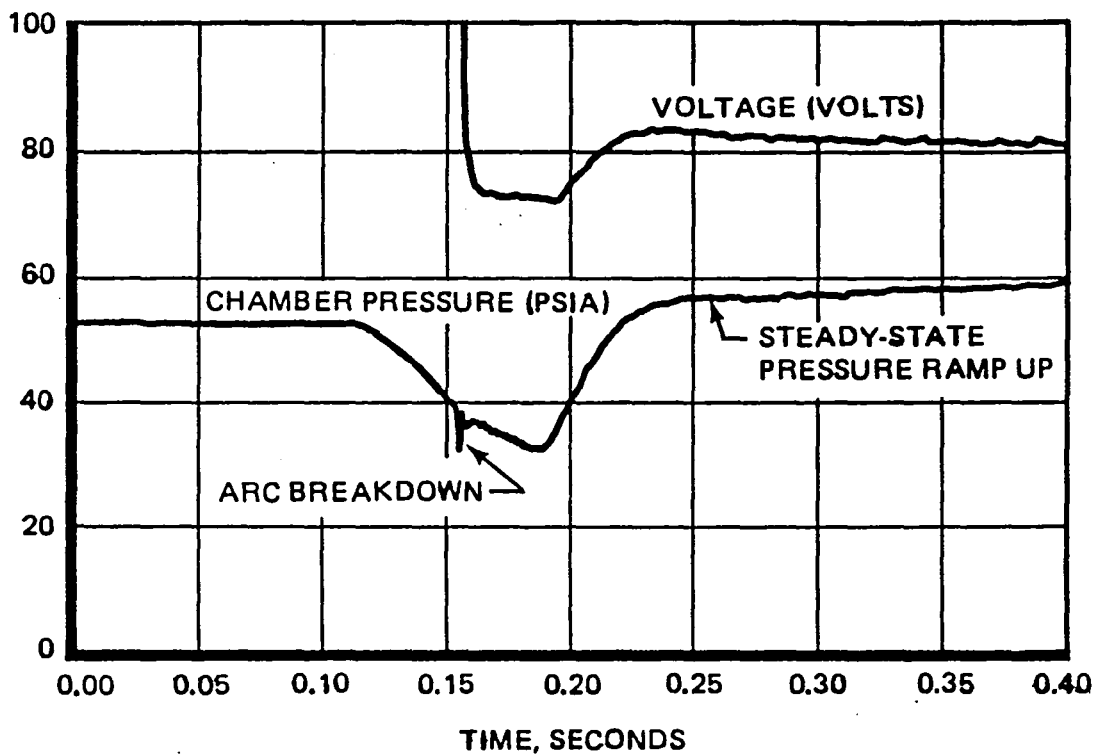
The initial tests of the N_2H_4 arcjet were used to explore startup techniques and the general operating behavior of the thruster. Two startup techniques were developed. For the first method, the steady state flow rate was set, then the capacitive starting circuit charged to 600 to 800V. This was not a sufficient potential to initiate the arc at the steady state pressures, yet the circuitry was limited to these voltages. The arc was started by lowering the flow rate with a remote control needle valve until breakdown occurred, at which point the steady state flow rate would be restored. The draw back of this method is that the arc would tend to reside on the upstream surfaces of the constrictor for too long a time (several seconds), resulting in anode erosion.

A second method was developed to reduce this time. This entailed sending a short (100 millisecond) low pressure pulse through the thruster while at steady state flow conditions by briefly shutting off the liquid N_2H_4 solenoid valve located upstream of the catalyst bed. This method significantly reduced the anode erosion by decreasing the time the arc spent attached on the upstream surfaces while under the influence of a lower pressure flow field.

A typical breakdown sequence is seen in Figure 3-15. The catalyst bed chamber pressure drops in approximately 50 msec to below 40 psia. The breakdown is evident by the pressure disturbance and the voltage drop. Then the solenoid valve opens and the pressure ramps up, driving the voltage up. A large number of starts were conducted with this method. They were generally quite repeatable.

The startup tests led to several conclusions. The first is that the flow field is important to the startup process. Ideally, starts should be conducted at full flow to reduce the transition time from breakdown to stable nozzle attachment. This will require, however,

PRESSURE PULSE STARTUP



breakdown voltages of from 1500 to 2500V. A second conclusion is that the power supply plays a crucial role in affecting a nonerosive start through control of the initial current transient. The capacitive circuit used for these tests permitted too large of a current surge, which results in overly high heat fluxes at the first arc attachment point. Control of this surge is a requirement for any PCU design. A third conclusion is that many non-erosive starts are possible for a catalytically decomposed N_2H_4 arcjet, even with a non-optimized PCU. The re-start capability of flight units should more than meet any duty cycle requirements. And finally, it was shown for the first time that a N_2H_4 arcjet could be stably maintained over a broad operating range.

3.3.3 Materials Testing

Anodes of identical geometry made of tungsten, tungsten/25% rhenium (W/25 Re), molybdenum/41% rhenium (Mo/41 Re), and pure rhenium were operated on catalytically decomposed N_2H_4 to evaluate the chemical compatibility of these materials. The rhenium alloys were selected because of their demonstrated resistance to oxidation observed during previous resistojet work at RRC. Each anode had a .076 cm diameter by .076 cm length constrictor, a 20 degree half-angle, 50:1 expansion ratio nozzle, and was run with a .043 cm gap. Cathodes made of 2% thoriated tungsten were used for all tests. Table 3-6 summarizes the tests performed.

Table 3-6
MATERIALS TESTS SUMMARY

TEST ID	TEST 2.1	TEST 5.2	TEST 6.1	TEST 7.1
ANODE MAT'L	W	W/25% Re	Mo/41% Re	Re
Power, W	1,100	2,000	1,900	1,850
Voltage, V	104	100	95	100
Current, A	11	20	20	18.5
Flow Rate, kg/sec	5×10^{-5}	6.4×10^{-5}	6.8×10^{-5}	5.9×10^{-5}
Gap, cm	0.043	0.043	0.043	0.043
Test Duration, hrs	8	8	8	6.5

The first test was conducted with a pure tungsten anode at 1,100 W for eight hours. No chemical erosion was found. Figure 3-16 shows the anode and cathode from this test. The power level was increased to about 2000W for the remaining three tests in an attempt to induce some chemical effects.

A principle result of these tests is that almost no evidence of chemical erosion was observed for the tungsten and W/25 Re materials. Figure 3-17 shows the upstream and downstream faces of the W/25 Re anode. Some startup erosion is evident. The constrictor appears oval because of the viewing angle. In particular, the approximately 1% H₂O content of the hydrazine did not cause any oxidation. Some surface depositions were seen on the upstream surfaces of the Mo/41 Re and pure rhenium anodes. Auger electron spectroscopy analyses of the surfaces indicate the material to have some carbon, boron, and calcium present. The latter two came from the boron nitride insulators. No deposition or chemical erosion was found in the constrictor or nozzle with any of the materials.

A second result is that startup erosion is very dependent on the melting point of the material. Figure 3-18 shows a substantial amount of melting erosion of the Mo/41 Re anode which has the lowest melting point (2,550°C). All tests used the same starting procedure. A properly designed PCU may eliminate this erosion. However, there was no evidence to support choosing any of the materials over pure tungsten, which is the most resistance to startup effects. Tungsten was kept as the anode material of choice until such time as multi-hundred hour N₂H₄ arcjet erosion data is made available during Phase II of this program.

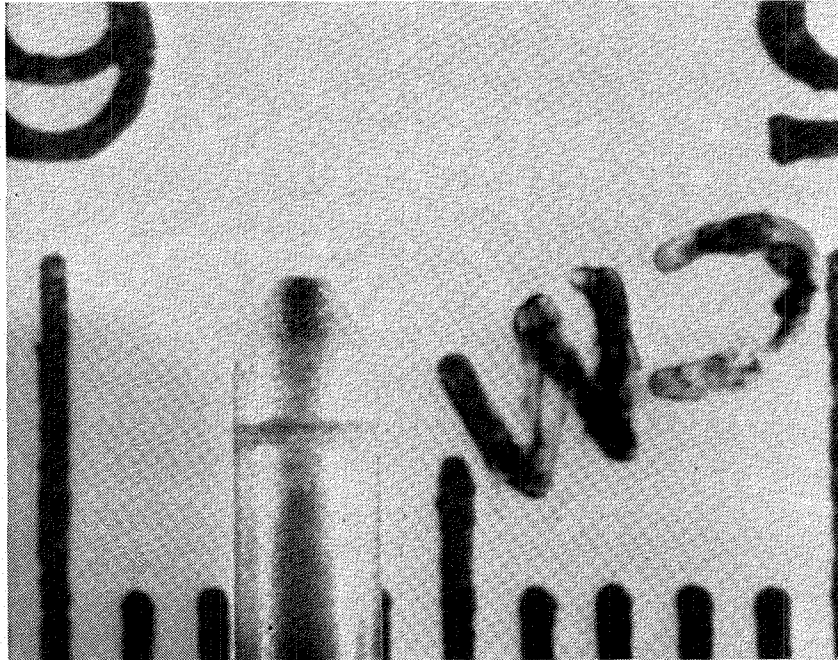
3.4 PERFORMANCE TESTING

An extensive performance testing program was conducted to evaluate the impact of design features on specific impulse and efficiency. All of the data were taken using catalytically decomposed N₂H₄ in the thruster described in section 3.2, Design/Fabrication/Assembly.

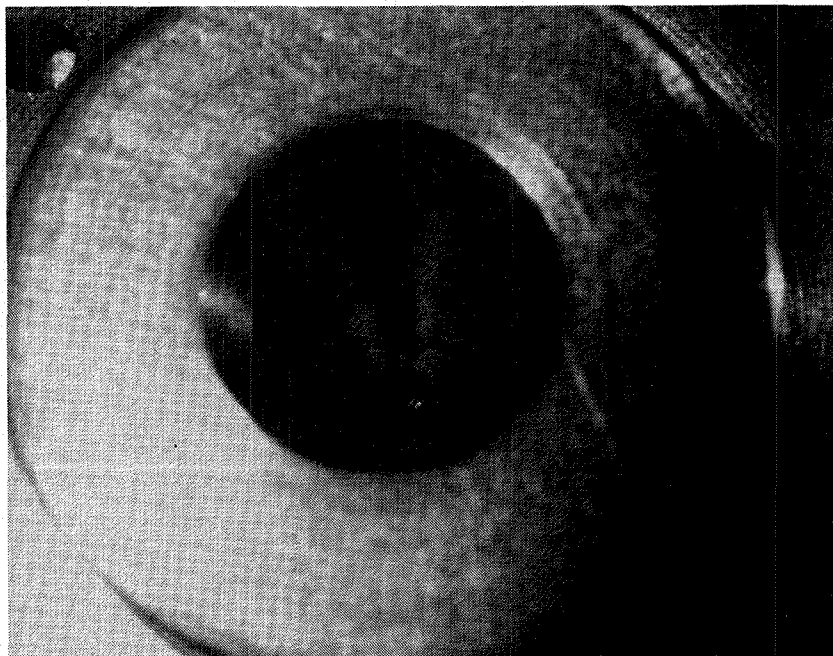
3.4.1 Facility

All performance testing was done in Cell 10 of RRC's Electric Propulsion Test Facility, shown in Figure 3-19. This vacuum chamber is 2.44m in diameter and 2.44m long, made of mild steel, and is fully water jacketed to enable long term high power arcjet testing. Seven 25.4 cm diameter flanges in the chamber side walls provide instrumentation, power, and visual access to the chamber interior. A 45.7 cm diameter flange and piping connect the chamber to a Stokes 1726 vacuum pump. This has a capacity 13,400 cfm. At a

CATHODE AND ANODE, 8 HOUR STEADY STATE, TEST 2.1

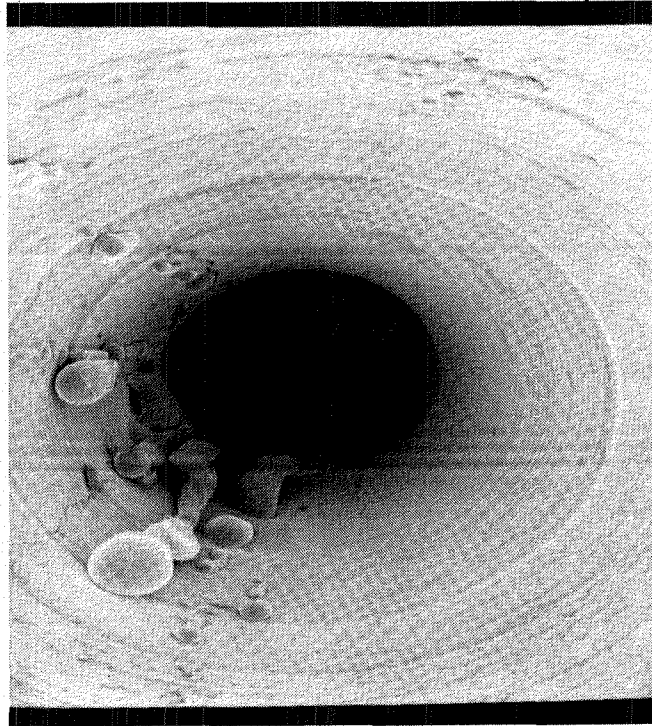


0.178 cm DIAMETER 2% Th/W CATHODE

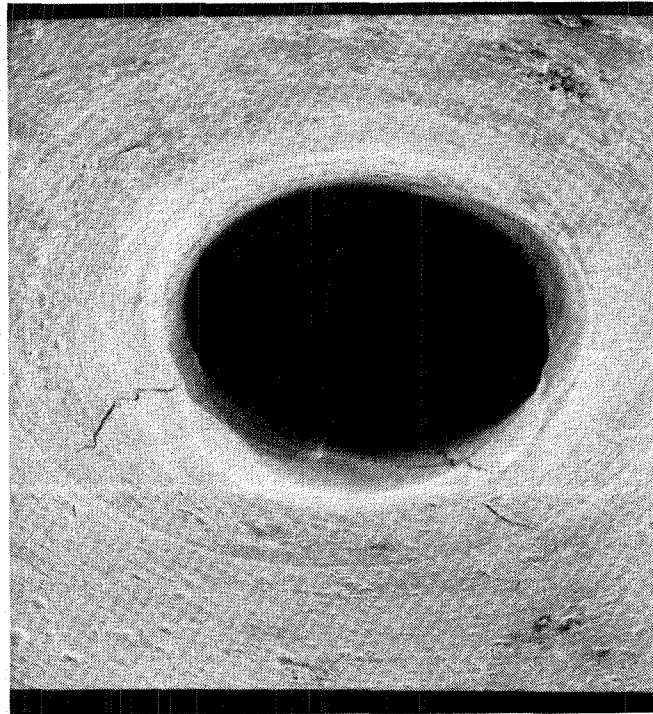


VIEW INTO W ANODE/NOZZLE DOWNSTREAM OF
0.076 cm DIAMETER CONSTRICTOR

W/25 Re ANODE, TEST 5.2



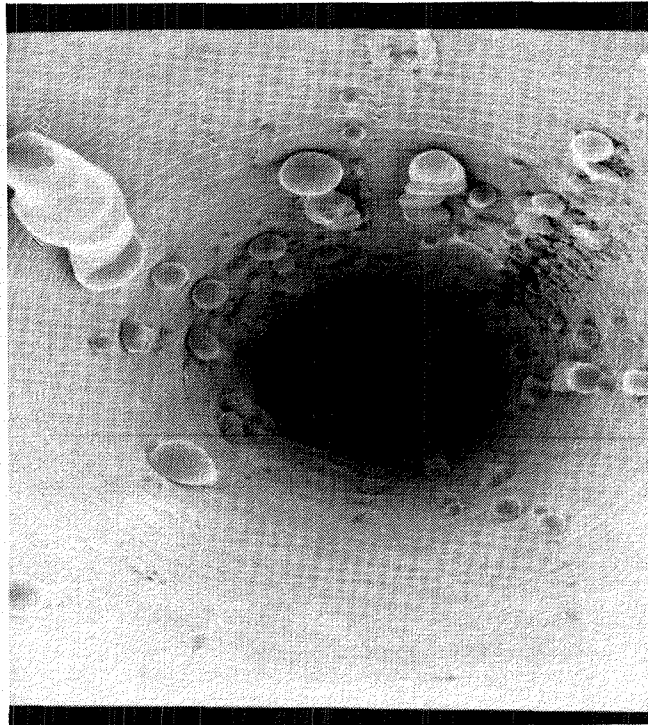
DOWNSTREAM, 50X



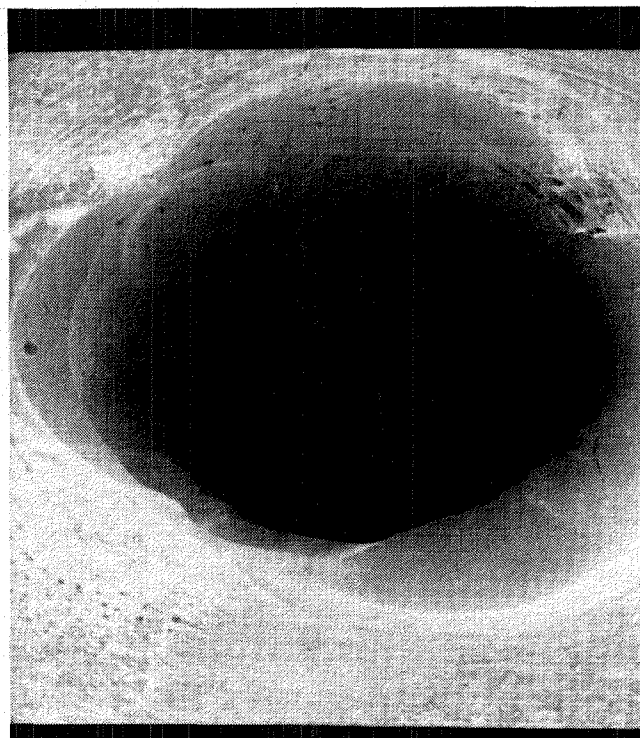
UPSTREAM, 70X

MOLY/41 Re ANODE, TEST 6.1

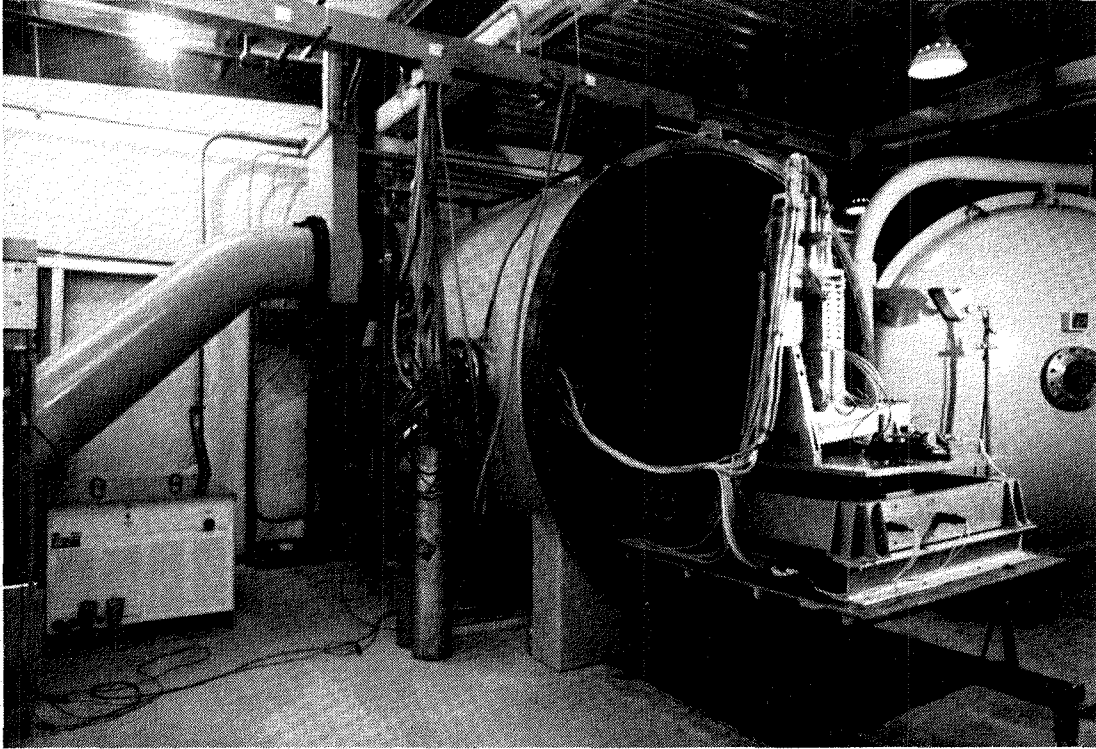
DOWNSTREAM, 30X



UPSTREAM, 70X



ELECTRIC PROPULSION TEST FACILITY, CELL 10



2992-2

maximum N_2H_4 flowrate of 6.8×10^{-5} kg/sec and at 2 kW, the vacuum level is less than 50 mTorr. This results in a vacuum pressure to thruster chamber pressure of about 1×10^{-5} . Studies of vacuum effects on thrust for low Reynold's number nozzles indicate that no degradation of the measured thrust would occur at this ratio.¹¹

The propellant feed system was the same as described in paragraph 3.3.1.

Thrust is measured using the stand shown in Figure 3-20. This stand incorporates the propellant and power feed lines as torsional flexures on the swing axis to eliminate hysteresis. A linear actuator is calibrated in a separate fixture prior to installation on the stand. The position of the stand is monitored by a LVDT located at the end of the arm. A feedback loop causes current to be supplied to the linear actuator to produce zero displacement of the arm. This current is then compared with the calibration and converted to thrust. The stand is accurate to within $\pm 1.5\%$ at 0.22 N (50 mlbf).

A Sorensen DCA 150-70 power supply was again used with a variable 2.0 to 4.3 ohm ballast resistor connected in series with the arcjet. Startup was accomplished with a separate capacitive circuit using an overvoltage technique to establish a Paschen breakdown. This was the same power setup as was used during operational testing.

The data was recorded on strip charts and on a fast sampling digital data system. Pre-and post-test zeros of thrust, flow rate, and of the pressure transducers were taken. During a performance mapping test, a 30 second sample was taken on the digital system. The operating point was then changed by varying current or flow rate, the arcjet was allowed to return to thermal equilibrium, and the next data set was taken.

3.4.2 Test Configurations

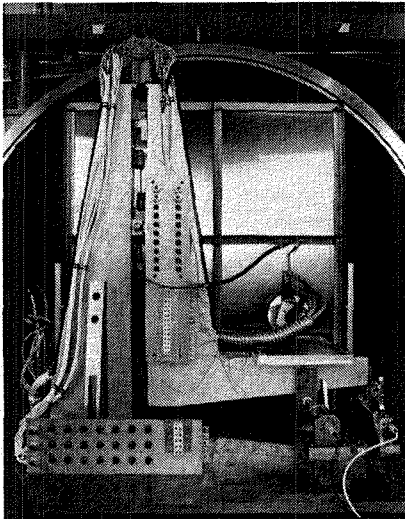
Performance mapping was conducted for each of the configurations listed in Table 3-7. These configurations were chosen to determine the effects of constrictor length, constrictor diameter, cathode/anode gap, and vortex strength on performance. The nozzle was fixed at a 20° half-angle and a 50:1 expansion ratio.

3.4.3 Results/Discussion

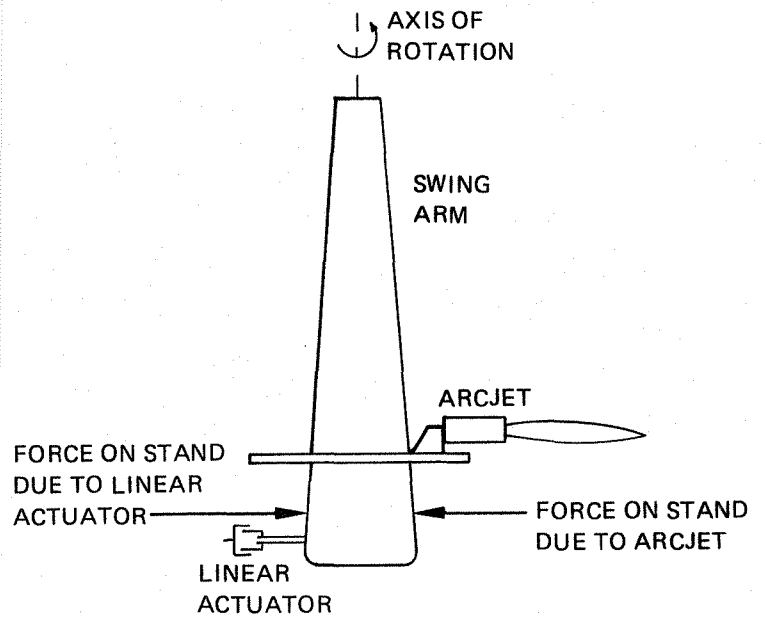
Test Data

The data from the performance tests are found in Appendix D. An index to the plots is given in the Appendix. Graphs were prepared of I_{sp} vs. power divided by flow rate (P/\dot{m}),

NULL BALANCE THRUST STAND



2992-28



Isp versus catalyst bed chamber pressure (P_c), voltage vs. current, thrust vs. P/\dot{m} , and efficiency vs P/\dot{m} .

Table 3-7
PERFORMANCE TEST CONFIGURATIONS

<u>Test #</u>	<u>Constrictor Length (cm)</u>	<u>Constrictor Diameter (cm)</u>	<u>Gap Setting (cm)</u>	<u>Injector Port Area (cm²)</u>
9.2	0.076	0.076	0.038	2.68×10^{-2}
10.2	0.000	0.076	0.038	2.03
12.1	0.000	0.076	0.038	1.30
14.1	0.051	0.058	0.025	2.68
16.2	0.152	0.076	0.046	2.03
17.1	0.076	0.076	0.046	1.30
18.4	0.076	0.076	0.046	2.03

Nozzle half angle = 20° , $\epsilon = 50$

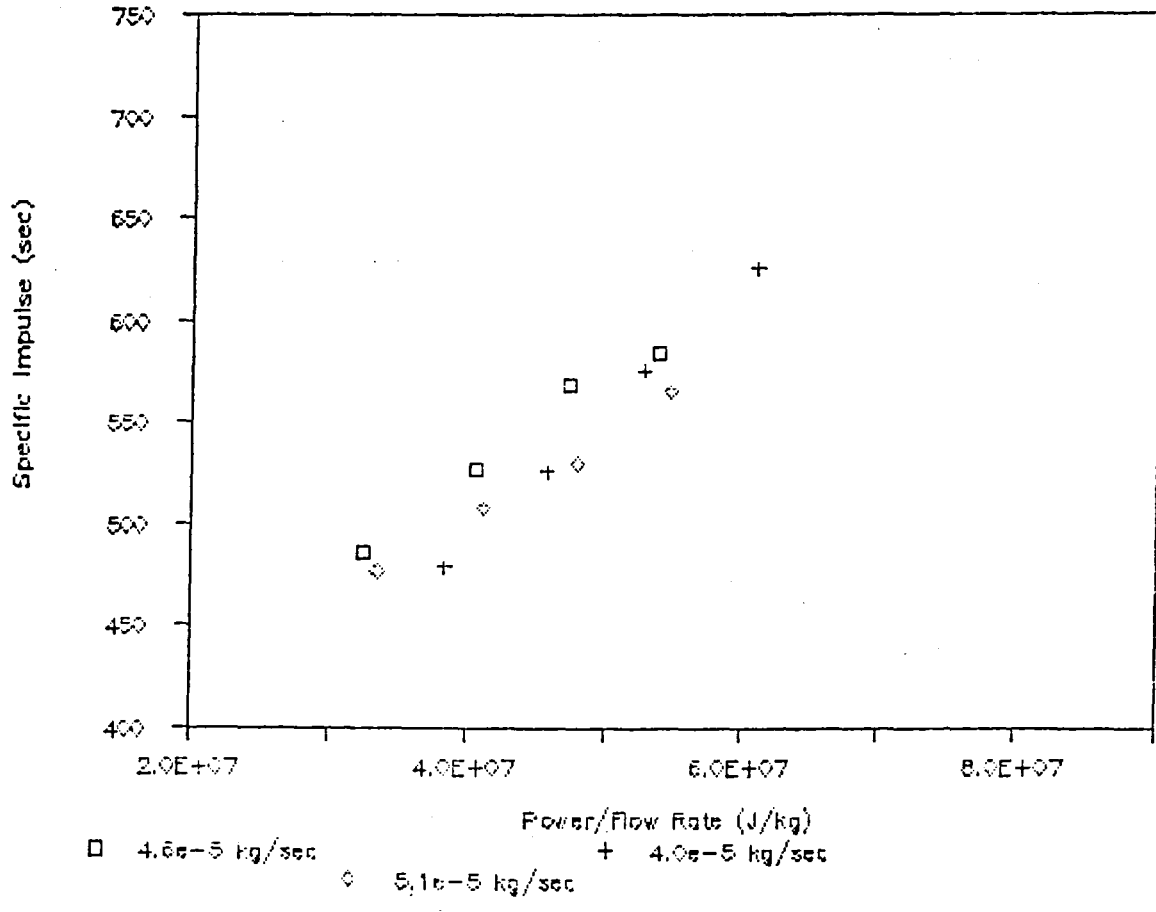
A typical set of data are shown in Figures 3-21, 3-22, and 3-23 for Isp versus P/\dot{m} , Isp versus gas generator pressure, and thrust versus P/\dot{m} , respectively. For the same ratio of P/\dot{m} , there were only small differences in the measured specific impulse values, regardless of the configuration. Figure 3-24 shows a curve fit of all the performance data taken. The data generally fell within ± 20 seconds Isp for a given value of P/\dot{m} . Often the differences were within the experimental uncertainty of the tests. Values of Isp to 730 sec were produced for the .058 cm diameter constrictor at a power level of 2640 W and a thrust of 0.227N.

Specific impulse correlated well with the catalyst bed chamber pressure. This pressure is a function of the flow rate and the degree to which the arc chokes the flow through the constrictor. Figure 3-22 shows that at a constant flowrate of 4.0×10^{-5} kg/s, increasing the current from 20.2 A to 35A increases the chamber pressure by 5 psia. Conversely, at a fixed current of 20A, increasing the flow rate from 4.0×10^{-5} kg/s to 4.6×10^{-5} kg/s increases the chamber pressure by 10 psia.

Figure 3-25 shows the variation in the arc voltage/current characteristic with constrictor length at the same flow rate of 4.5×10^{-4} kg/s. At 20A, the "zero" length voltage is 77V, the 0.076 cm length constrictor produces 87V, and the 0.150 cm length results in 100V. This is equivalent to a roughly 150 V/cm increase as a result of lengthening the

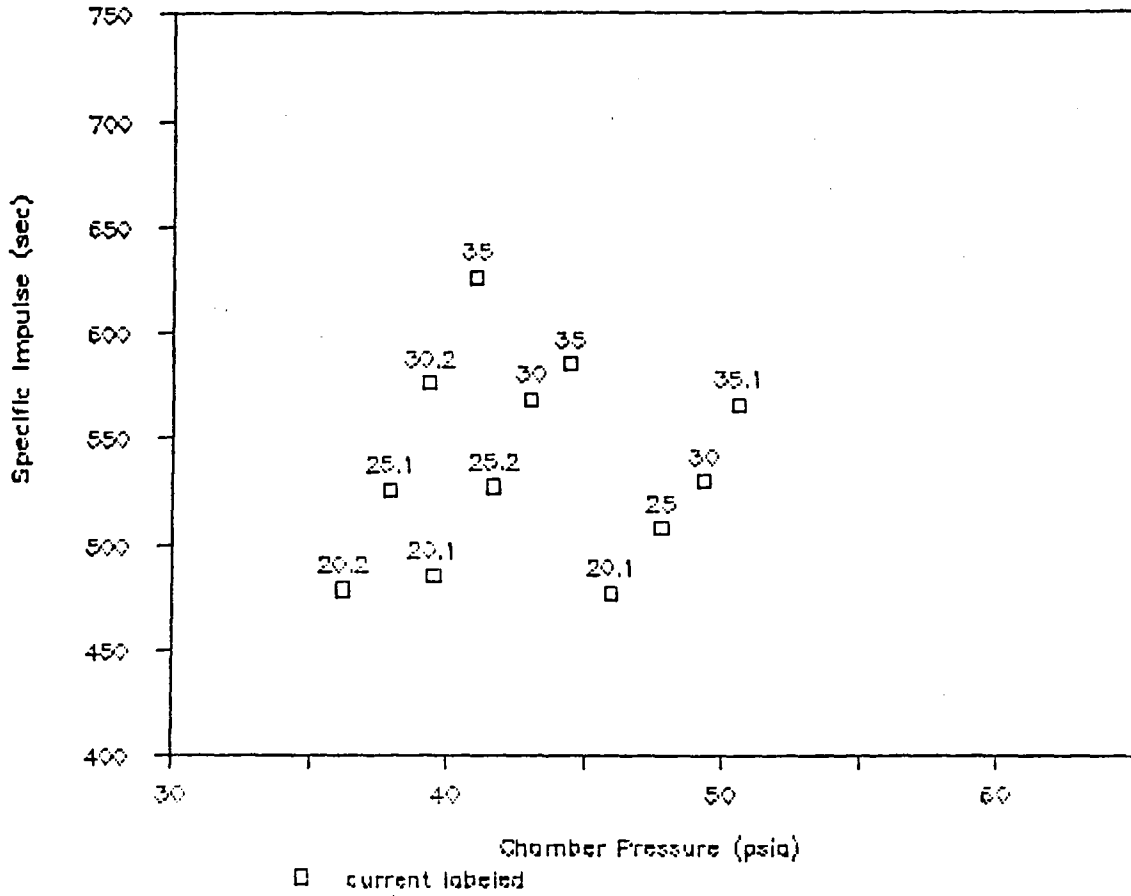
Specific Impulse vs. Power/Flow Rate

Test 10.2



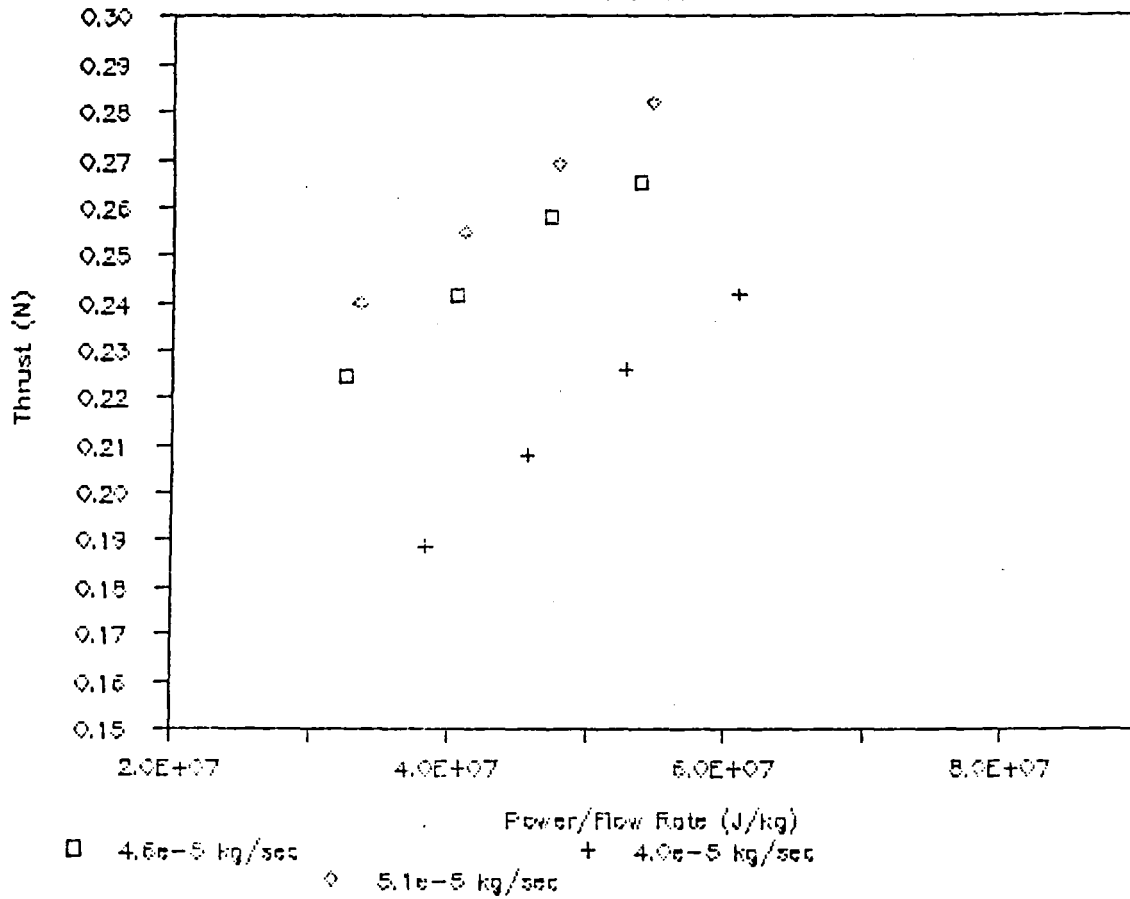
Specific Impulse vs. Chamber Pressure

Test 10.2

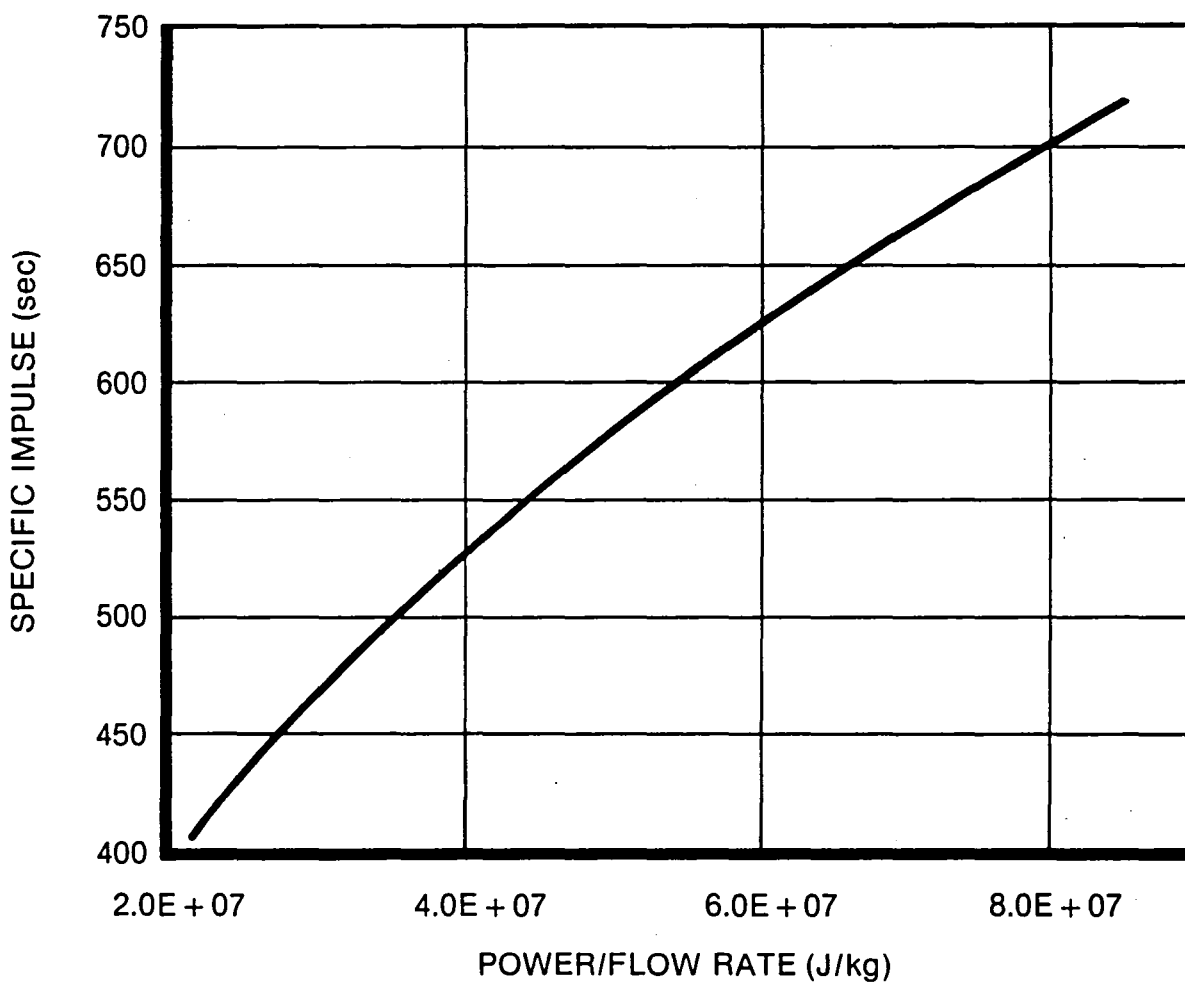


Thrust vs. Power/Flow Rate

Test 10.2

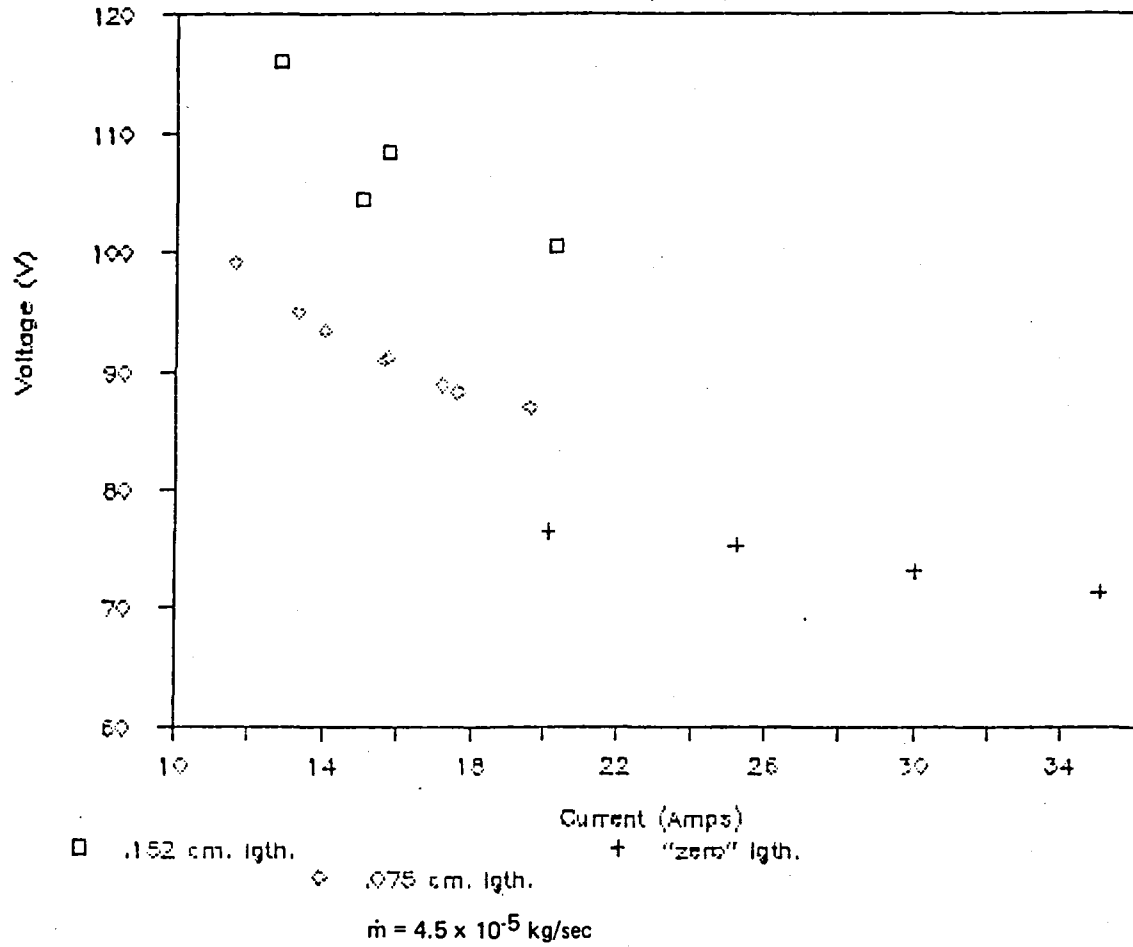


N₂H₄ Arcjet Performance Curvefit Based on Test Data, 1000 — 2800 W



Voltage vs. Current.

Tests 10.2, 16.2, 18.4



constrictor. However, this does not noticeably effect the relative performance at the same P/\dot{m} .

Figure 3-26 shows voltage vs. current for the same electrode configuration at approximately the same flow rate of 4.5×10^{-5} kg/sec but with different vortex injectors. Test 17.1 had an injector port area of 1.30×10^{-2} cm², test 18.4 was 2.03×10^{-2} cm², and test 9.2 was 2.68×10^{-2} cm². There is little difference between the three V-I traces. The voltage for test 9.2 was 3-4 V less than the other curves. The vortex does not strongly effect the V-I relation.

Referring again to Figure 3-23, thrust versus P/\dot{m} is given for the "zero" length constrictor of test 10.2. At a constant flow rate of 4.6×10^{-5} kg/sec, increasing the current from 20A to 35A increases the thrust from 0.227N to 0.267N. This corresponds to a power increase from 1,540 W to 2,500 W.

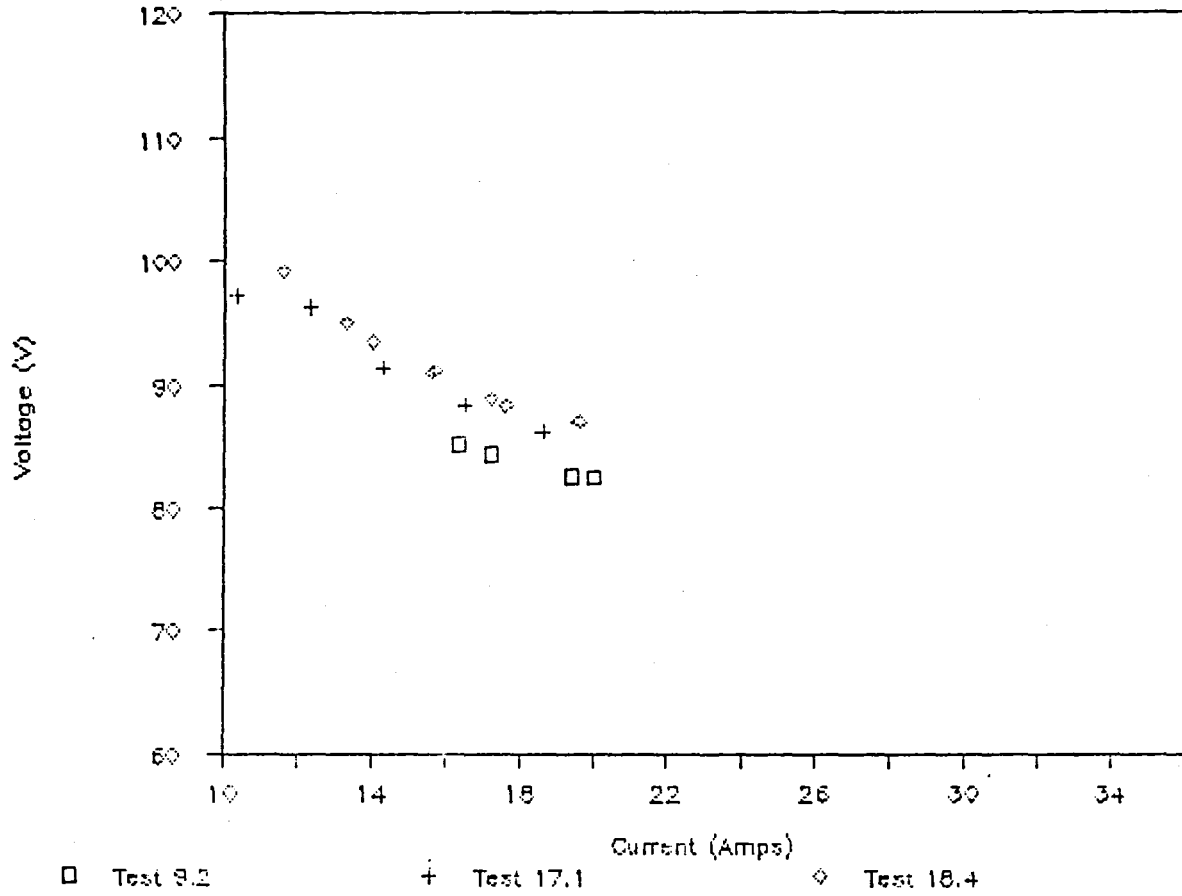
Figure 3-27 gives overall efficiency versus P/\dot{m} for test 18.4. At a P/\dot{m} ratio of 4.0×10^7 J/kg, going from 4.0×10^{-5} kg/sec to 4.9×10^{-5} kg/sec causes an increase in efficiency from 31 to 32.5%.

Total efficiency from test 18.4 is plotted against the catalyst bed chamber pressure in Figure 3-28, with the current levels shown above the data points. At 4.0×10^{-5} kg/sec, going from 12 to 20 amps (1,150 to 1,650 W) causes a decrease in the efficiency from 33 to 30%. At 18A, increasing the flow rate from 4.0×10^{-5} to 4.9×10^{-5} kg/sec causes an increase in the efficiency from 30.5 to 33%.

Figure 3-29 shows a comparison of the efficiency versus P/\dot{m} relation for tests 14.2 and 18.4. It is evident that efficiency is dependent on parameters other than the P/\dot{m} ratio. If the trend for the 0.075 cm diameter constrictor of test 18.4 applied to the .058 cm throat of test 14.2, the latter's efficiency would be less than 0.30. A possible explanation for the shift is found in the fact that the catalyst bed pressure is 10-15 psia higher at the same flow rate and current for the smaller throat. This may favor higher nozzle and thermal efficiencies.

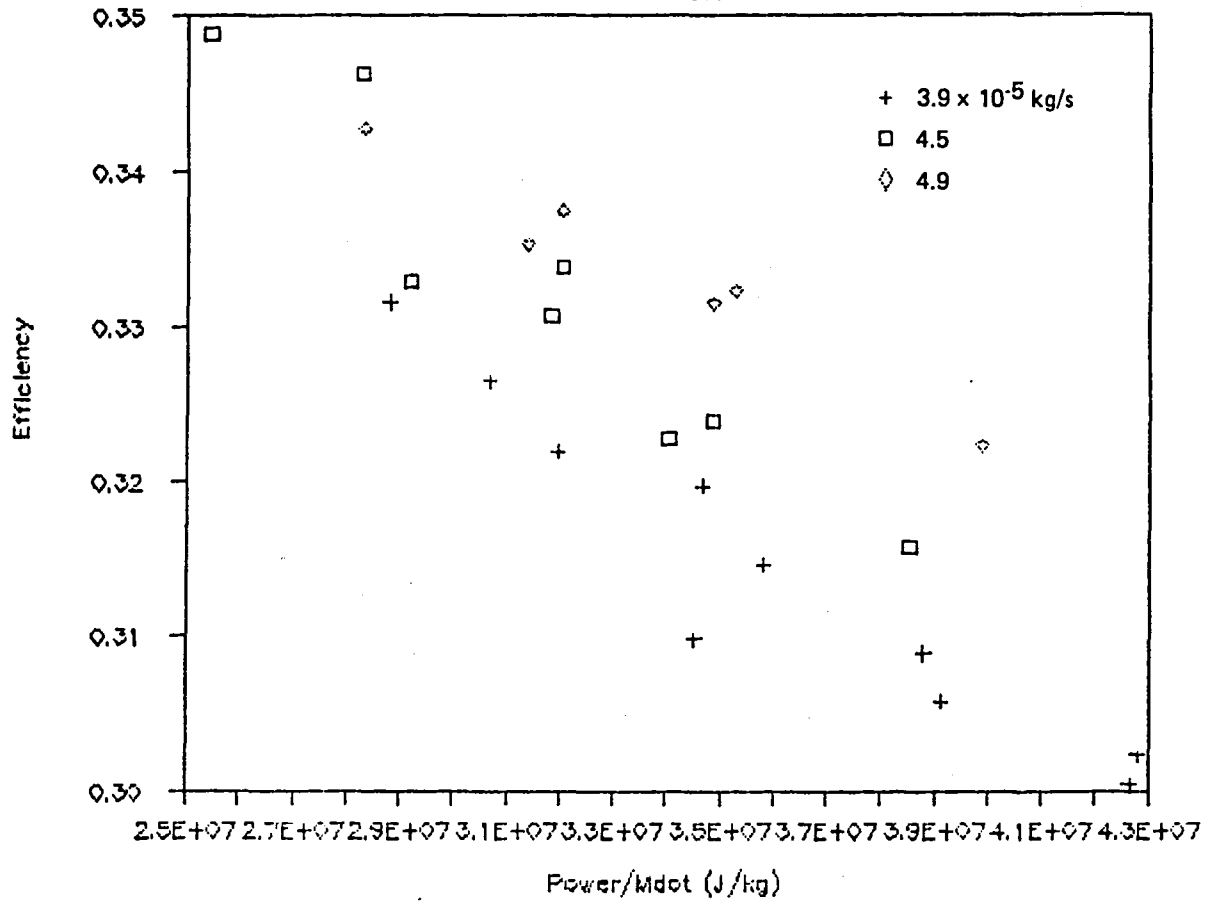
Voltage vs. Current

Tests 9.2, 17.1, 18.4

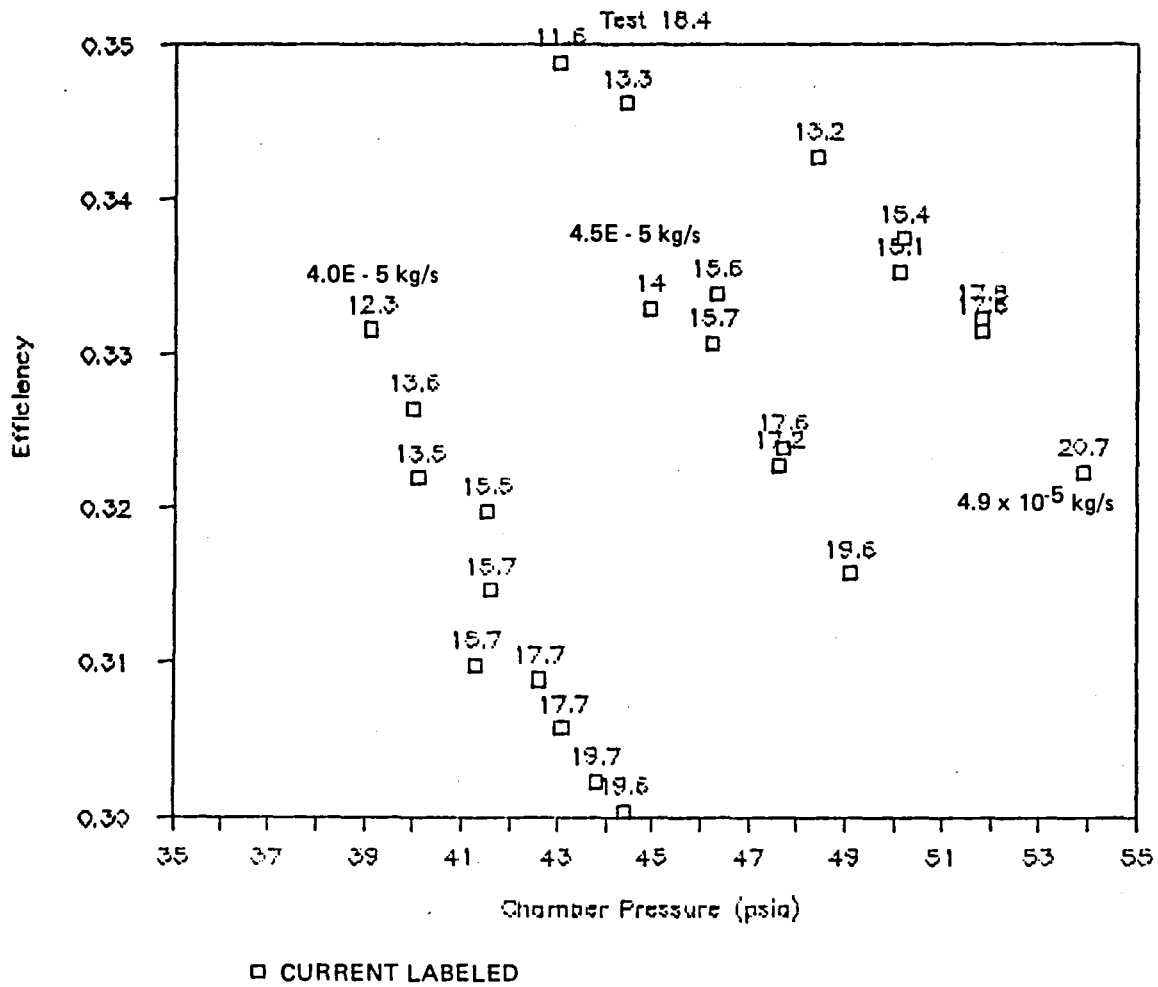


Efficiency vs. Pow/Mdot

Test 18.4

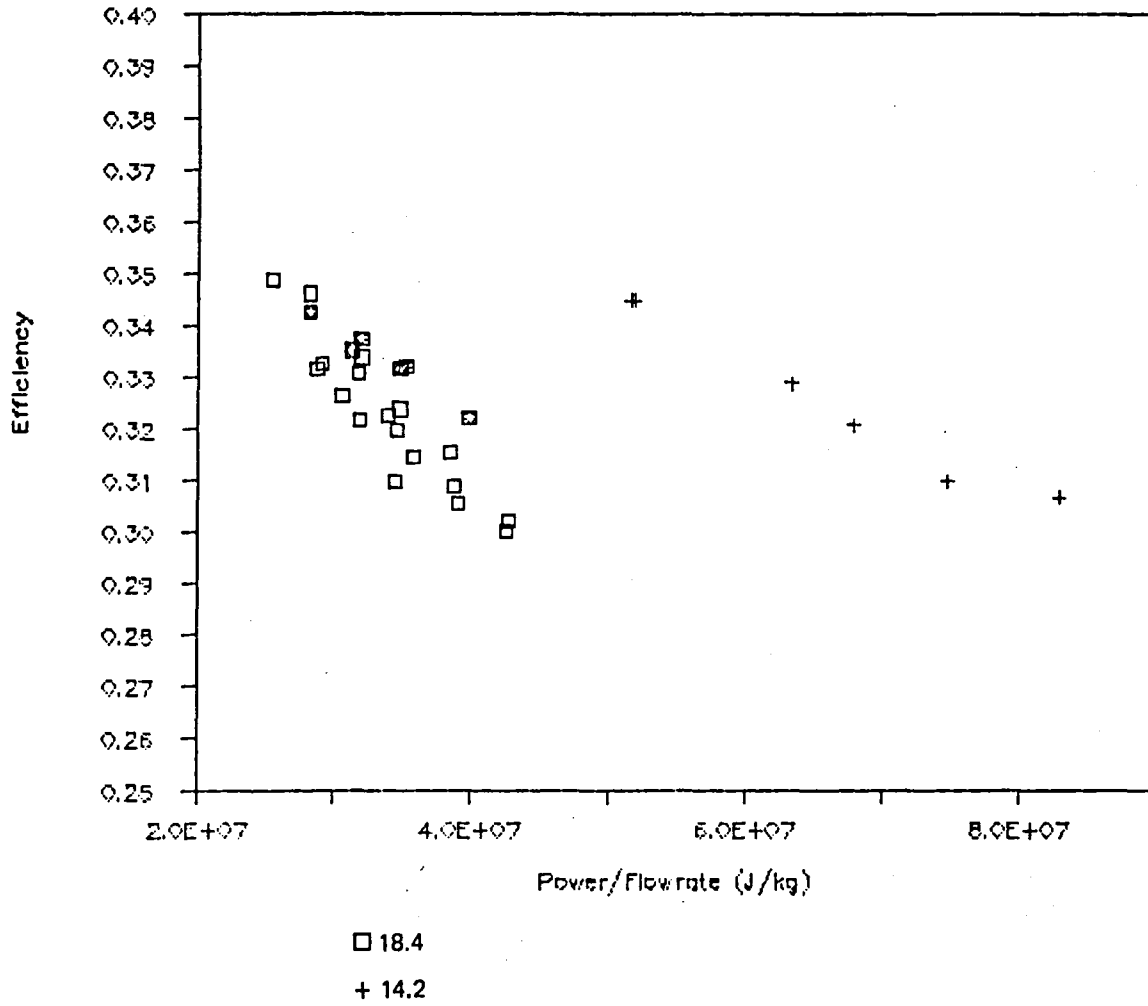


Efficiency vs. Chamber Pressure



Efficiency vs. Power/Flowrate

Tests 14.2 & 18.4



3.4.4 Efficiency Analysis

Overall arcjet efficiency was broken down into four components: thermal, frozen flow, geometric, and nozzle. The product of the component efficiencies equals the overall arcjet efficiency,

$$\begin{aligned}\eta_T &= \eta_{Th} \eta_{FF} \eta_G (\eta_N)^2 \\ &= 1/2 \frac{\text{Thrust}^2}{(IV + \dot{m} h_o) \dot{m}}\end{aligned}$$

where h_o = decomposition gas inlet enthalpy.

The component efficiencies are briefly described below.

Thermal efficiency is a measure of the fraction of the total input power which is lost through the thruster structure. It was estimated by using thruster temperature data in the thermal model described in paragraph 3.1.5, Thermal Modelling.

Frozen flow efficiency is a measure of the fraction of gas enthalpy which is available for thrust (i.e., gas enthalpy not tied up in dissociation or ionization). NASA's CEC program was used to estimate trends in frozen flow efficiency with gas enthalpy.

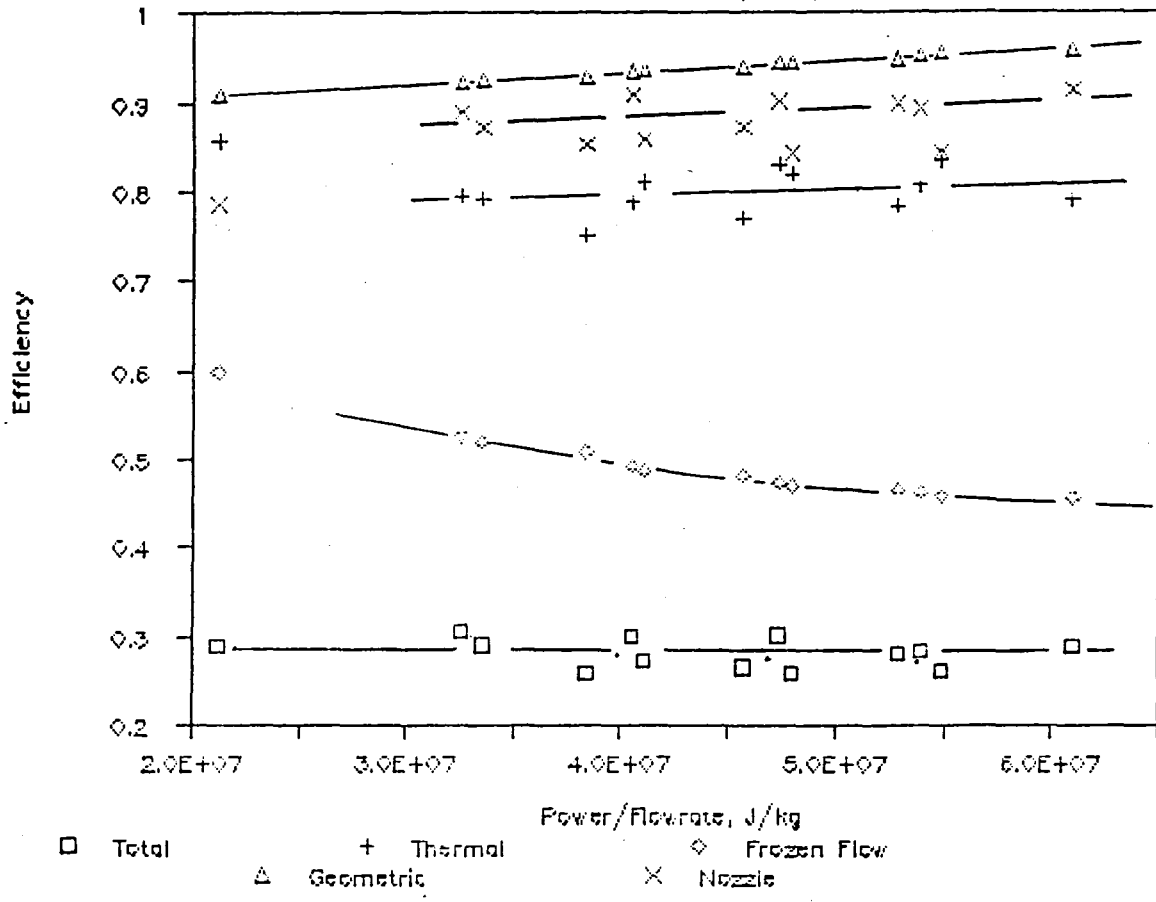
Geometric efficiency is a measure of the losses due to incomplete expansion by the nozzle. The NASA CEC program was also used to estimate this efficiency.

Nozzle efficiency is a measure of the viscous and divergence (or cosine) losses. Nozzle efficiency is calculated using equation 1 by inserting the other calculated and measured efficiencies. The nozzle efficiency is conventionally defined as a specific impulse ratio, not as an enthalpy ratio. Since $I_{sp} \sim h^{1/2}$, the nozzle efficiency is squared in this relation so that each term represents an enthalpy ratio.

A summary of the various component efficiencies for tests 10.2 and 18.4 is shown in Figures 3-30 and 3-31. In both, the measured overall efficiency remains relatively constant with P/\dot{m} . The inlet enthalpy term $\dot{m} h_o$ in the denominator reduces the overall efficiency by 2 to 5% from the value calculated by $\eta_T = \frac{1/2 T^2}{IV \dot{m}}$, which is used for the performance graphs of section 3.4.3.

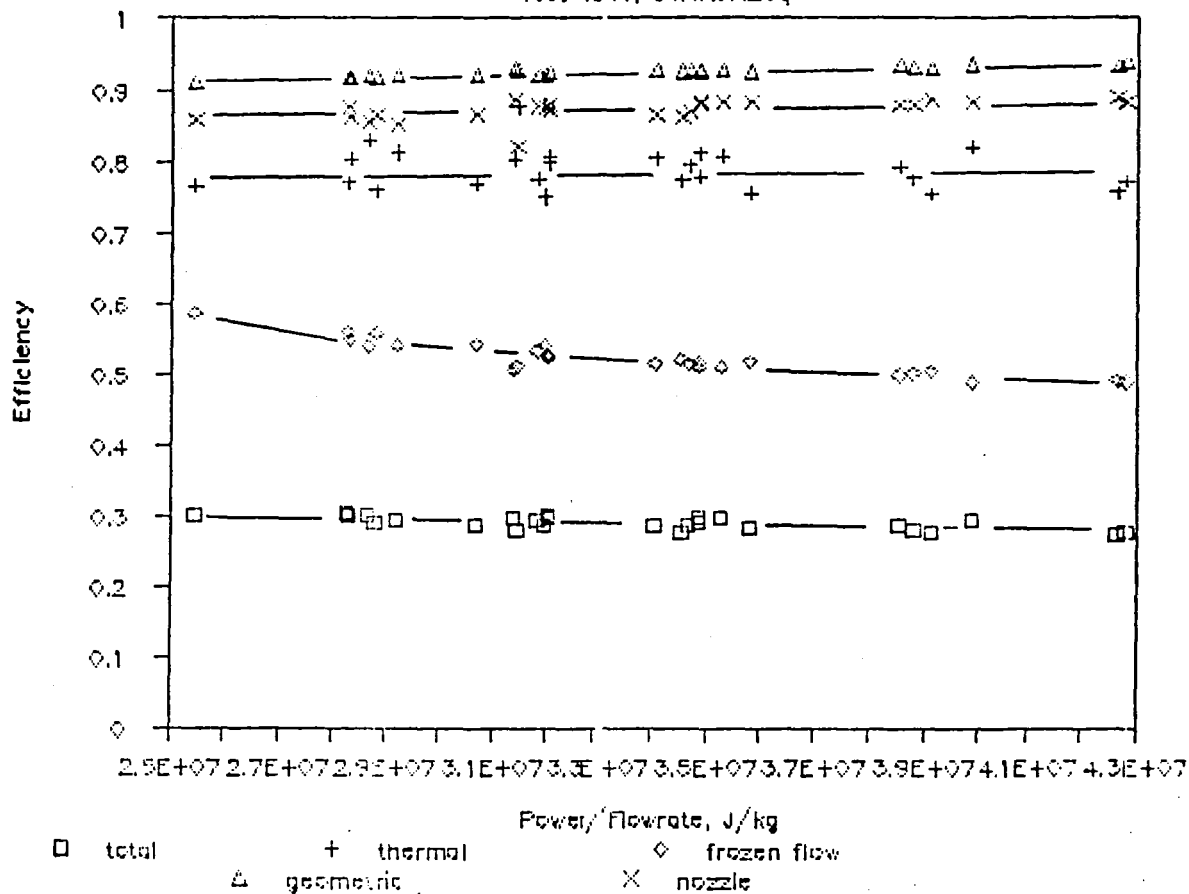
Efficiency vs Power/Flowrate, J/kg

Test 10.2, 80NH3/H2eq



Efficiency vs Power/Flowrate

Test 18-4, 80NH3H2eq



Figures 3-30 and 3-31 show that frozen flow effects and the nozzle cause the largest losses in the low power arcjet. For both test 10.2 and test 18.4, the product of these two is less than 44%. Unfortunately, the governing phenomena for these two are also the most difficult to diagnose and analyze. The CEC program can be used to predict frozen flow losses. The main flaw in the use of the CEC program is that it is a 1D bulk analyzer and the arcjet is a 2D phenomenon. A hand calculation based on estimated temperature and mass flux profiles for an arcjet was made to compare with the CEC results. The flow was divided into two parts, the arc core and the surrounding flow. The arc core was assumed to be in species equilibrium at 20000K and the outer flow frozen at the species concentrations exiting the gas generator (11% NH_3 , 22% N_2 , 67% H_2). The equilibrium species data for the arc core were estimated using theoretical data.^{2,3} The core flow was assumed to be less than 10% of the total. The hand calculated results indicate that frozen flow losses could account for a major portion of the combined frozen/nozzle losses.

Figure 3-30 and 3-31 also show geometric efficiency as a function of P/\dot{m} . Geometric efficiency is generally greater than 90%. It increases with P/\dot{m} due to the dissociation of heavier, lower specific heat ratio species. The geometric efficiency was calculated with the CEC program.

Figures 3-32 and 3-33 show thermal efficiency as a function of current for tests 10.2 and 18.4, respectively. Both arcjet configurations demonstrate the same increasing thermal efficiency trend with current.

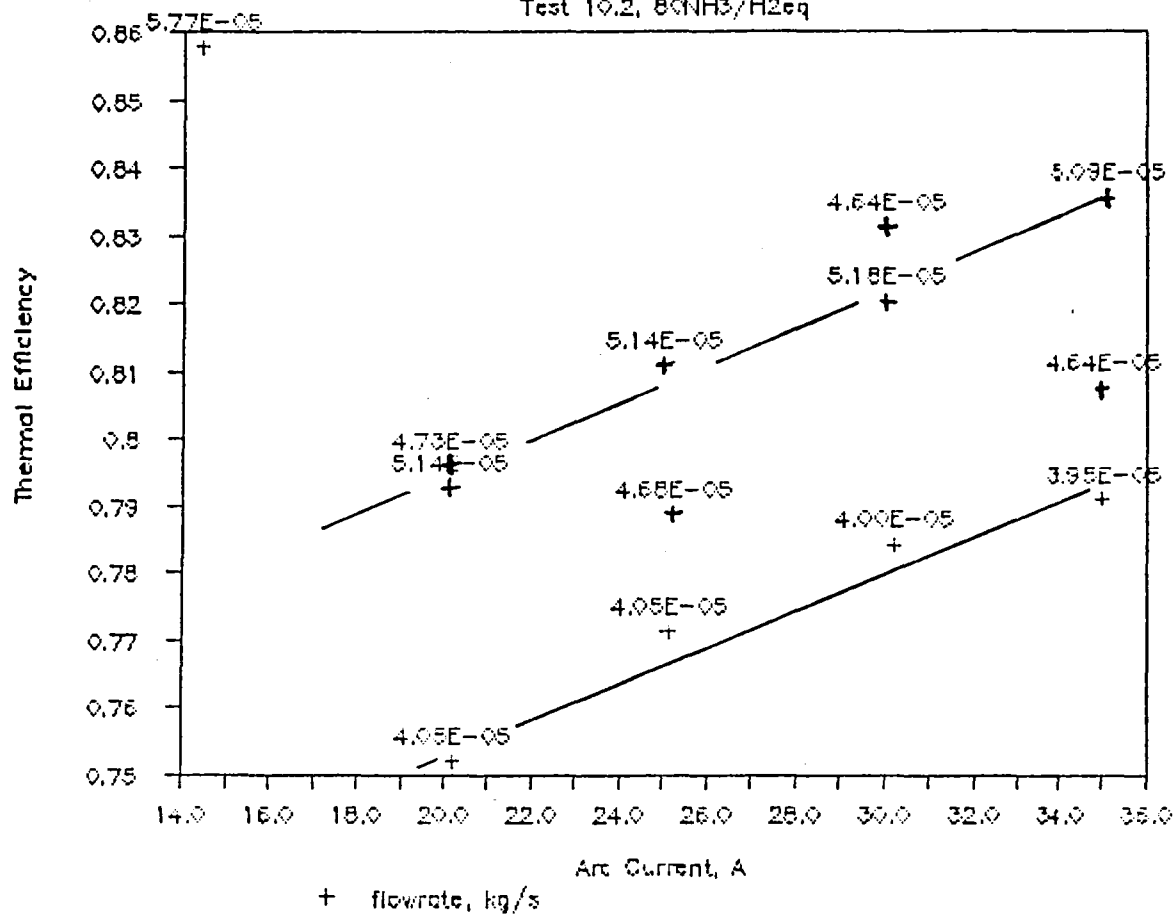
This suggests that the heat transfer at the anode fall zone decreases with increasing plasma density. While this may be nonintuitive, it is consistent with accepted descriptions of the anode fall zone. In this zone, a potential develops near the surface to accelerate the electrons to a high enough kinetic energy to create ions to maintain the electrically neutral plasma through collisions with neutrals. Those electrons not colliding carry their kinetic energy and thermal energy into the anode surface. As the plasma densities increase through either increased pressures or magnetic self-constriction, the collision cross sections increase, and fewer electrons reach the surface without colliding with neutrals. The energy removed by the collisions decreases the electron energy flux to the surface.

3.4.5 Performance Test Conclusions

The demonstrated specific impulse levels of from 400 to 730 seconds using catalytically decomposed N_2H_4 were much higher than expected, and are far in excess of existing flight

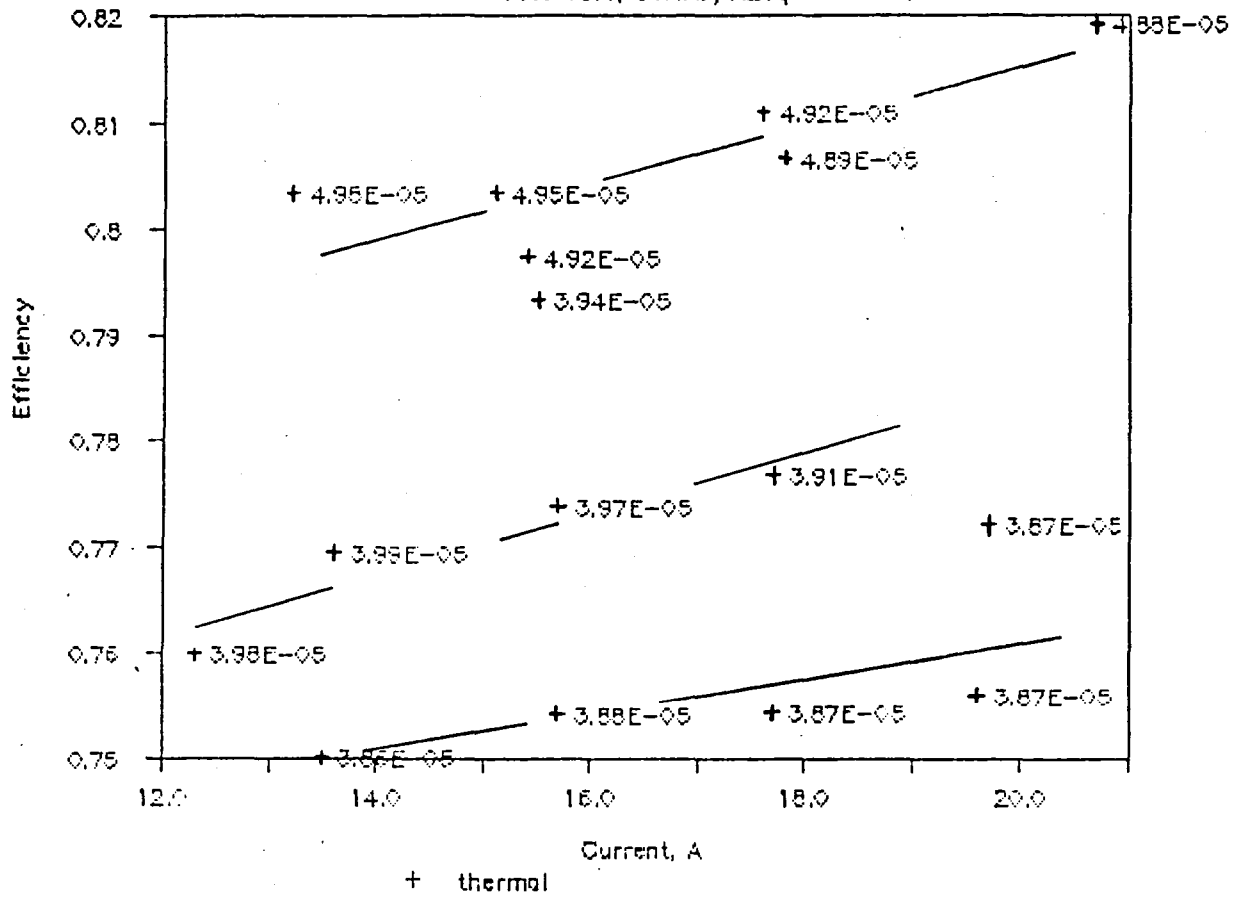
Thermal Efficiency vs Current

Test 10.2, 80NH3/H2eq



Thermal Efficiency vs Current

Test 18.4, 80NH3/H2eq



qualified auxiliary propulsion systems. A nominal level of 500 seconds near the low end of the range measured is 125% higher than a straight N_2H_4 system, 75% higher than a bipropellant thruster, and 67% higher than a N_2H_4 resistojet. Even higher specific impulse levels appear possible since the efficiency had not yet started to rapidly drop off and no high performance failure modes, such as anode spots, were observed.

An important conclusion reached is that the arcjet performance for a given ratio of power to flow rate is not strongly linked to the precise geometry. Three different constrictor lengths, two constrictor diameters, several vortex strengths, and three gap settings were tested in various combinations. No obvious performance advantages were observed. This allows the arcjet to be designed to meet lifetime and operational requirements without sacrificing any performance.

Operational differences were observed. Generally, the shorter constrictors started more easily and were more stable. This was evident by less erosion on startup, by smoother voltage and current traces, and by less noise being picked up by thermocouple lines at the edges of the stable operating range. A possible disadvantage of the more stable, shorter constrictors is that for a given power level, higher currents result from the lower arc voltage. This may effect the cathode erosion rates.

Overall efficiencies measured were 30 to 35%. Frozen flow effects cause the major loss, followed by nozzle and thermal losses. Future technology work focused on improving the efficiency should be able to reduce these losses.

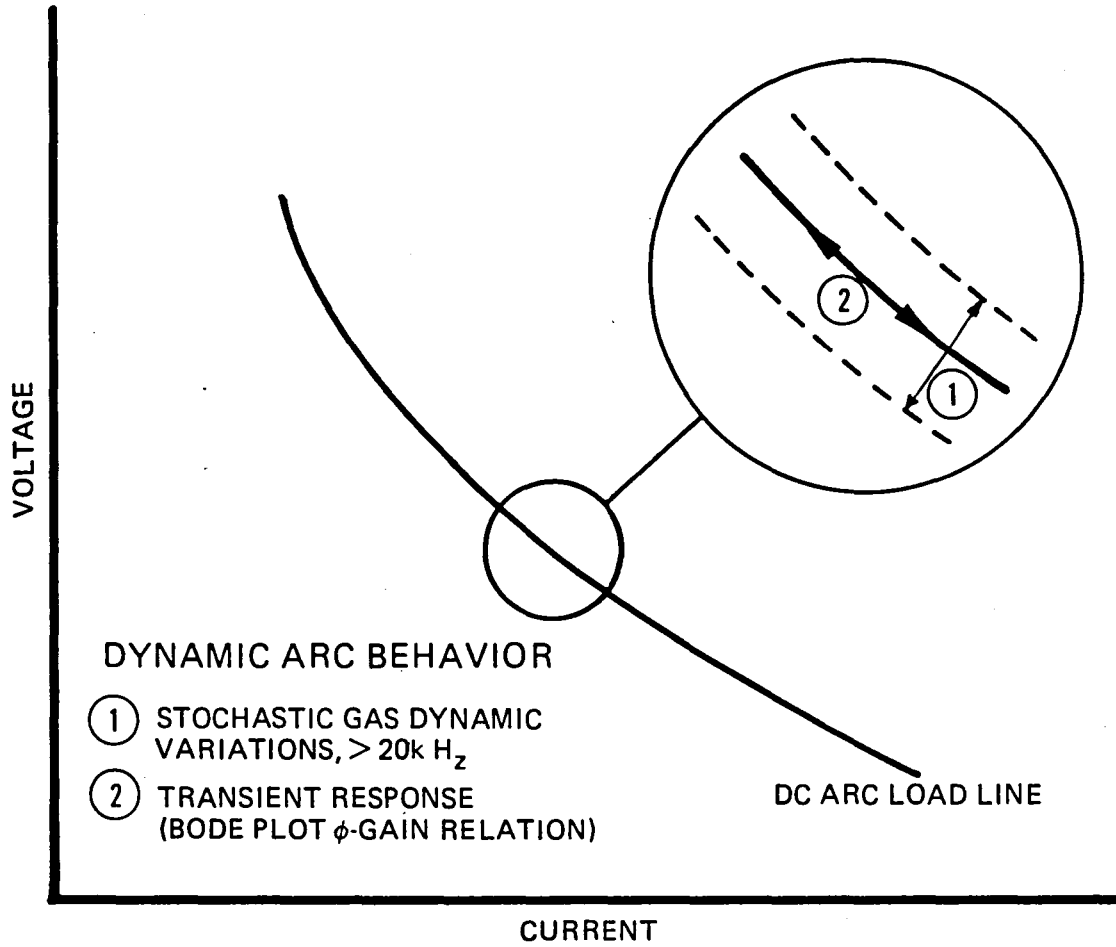
3.5 PCU DEVELOPMENT

3.5.1 Design Requirements

Flight application of a N_2H_4 arcjet requires a power control unit (PCU) capable of starting and stabilizing the arcjet while operating off of a nominally 28 VDC battery system. Starting entails applying a 1500 to 2000 V potential across the electrodes to produce a Paschen breakdown at steady state flow rates. As soon as an ionized path is formed, the PCU must ramp the current up to the steady state value with a minimum current overshoot to prevent anode erosion. The entire starting procedure takes less than 20 msec.

Maintaining steady state arc stability involves satisfying both a DC and a dynamic criterion. The characteristic of the arc is shown in Figure 3-34. The negative

DC/DYNAMIC ARCJET CHARACTERISTICS



characteristic is a result of the lower resistance of the arc at higher currents due to increased ionization. Increasing the flow rate shifts the curve up due to greater arc cooling. Lengthening the constrictor moves the curve up due to a longer arc.

Superimposed on the DC load line are two dynamic effects. For a steady, zero-ripple input current, there are voltage fluctuations caused by movement of the arc attachment point. It is probably due to the gas dynamic forces of the flow and transient heating of the anode attachment point surface. This effect has been observed during high power arcjet tests^{6,7}. Reference 6 reports periodic voltage oscillations in the 100 to 200 kHz range with hydrogen. The investigators reported the phenomenon to be a function of the flow rate, geometry, propellant, and anode material. The tentative conclusion they reached was that turbulence was partially responsible for the oscillations, based on an analysis of the Prandtl and Reynold's numbers. Periodic oscillations have not been observed with the low power N_2H_4 arcjet. There are some apparently random variations in certain modes. This effect can be visualized as a rapid translation of the DC load line.

A second dynamic feature of the arc is its response to a varying input current signal. If the ionization and dissociation times are on the same order as the input signal period, the voltage and current can change their phase relation. At high enough frequencies, the arc can have a positive I-V characteristic. This characteristic is important to the arcjet/PCU system stability design.

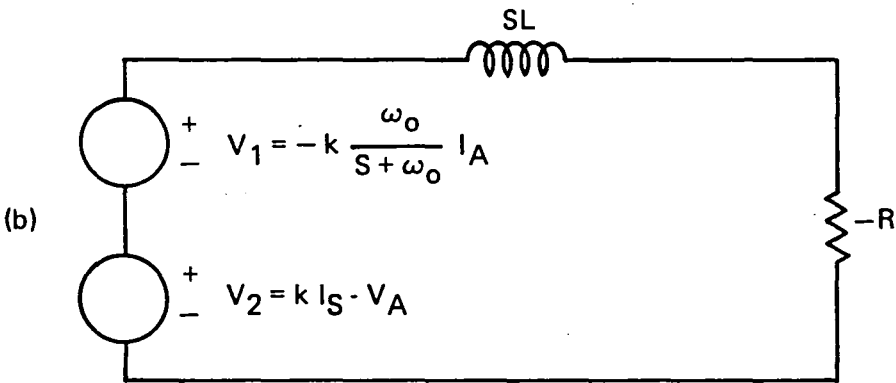
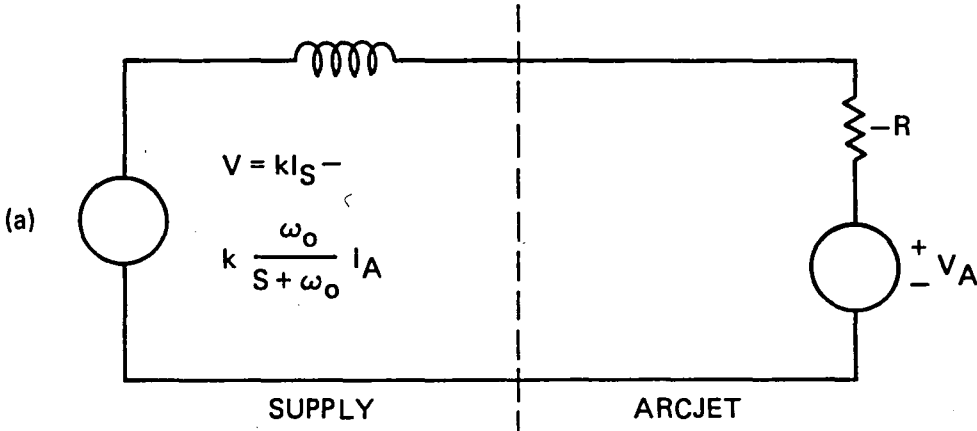
A simplified analysis approach was taken to define these conditions. Figure 3-35 (a) shows a schematic representation of the PCU/arcjet system. The PCU is a voltage source with bandwidth limited current feedback in series with an inductor. This is typical of the circuits used for switch mode power supplies. The voltage of the source is given by:

$$V = I_S - \kappa \left(\frac{\omega_o}{s + \omega_o} \right) I_A$$

where:

- κ = DC impedance of supply
- I_S = current setpoint
- I_A = arc current
- ω_o = feedback loop bandwidth
- s = arc load frequency

SIMPLIFIED PCU/ARCJET SYSTEM



The arcjet is represented as a voltage source in series with a negative resistance R. The value of R is the slope of the D.C. characteristic shown in Figure 3-34. For this analysis, it is assumed that R is constant over a small range of current at the same flow rate.

Rearranging the system elements results in the schematic of Figure 3-35 (b). The following analysis results:

$$V_1 + V_2 = I_A (sL - R),$$

$$-k \left(\frac{\omega_0}{s + \omega_0} \right) I_A + k I_S - V_A = I_A (sL - R)$$

Solving for I_A gives,

$$I_A = \frac{\frac{1}{L} (kI_S - V_A) (s + \omega_0)}{s^2 + s (\omega_0 - R/L) + \frac{\omega_0}{L} (k - R)}$$

For this system to be stable, the real roots of the denominator must have negative real parts. Hence the PCU/arcjet system is stable if:

$$\omega_0 L > R, \quad \text{dynamic stability,}$$

$$\text{and } k > R, \quad \text{DC stability.}$$

This analysis has over simplified both the arcjet and the PCU. It does stress, however, the fact that there is another stability criterion to meet other than the comparison of the DC PCU and arcjet load lines. Work is planned for Phase II to measure the arc's dynamic load characteristic and to perform first order stability analyses.

3.5.2 Design Description

The specification given in Table 3-8 was prepared and sent to several potential suppliers. Space Power, Incorporated was selected to design and fabricate a variable, laboratory PCU. It was decided to relax the voltage step-up requirement at this stage.

A block diagram of the PCU as originally developed is shown in Figure 3-36. The PCU is broken into five functional blocks. They are: the three phase buck regulator, the clock, the comparators, the feedback circuit, and the start circuit.

Table 3-8

BREADBOARD ARCJET LABORATORY PCU SPECIFICATION

1. Current/Voltage Characteristics

1.1 Startup - high voltage pulsing

- 1.1.1 Voltage peak: 600-1500 V
- 1.1.2 Pulse width: 0-50 msec
- 1.1.3 Current ramp-up and crossover: 0- (steady state value) A, varied from 0.1 to 5.0 msec with less than 2% current overshoot.

1.2 Steady State

- 1.2.1 Voltage: 60-150V
- 1.2.2 Current: 5-45A
- 1.2.3 Current fluctuations: less than 1% peak to peak
(current control mode)
- 1.2.4 Response time, t_R : Variable response time t_R , where 10 microsec $< t_R < 100$ microsec (100 KHz to 10 KHz)

2. Operating Features

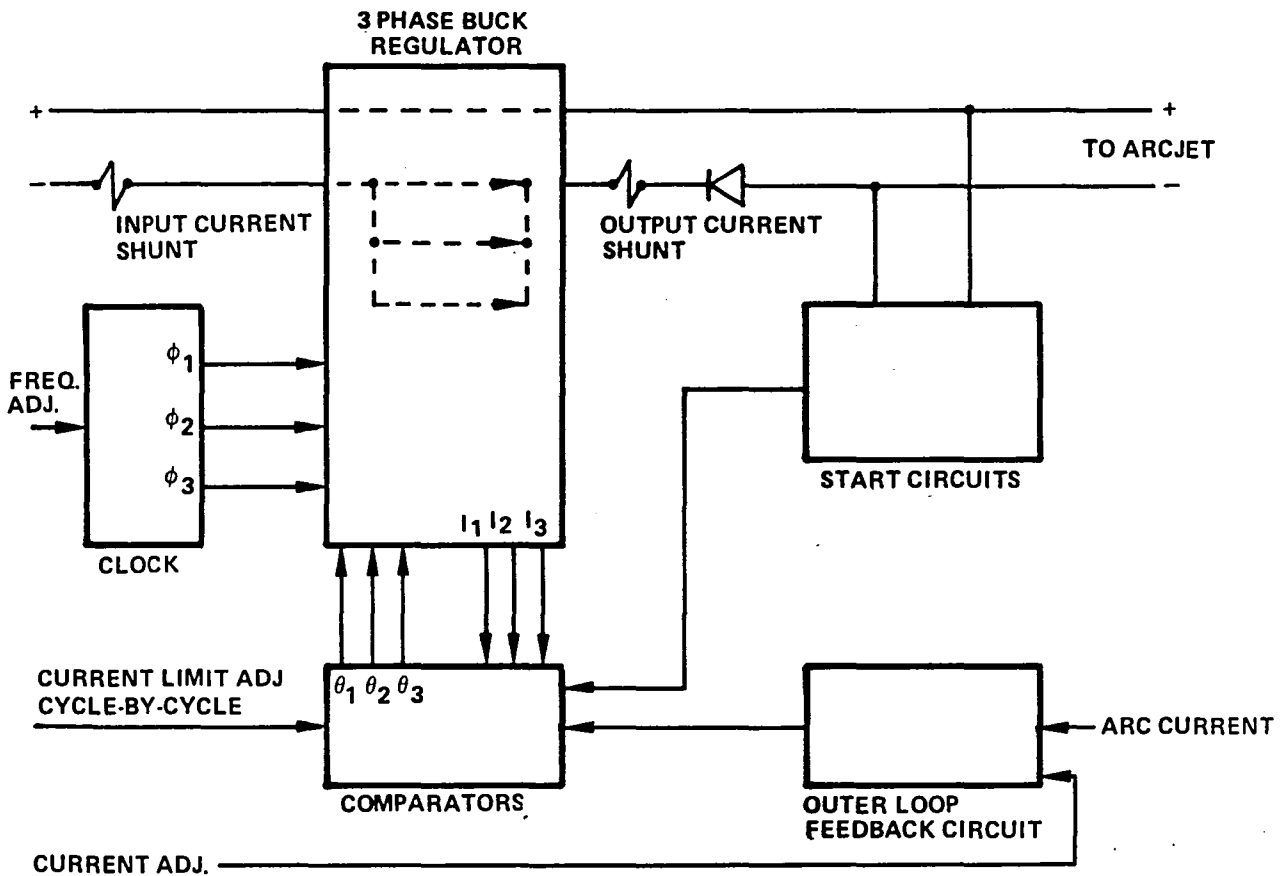
- 2.1 Operate in current and power control modes (voltage control optional)
- 2.2 Vary starting voltage pulse peak, duration, ramp-up time
- 2.3 Vary steady state I, V, or power while operating

3. Input: Use Sorensen DCA 150-70 supply. Ideally, the Sorensen voltage would be set to 28 V to simulate the spacecraft bus power. However, if significant cost and schedule savings will result from using higher supply voltages, this value will be relaxed.

4. Stability: Less than 0.5% variation in V, I after 8 hours.

5. Weight & Volume: There are no restrictions on weight and volume. However, this work is leading to flight hardware development. Preliminary laboratory PCU designs should be compatible with eventual weight and volume reduction.

PCU Block Diagram



The first block is made up of 3 buck regulators in parallel. These are operated 120° out of phase from each other. This arrangement results in a reduced ripple in the composite current, although there is considerable ripple in each of the three legs.

The three phase clock provides the signals to turn on the MOSFET switches of each buck circuit. It consists of a variable timing pulse generator clocking a 3 output, 3 state machine.

The comparators determine when each of the buck regulator switches is turned off. The current in each branch increases until the voltage developed across a shunt in that branch exceeds a reference voltage.

The reference voltage used by the comparator circuit to turn off each buck regulator branch has three sources: the current limit potentiometer on the control panel, the output of the outer loop feedback circuit, and the comparator signal for the startup circuit. These are electronically evaluated so that the reference voltage used by the comparator is equal to the lowest of the three.

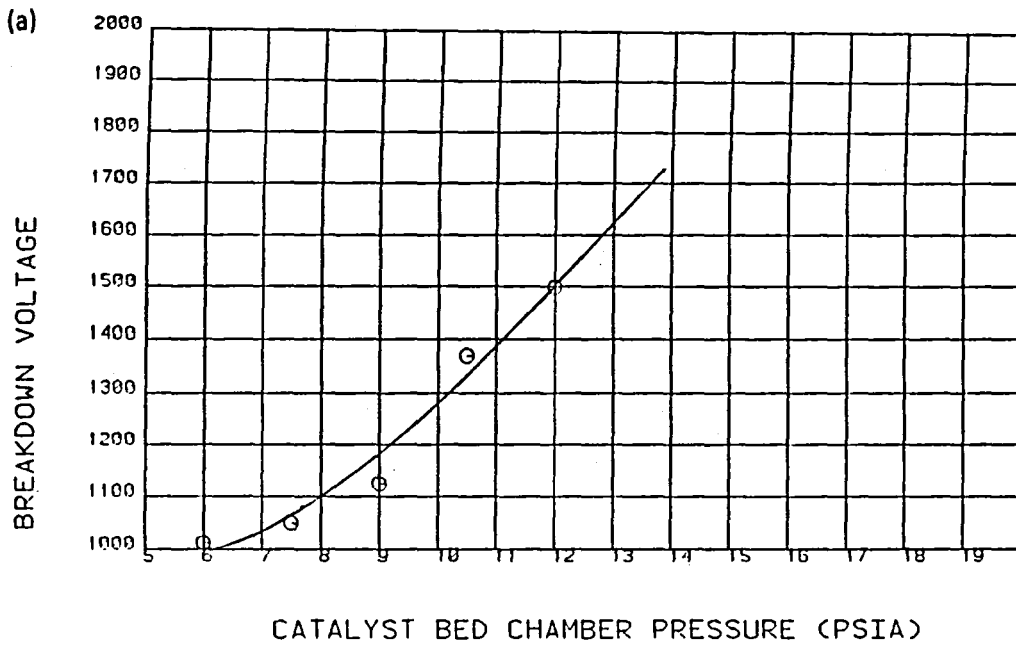
The startup circuit has two functions. First, it generates a high voltage startup pulse, and second, it ramps the current to its steady state value. A pulse forming network applies a low voltage pulse (0 - 150 volts peak) to the primary of a step-up transformer. The secondary of the transformer is connected in parallel with the PCU output, and provides 0-2500 V pulse. The high voltage pulse triggers a variable slope ramp generator.

3.5.3 Results/Discussion

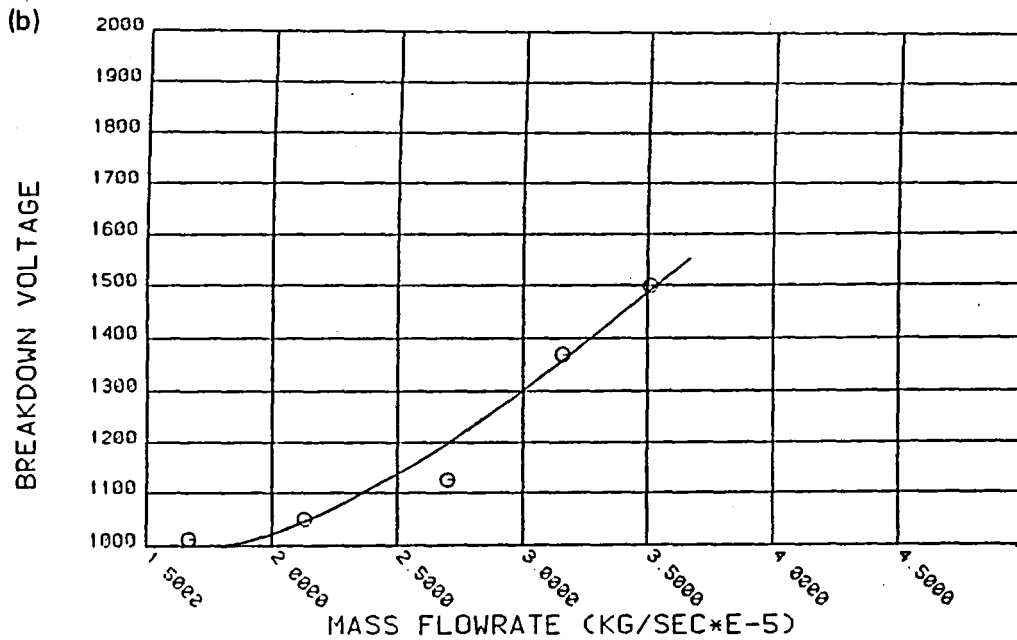
Startup tests were done to investigate three issues: the voltage required to breakdown at steady state flow rates; control of the current overshoot on startup; and the effect of the current ramp-up time on the startup phenomena.

A set of breakdown voltage data for a .076 cm diameter constrictor with a .038 cm gap is given in Figure 3-37. Rough calculations assuming a 1.5 kW, 450 sec arcjet and a typical satellite pressure blowdown curve give a range of flow rates over life from 5.5 to 4.0×10^{-5} kg/s. If the breakdown curves are typical of an eventual flight system, more than 2000 V will be needed for a breakdown at the highest steady state flowrate if the pressure

N₂H₄ ARCJET/PCU BREAKDOWN DATA



N₂H₄ ARCJET/PCU BREAKDOWN DATA



is not pulsed lower. The dependence of this voltage on flow field, gap, and cathode tip shape deserves further study. For a flight system, an upper value is needed that will always start the arcjet regardless of the flow rate or degree of cathode erosion. If this value is prohibitive from a system standpoint, an alternative method, such as a pressure pulse, may be needed.

Oscilloscope traces were taken for a large number of starts. Figure 3-38 gives an example. Voltage is the top trace, and is measured from the top down (375 V/div). Current is the lower trace, with the zero three divisions up (7.5 A/Div). The arcjet was hot, which lowered the breakdown voltage to 750 V. The current rises in 10 microseconds to almost 30 A. Then as the clock starts to cycle the three phases, it steps down to about 7 A. The subsequent current increase is determined by the ramp-up rate set by the PCU. The steady state level eventually reaches 17 A.

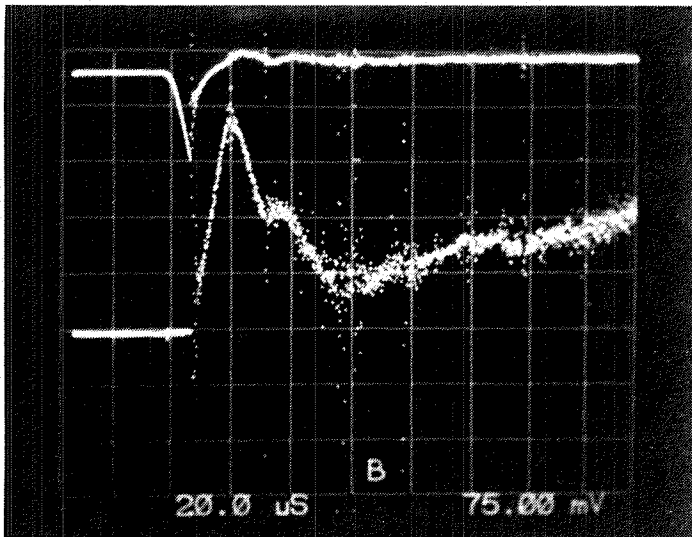
No startup erosion was visually evident under these conditions. The short duration of the spike limits the total energy transferred to the initial arc attachment point. Nevertheless, the design goal is to not allow the current to rise above the steady state set point during startup.

SPI was consulted and it was concluded that the spike is the result of the initial wait states of the three switches. All three are initially closed and conducting. As the maximum current limit is sensed in each phase, they start to open. The initial spike is the sum of the three phases. This was changed in a subsequent modification.

A second over-current phenomena occurs in the first 5 msec. Figure 3-39 shows the current traces for three ramp-up rates. In each, there is a 3 msec surge of about 5 A above the steady state value. This is of greater concern for erosion than the initial spike because of the longer duration. It is thought that this is due to the feedback circuit's response to the large current level change at startup.

Figure 3-39 also shows the traces produced by the current ramp-up feature. In 3-39 (a), the ramp-up rate is at a maximum. The current ramps continuously up to the surge value. In 3-39 (b) and (c), the ramp time was increased. The current level ramps up, but then levels off at between 7 and 10 amps. It then takes a step jump to the surge value. The step was not anticipated and not well understood. Ideally, a smooth transition will occur between the initial and the steady state current levels.

PCU STARTUP TRACE



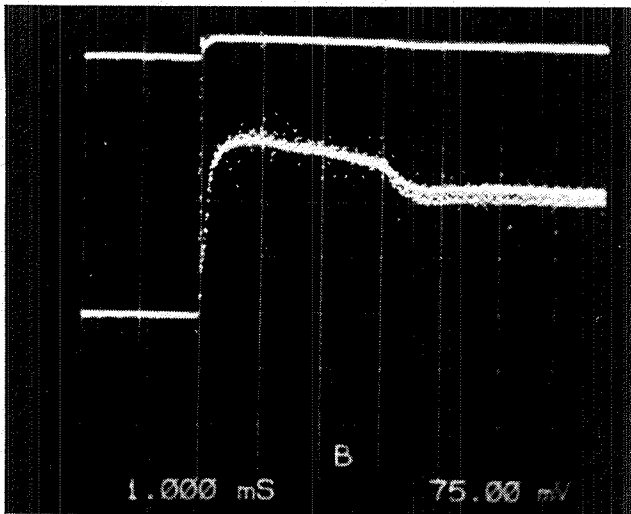
UPPER TRACE: VOLTAGE, 0 AT TOP,
375 V/DIV.

LOWER TRACE: CURRENT, 0 AS SHOWN,
7.5 A/DIV.

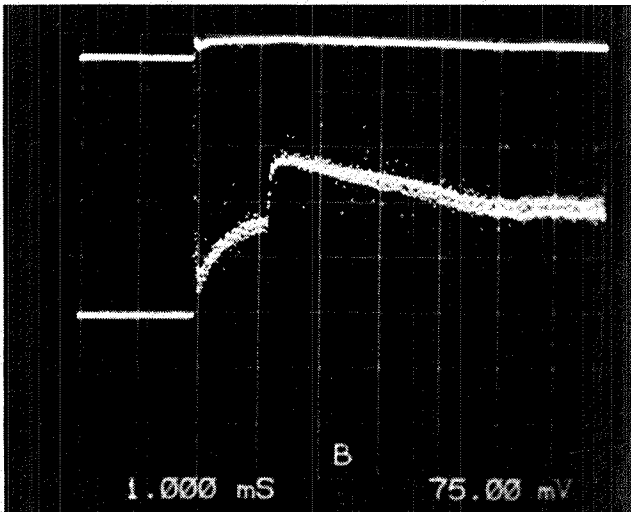
TIME SCALE: 20 MICROSEC/DIV.

BREAKDOWN VOLTAGE: 750 V (ENGINE HOT)

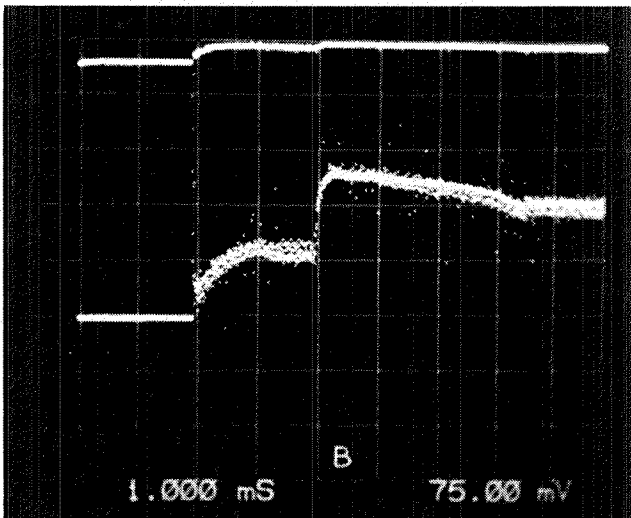
PCU STARTUP RAMP BEHAVIOR



(a) VOLTAGE, 375 V/DIV., 0 AT TOP
CURRENT, 7.5 A/DIV., 0 AS SHOWN.
DI/DT SET AT MAX. STEADY STATE
I LIMIT IS 15 A.



(b) SAME SCALE AS (a), BUT WITH
LONGER RAMP TIME.



(c) SAME SCALE AS (b), BUT WITH
LONGER RAMP TIME.

Startup tests produced few or no sparks, and no visible signs of erosion. However, the long term effects of hundreds of such starts is not known. Elimination of current overshoot is an obvious safeguard. It is not yet clear if current rise time is an important factor to startup erosion.

Steady state stability of the original PCU design was good. It was run over a range of current levels from 7 to 20 A. Figure 3-40 shows steady state voltage and current traces for three switching frequency settings. Theoretically, if the arc voltage is two-thirds the input voltage, the superposition of the three phases should result in identically zero ripple. In practice, subperiodic waveforms are produced by the interactions of the three phases.

After these initial tests, the PCU was sent back to SPI for modifications to improve the ripple characteristics, and to make the startup ramp smoother and without current overshoot. These changes are listed below:

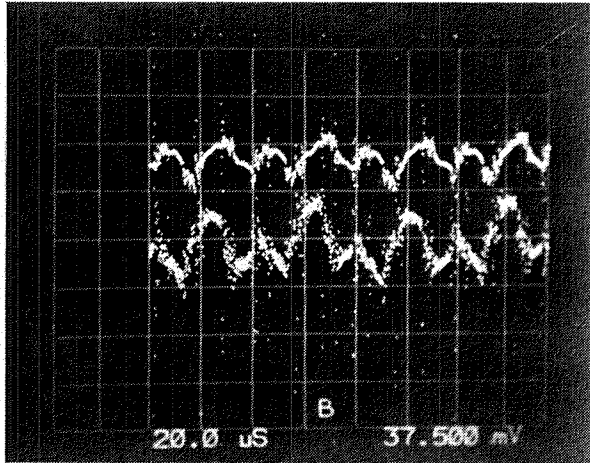
1. Add a ramp generator to the comparator reference to correct instabilities above a 50% duty cycle and to eliminate the sub-periodic current waveform. This also requires that the switching frequency be fixed at 50 kHz, instead of being variable.
2. Modify the outer loop feedback circuit. The PCU input current was originally the input to this circuit, but this ignored the commutating current when the buck regulator switches are turned off. Optical isolation of the sensed output current was necessary because all control circuitry is at the potential of the negative PCU input.

Two weeks were spent evaluating the new feedback setup. The tests were successful and provided insights into arc behavior for different geometries.

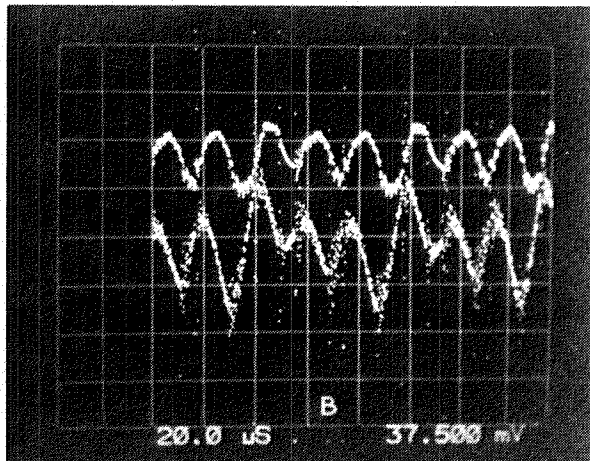
Oscilloscope traces are shown in Figures 3-41 and 3-42 for an arcjet with a "zero" length constrictor. Photographs (a) and (b) of Figure 3-41 show the composite current waveform produced at 6.7 A and 10.8 A, respectively. The complex form at 6.7 A results from the inductors going to zero current before each switch closes again. In (b), the duty cycle is such that the inductor current does not go through zero. Photograph (c) shows the superposition of each of the three phases. One phase is not tuned identically with the others, as evidenced by the increased ripple magnitude.

Photograph (a) of Figure 3-42 shows the composite current at 15.2 A. Photograph (b) shows a single phase. The peak to peak ripple of one phase is much higher than the composite signal.

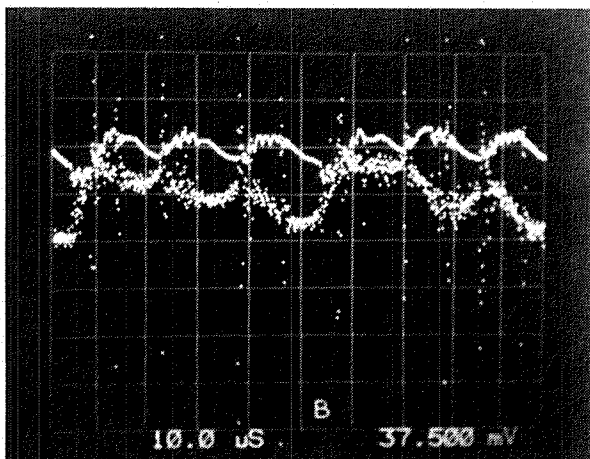
STEADY-STATE CURRENT/VOLTAGE TRACES



- (a) Voltage, 37.5 V/Div., 0 at top current, 3.75 A/Div., 0 at bottom, switching frequency 25 KHz.

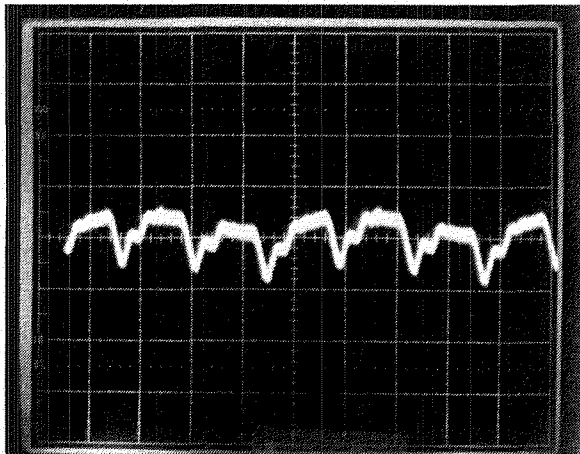


- (b) Voltage, 37.5 V/Div., 0 at top current, 3.75 A/Div., 0 at bottom, switching frequency 16 KHz.

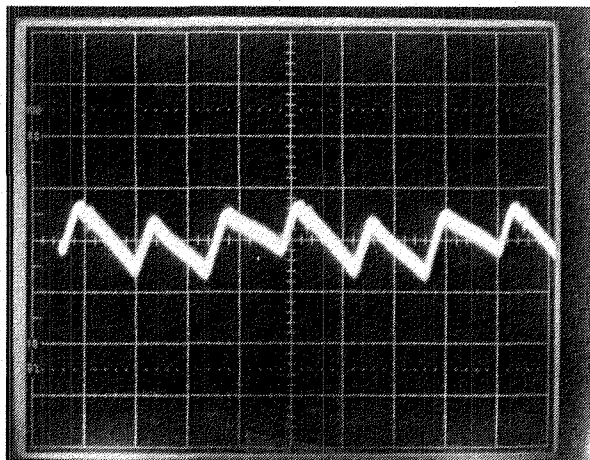


- (c) Voltage, 37.5 V/Div., 0 at top current, 3.75 A/Div., 0 at bottom, switching frequency 20 KHz.

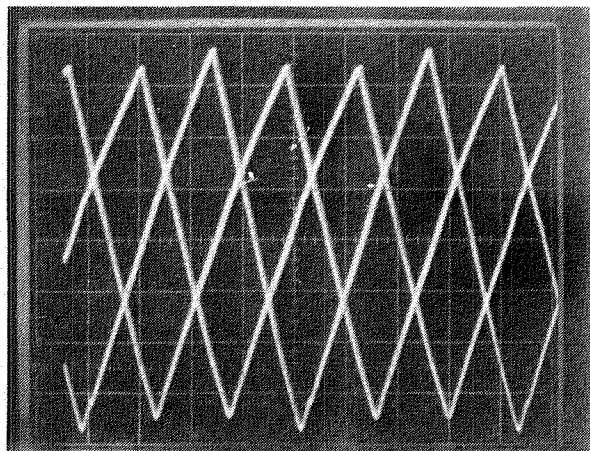
PCU CURRENT TRACES



- (a) Arcjet load
Composite current, 1 A/Div.
6.7 A, 95.5 V
5 microsec/Div.
150 V input

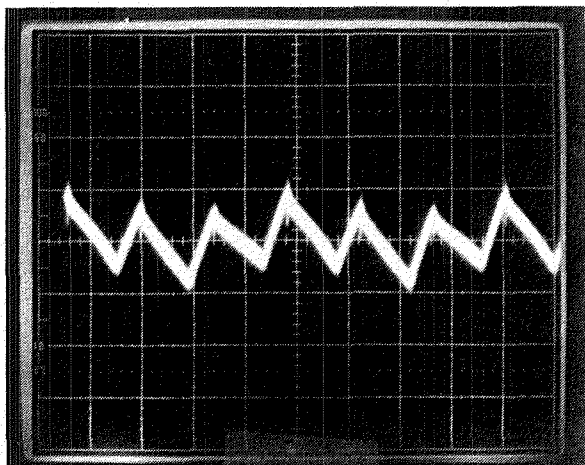


- (b) Arcjet load
Composite current, 1 A/Div.
10.8 A, 85.0 V
5 microsec/Div.
150 V input

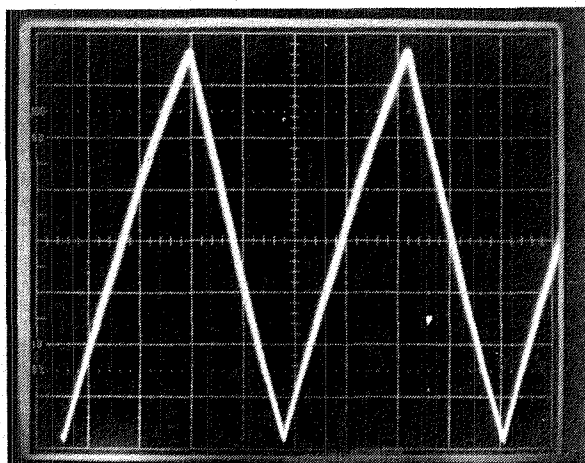


- (c) Arcjet load
Superposition of current through all 3
phases, 1 A/Div.
10.8 A, 85.0 V (same as No. 14)
150 V input

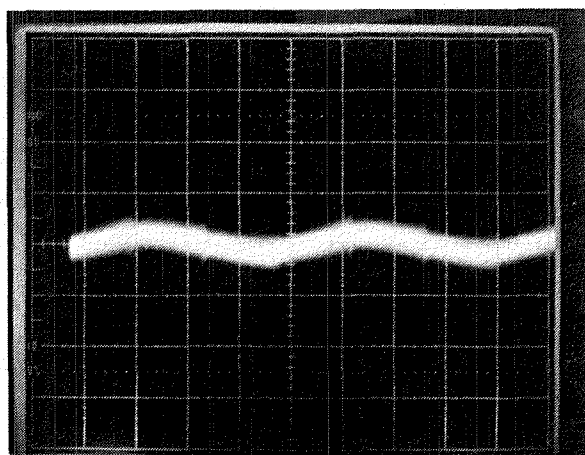
PCU CURRENT TRACES



(a) Arcjet load
Composite current, 1 A/Div.
15.2 A, 80.0 V
5 microsec/Div.
150 V input



(b) Arcjet load
Single phase current, 1 A/Div.
15.2 A, 80.0 V (same as No. 16)
5 microsec/Div.
150 V input



(c) Arcjet load
Composite current, 1 A/Div.
10.1 A, 87.0 V
5 microsec/Div.
135 V input

For typical arcjet operating conditions, the output to input voltage ratio was not an optimum to reduce ripple for 150V input. Photograph (c) of Figure 3-42 shows the result of lowering the input voltage to obtain a $2/3$ voltage ratio. At 10.1A, the peak-to-peak ripple is less than .75A.

With the "zero" length constrictor, the arcjet traces were very periodic and noise free. PCU testing done with a .076 cm length constrictor gave different results. There was a great deal more high frequency noise, and it was difficult to see if the signal was periodic. Clearly the dynamic characteristics of an arcjet can affect the PCU output. If the impedance of the inductors is high enough, the arcjet noise may be limited to the output lines. PCU operation is not affected, yet the output signal is masked by the line noise. If the output impedance of the inductors is too low at higher frequencies, the arcjet noise could conduct back onto the comparator current shunt and disturb the switching process.

3.5.4 PCU Development Conclusions

An optimized arcjet PCU was identified as being important to non-erosive starting techniques and to maintaining stable arc operation through experiences with a ballasted commercial supply. Close control of the initial current ramp-up is required. DC and dynamic stability criteria must be met. Such a unit will also be required for flight application of the arcjet to step up the spacecraft bus voltage to the arcjet voltage. Development work was initiated during Phase I.

A laboratory unit was designed, fabricated and tested. It was not a voltage boost design. Further refinement of the startup transient is needed to prevent current overshoot. The superposition of the 3 parallel buck regulator outputs resulted in a very low ripple, steady state output at the proper input to output voltage ratios. The PCU maintained the arc stability over a broad range of operating points.

It is important to consider the PCU and the arcjet as a system. Different arcjet configurations were shown to effect the output of the PCU. Work is planned during Phase II to characterize the dynamic arc load for both PCU stability and EMI design.

4.0 CONCLUSIONS

A number of conclusions were reached as a result of the Phase I low power arcjet development efforts. These are listed below:

1. Analysis

(i) Viscous losses dominate nozzle performance for expansion ratios > 50 . Nozzle optimization will prove difficult because of the low Reynold's numbers (< 1000) at these flow rates. Experimental verification is needed.

(ii) The arc/gas energy transfer involves chemical non-equilibrium processes because of the short gas residence time (< 1 microsec.) and chemical reaction rate constants. The performance implications of gas kinetics effects are currently unclear but will probably play an important role in eventually optimizing performance.

(iii) Vortex decay phenomena are difficult to analyze, but may be important to arc stability. The differences in arc stability between short and long constrictors may be evidence of this effect.

(iv) The energy transfer is predominantly in the localized arc region. The low flow rates and large passage areas indicate that improvements in efficiency through regenerative heating will require raising the arcjet body temperature. Gas temperatures already come close to those of the structure.

(v) There are several regions that deserve further analysis. The overall arc/gas/structure energy balance is critical to future efficiency improvements. This includes modelling the impact of plasma that is in thermal equilibrium but not in the chemical equilibrium. The energy transfer in the diffuse attachment region is also important. A second analysis task is to model the arc attachment at the cathode tip. This will be started during Phase II to support lifetime investigations. Analysis of the stabilizing vortex may prove untenable without experimental data. If this work is pursued, it may be necessary to scale up the arcjet to a size more compatible with flow diagnostics.

2. Design/Fabrication/Assembly

(i) The modular design developed for laboratory testing successfully provided flexibility for parametric tests. Close tolerances and strict control over documentation and assembly procedures was essential.

(ii) High temperature seals and fabrication techniques require further study for long life multiple start operation.

3. Operational/Lifetime Testing

(i) Arcjet startup and stability were successfully demonstrated for the first time with catalytically decomposed N_2H_4 .

(ii) Oxidation of the electrodes due to the H_2O content of standard hi-purity grade N_2H_4 propellant was not evident in the test time conducted (20 hours).

(iii) Startup erosion is a function of the electrode geometries, anode materials, flow field, and of the current transient produced by the PCU. Repeatable, non-erosive starting techniques were developed and demonstrated.

(iv) Long life anodes appear feasible. Understanding and minimizing steady state cathode erosion effects requires further effort. Cathode erosion may be a function of the current level, the tip thermal balance, the relative anode/cathode geometry, the flow field, and the material.

4. Performance Testing

(i) Specific impulse levels from 400 to 729 sec. were demonstrated with catalytically decomposed N_2H_4 . Higher levels appear feasible as no failure mechanisms were observed.

(ii) The constrictor geometry, vortex, and electrode gap do not strongly effect the performance. These do effect operational stability, however.

(iii) A single configuration can be operated over a broad power range. There is not a well-defined optimum operating point.

(iv) Frozen flow effects are the major determinants of arcjet efficiency. Anode thermal and nozzle viscous losses are smaller in magnitude.

(v) Increasing the current reduces the anode fall (thermal) losses. Increasing the flow rate reduces the thermal losses and the nozzle losses. Increasing the ratio of power to mass flow rate (P/\dot{m}) increases frozen flow losses. Advanced designs should be able to improve the efficiency above the present levels of 30 to 35%.

5. PCU Development

(i) Maintaining a stable arc requires meeting both DC and dynamic stability criteria.

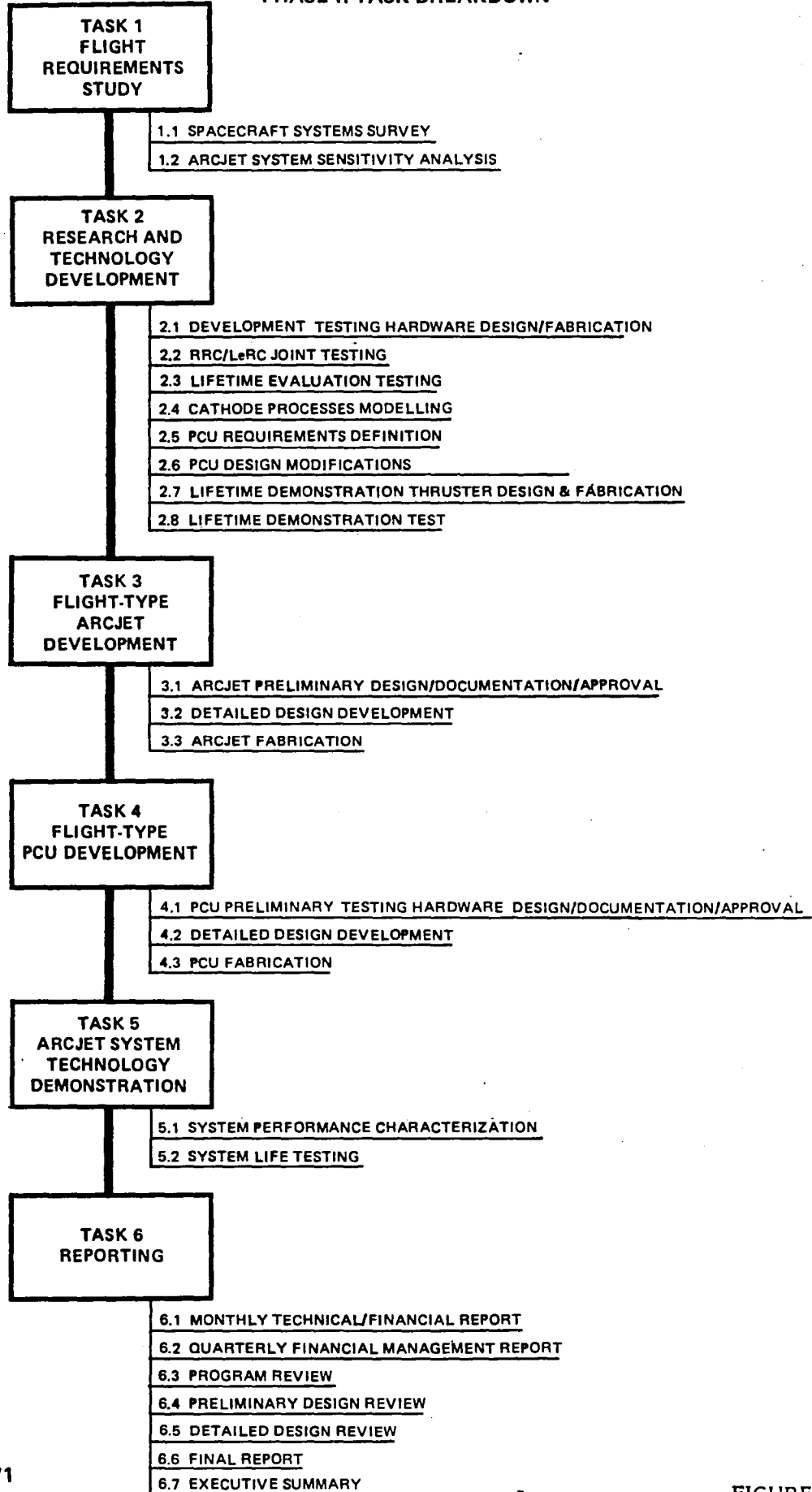
(ii) Essentially ripple free current output can be produced through the superposition of three parallel legs of a high switching frequency PWM supply. This could help reduce inductor sizes of an eventual flight unit.

(iii) Characterization of the arcjet load is needed over its operating envelope for future PCU design work. Its behavior is a function of the geometry and the propellant. This work will be performed during Phase II.

5.0 FUTURE WORK

Phase II of the Arcjet Thruster Research and Technology program is presently being carried out at Rocket Reserach Company. The primary emphasis of this phase is to develop the technology to demonstrate multi-hundred hour lifetimes in a duty cycle mode. Reducing the steady state erosion of the cathode is the key lifetime issue. Additional tasks include a survey of the possible constraints imposed by the spacecraft on the arcjet system, further PCU development work, detailed measurements of the dynamic arcjet impedance to support stability analyses, and testing of hardware provided by the NASA Lewis Research Center to show repeatable results at a separate facility. During the final part of the program, a flight type arcjet/PCU system will be developed and tested that will adhere to many of the design and operational requirements of a real flight system. This will serve to demonstrate the flight readiness of the N_2H_4 arcjet technology developed under this program. The Phase II task breakdown is given in Figure 5-1.

PHASE II TASK BREAKDOWN



REFERENCES

1. McCaughey, O. J., Geideman, W. A., Jr., Muller, K., "Research and Advanced Development of a 2 kW Arc-Jet Thruster," NASA CR-54035, 1963.
2. Cline, M. C., "VNAP2: A Computer Program For Computation of Two-Dimensional, Time-Dependent, Compressible, Turbulent Flow," Los Alamos, LA-8872, UC-32, August 1981.
3. Branch, M. C., et. al., "Review and Evaluation of Rate Data for Gas Phase Reactions of the N-H System," California University, 4D-755 855, 1971.
4. Cobine, J. D., "Gaseous Conductors," Dover Publications, 1958.
5. Sovey, J. S., Penko, P. F., Grisnik, S. P, and Whalen, M. V., "Vacuum Chamber Pressure Effects on Thrust Measurements of Low Reynold's Number Nozzles," NASA TM-86955, 1985.
6. Page, R. J., et. al., "Development of a Thermal Arc Engine," ASD-TDR-62-740. Plasmadyne Corporation, 1962.
7. Todd, J. P., "30 kW Arc-Jet Thruster Research," Final Technical Report No. APL-TDR-64-58, Giannini Scientific Corporations, 1964.
8. Unitrode Corporation, "Modelling, Analysis, and Compensation of the Current-Mode Converter," Application Note U-97.

APPENDIX A

VNAP2 Nozzle Analysis Plots

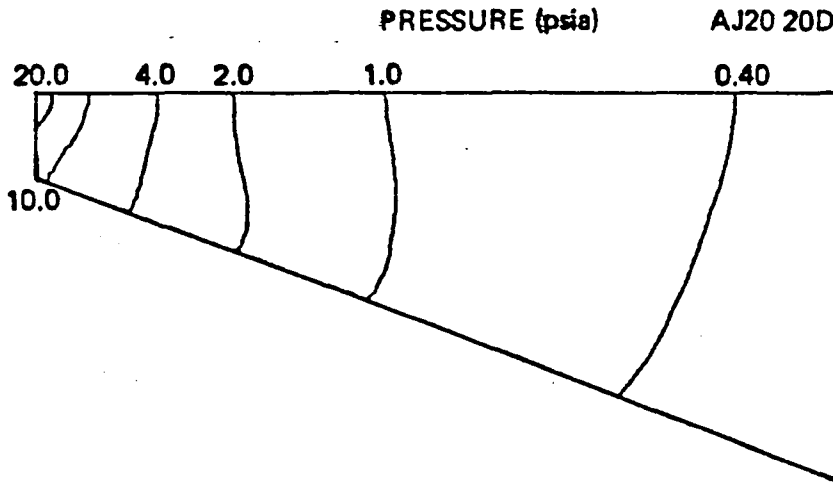
The following figures (A-1 to A-6) show pressure density, and temperature nozzle profiles calculated with VNAP2 for the six nozzle contours listed in Table A-1. Nozzle inlet conditions were calculated using ARCJET III, RRC's arc energy balance model. (See section 3.1.2, VNAP2 Nozzle Analysis.

Table A-1

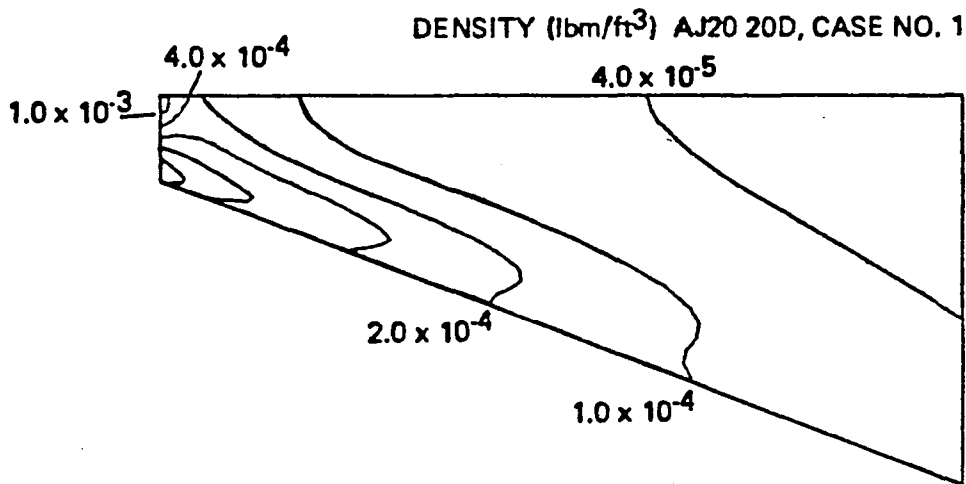
VNAP2 NOZZLE PROFILES

Number	Nozzle	Half Angle	Area Ratio	Figure
1	Conical	20°	20	A-1
2	Conical	20°	50	A-2
3	Conical	20°	100	A-3
4	Conical	10°	50	A-4
5	Conical	30°	50	A-5
6	Contour	--	50	A-6

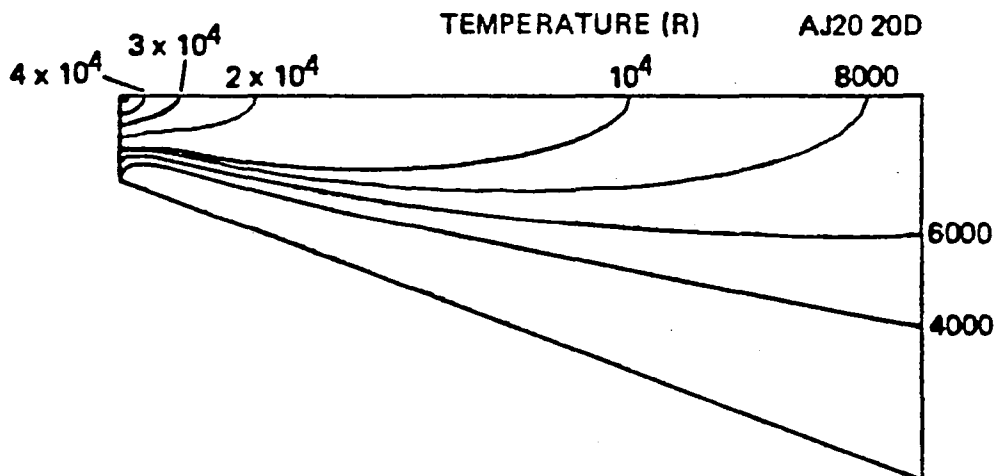
VNAP2 OUTPUT
 PRESSURE, DENSITY, AND TEMPERATURE PROFILE, CASE 1



N= 8

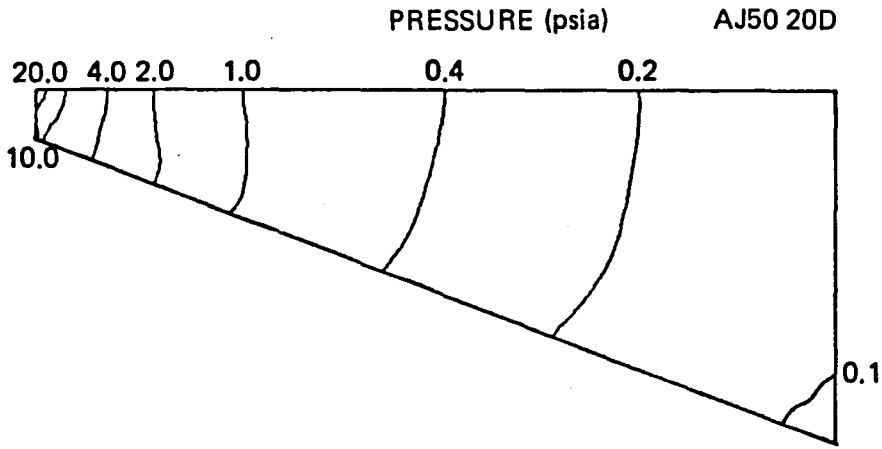


N= 8

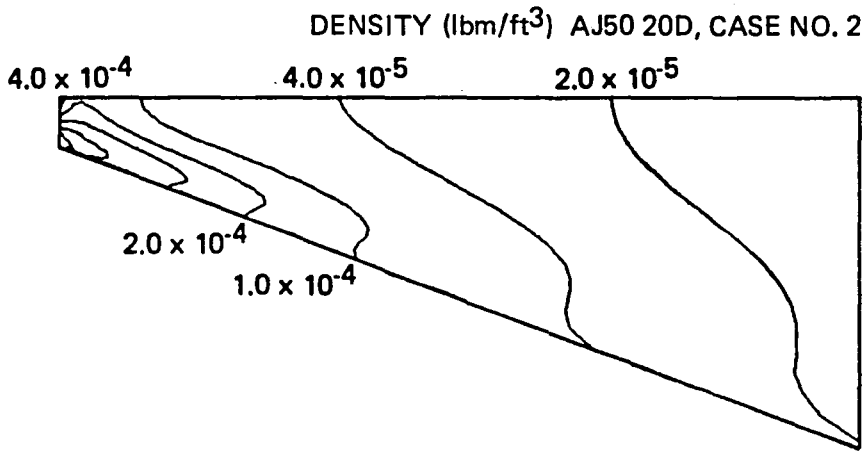


N= 8

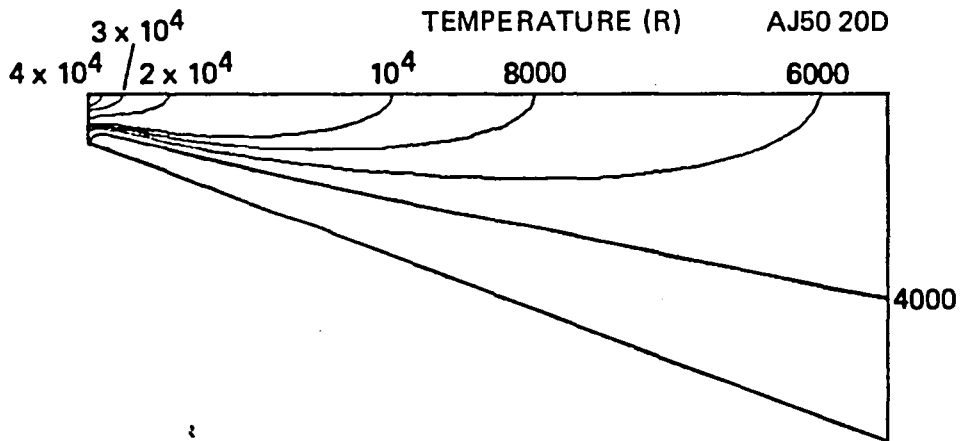
VNAP2 OUTPUT
 PRESSURE, DENSITY, AND TEMPERATURE PROFILE, CASE 2



N= 0

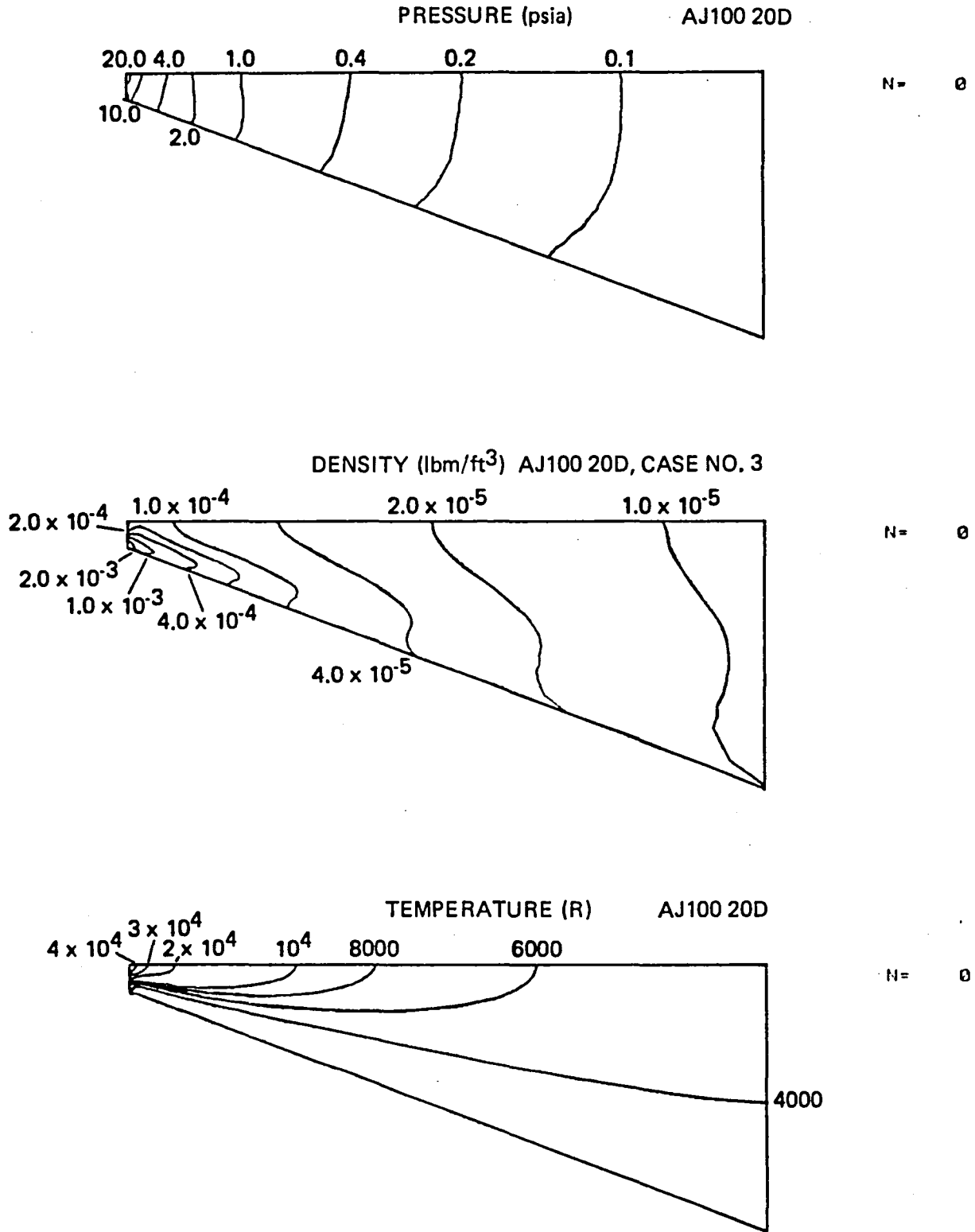


N= 0

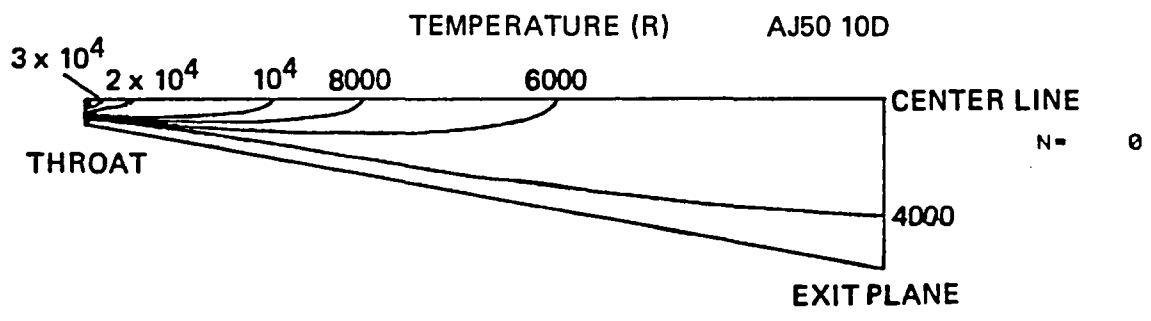
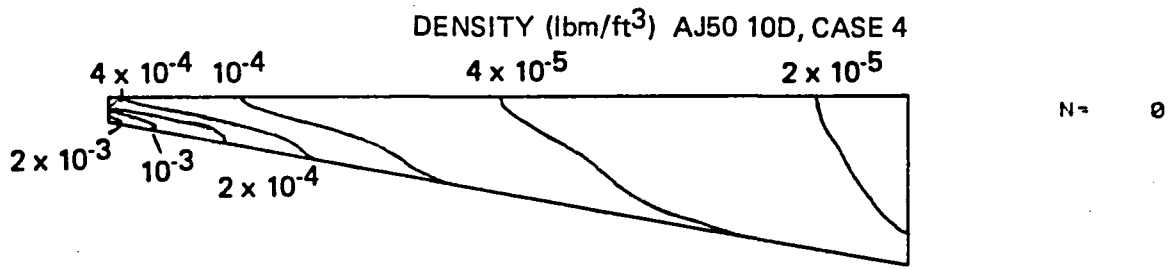
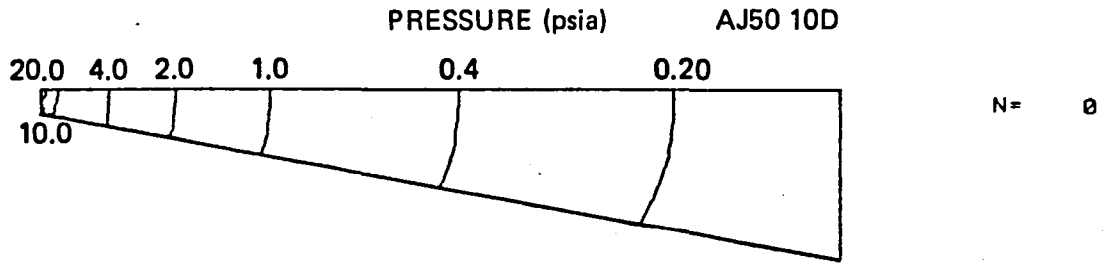


N= 0

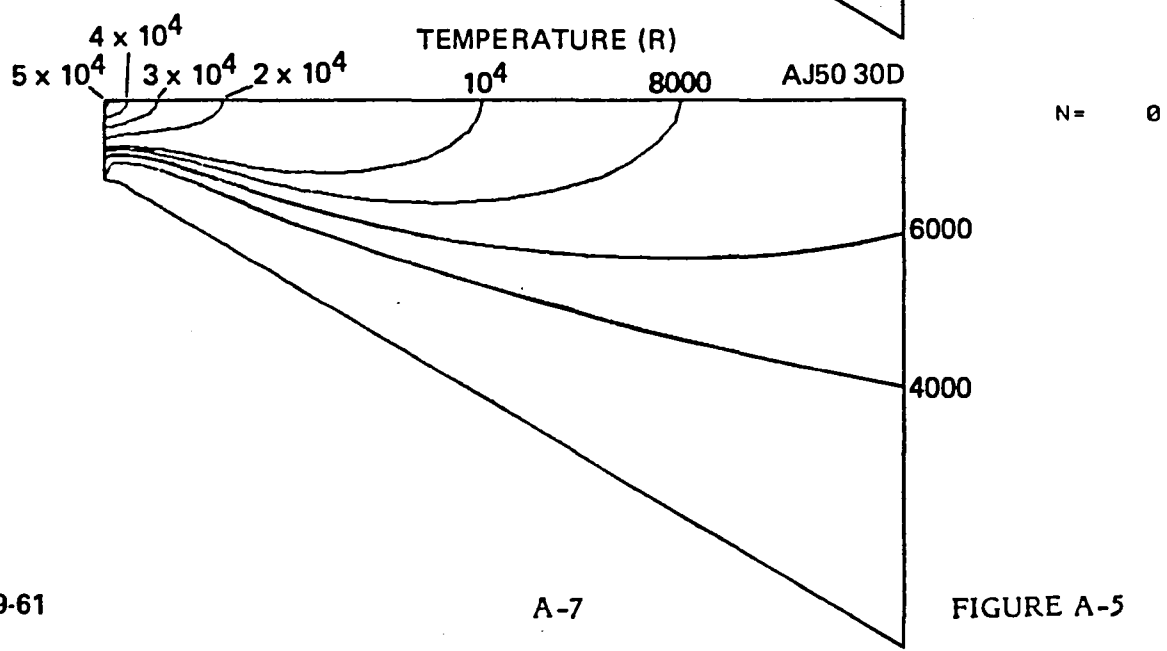
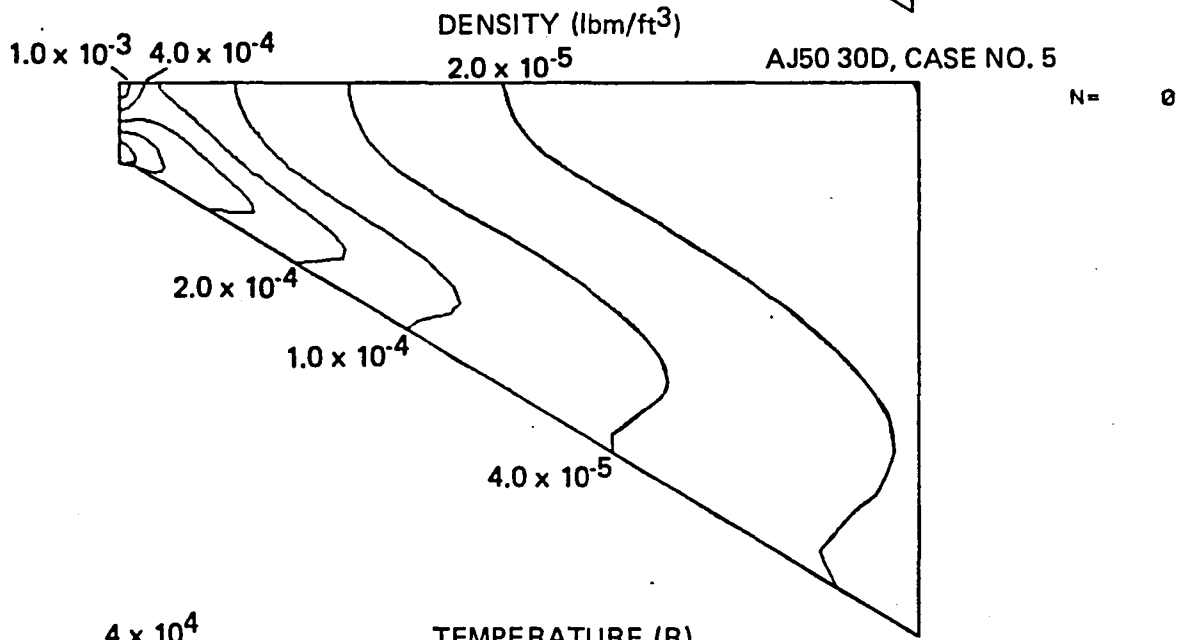
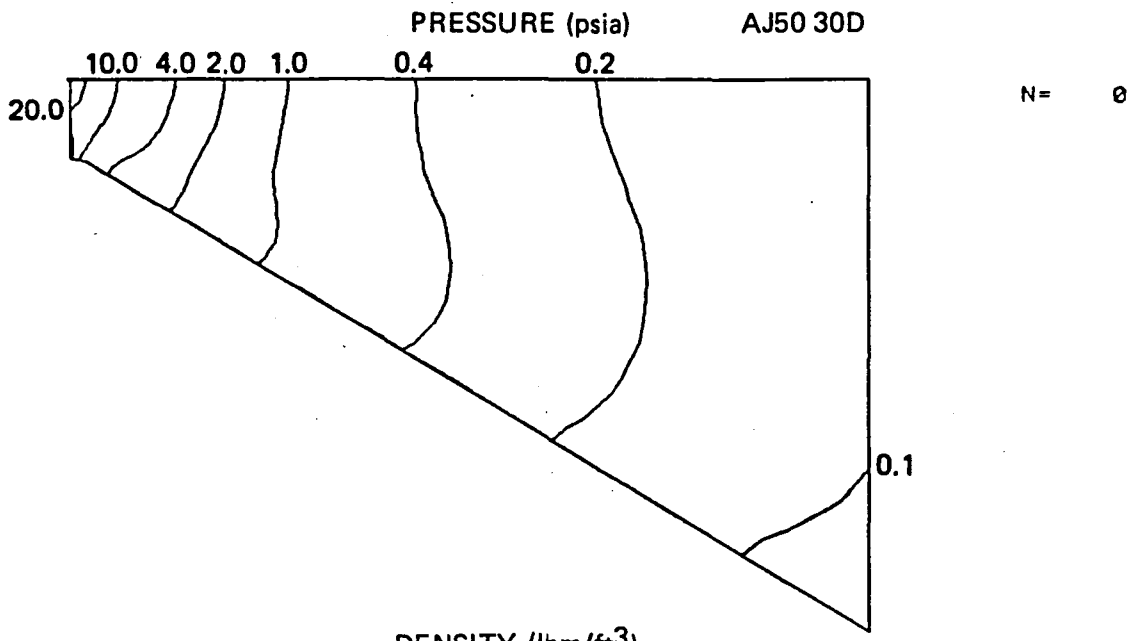
VNAP2 OUTPUT
 PRESSURE, DENSITY, AND TEMPERATURE PROFILE, CASE 3



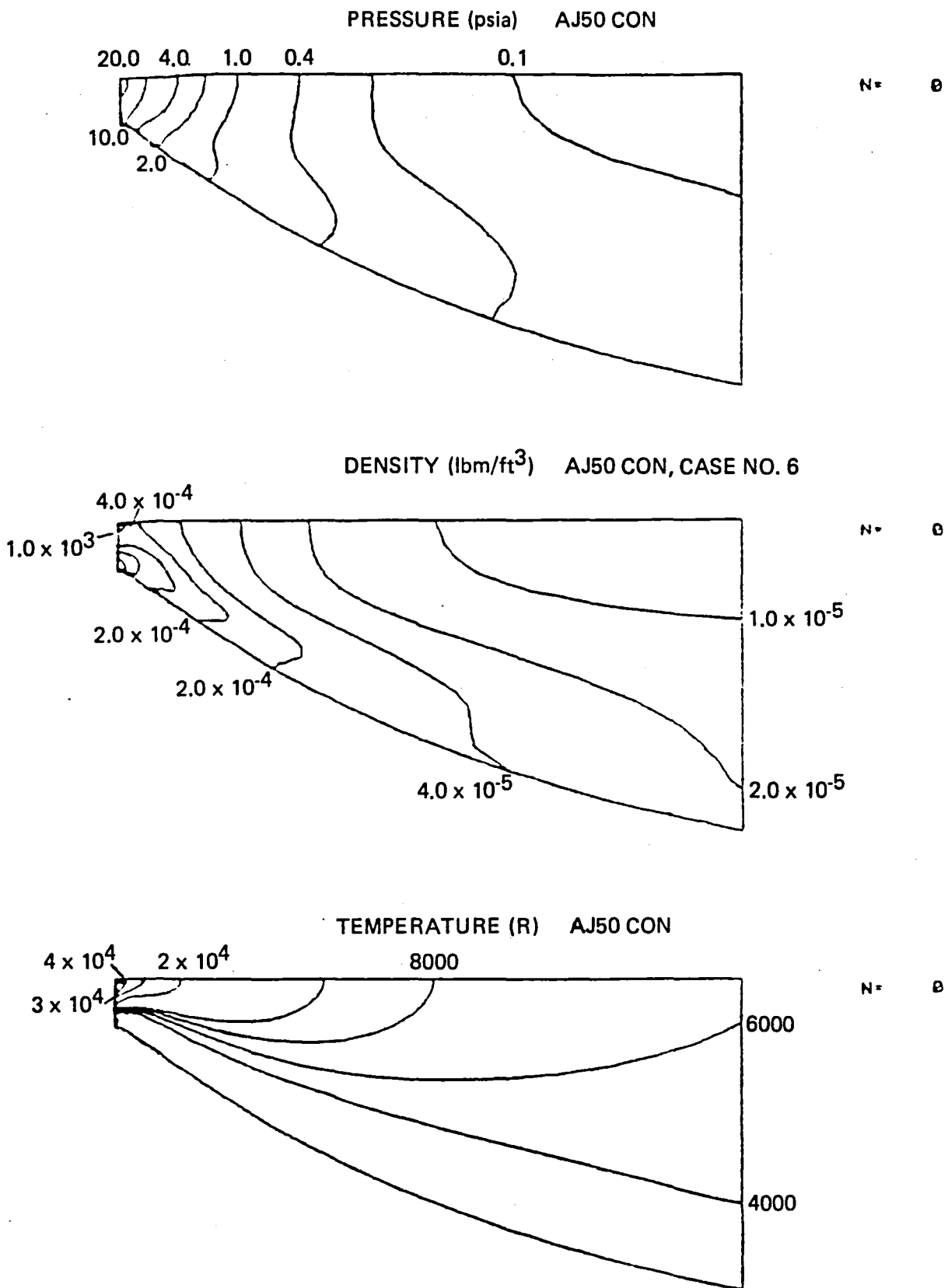
VNAP2 OUTPUT
 PRESSURE, DENSITY, AND TEMPERATURE PROFILE, CASE 4



VNAP2 OUTPUT
 PRESSURE, DENSITY, AND TEMPERATURE PROFILE, CASE 5



VNAP2 OUTPUT
 PRESSURE, DENSITY, AND TEMPERATURE PROFILE, CASE 6



APPENDIX B

Summary of Vortex Analysis Techniques

A review was conducted of vortex analysis techniques to assess the feasibility of modelling the arcjet vortex flow field. The following summarizes the review results. It was determined that such a modelling effort would be beyond the scope of this program, but could be the subject of future efforts.

Vortex Structure

Typically a vortex flow is represented by a Rankine vortex consisting of an inner viscous core surrounded by an inviscid potential flow, where in its simplest form:

$$\begin{aligned} \text{axial velocity, } (\omega r_c) &= \text{constant} \\ \text{tangential velocity, } v(r) &= \omega r, \quad 0 < r < r_c \\ &= \omega r_c^2 / r, \quad r_c < r < R \end{aligned}$$

With:

$$\begin{aligned} r_c &= \text{core radius,} \\ R &= \text{tube radius,} \end{aligned}$$

and ω = angular velocity of core rotating as solid body.

Leibovich¹ suggests a more complex velocity profile developed from experimental data curve fits,

$$w(r) = W_1 + W_2 \exp(-\alpha r^2)$$

$$v(r) = \lambda (1 - \exp(-\alpha r^2))$$

where:

W_1 , W_2 , λ , and α are curve fitting constants.

Various other authors have proposed analytic solutions to establish axial and tangential velocity profiles more generally without resorting to a numerical solution for the complete equations of motion. One method proposed by Hsu² considers compressibility effects and calculates the vortex core flow radius based on the ratio of maximum swirl energy to total energy,

$$\alpha(r_c) = (\gamma - 1)/2 \cdot \frac{1}{2} \omega r_c^2 / a_o R,$$

where:

$\alpha(r_c)$ = swirl parameter at core radius r_c ,
 γ = specific heat ratio,
and a_o = stagnation speed of sound.

It is not clear if this method is capable of predicting the possibility of reversed flow at high swirl intensities. An alternate, more complex method using integral momentum equations was outlined by Maeger.³ This method does distinguish between mass flow dominated and swirl dominated vortex cores with reversed flow, but was limited to an incompressible flow assumption and assumes a constant axial velocity outside the core.

Either of these two techniques could be used to estimate velocity profiles at the entrance to the constrictor with suitable modifications to account for the influence of the cathode on the flow field. Neither of these techniques will permit coupling to energy equations and will not be useful for studying the interactions of the arc with vortex flow.

Vortex Stability

Two mechanisms can disrupt or alter vortex flow fields:

1. Viscous dissipation
2. Vortex breakdown

Viscous dissipation is simply the slowing and smoothing of tangential velocity profiles due to internal and boundary layer drag forces caused by the fluid viscosity. Vortex breakdown is more complex and involves the formation of internal stagnation points and regions of reversed axial flow.¹ Vortex instability has been described based on wave

propagation characteristic of the flow fields and is analogous to shock waves and hydraulic jump phenomena.

For an optimized design a balance must be found such that sufficient swirl is given to the propellant to stabilize the arc column, but less than the critical value which will result in a vortex breakdown within the constrictor. The degree of viscous dissipation and associated reduction in arc stabilizing radial pressure gradients is important for defining maximum constrictor length to diameter ratios. It can be assumed that operation with local stagnation points or reversed flow regions will destabilize the arc column due to sudden flow redirection and turbulence generation. As a result it is also desirable to have a method for predicting onset of vortex breakdown.

Viscous dissipation of a vortex flow must be modeled numerically. The methodology proposed by Shaeffer⁴ is appropriate.

The simplification of the Navier-Stokes equations employed by Shaeffer required a quasicylindrical assumption which implies a weak swirl flow where reverse flow does not occur. Swirl was characterized by the axial flow ratio of swirl to axial momentum.

$$S = \frac{\int R r V_{\theta} V_Z dA}{\int_0^R \rho V_Z^2 dA}$$

where:

S = nondimensional swirl parameter,

ρ = local density,

and V_{θ}, V_Z = tangential and axial velocity components.

An alternative approach for avoiding vortex breakdown can be derived from experimental data relating the axial position of observed breakdowns in vortex tubes vs. Reynold's number and a dimensionless swirl parameter,¹

$$\Omega = \pi \Gamma D/4Q$$

where:

- Ω = swirl parameter,
- D = wall diameter,
- Γ = potential flow circulation,
- and Q = volumetric flowrate.

For a typical length to diameter ratio of 2 to 1 used in the present design at $Re = 3000$, a maximum swirl parameter of $\Omega = 1.54$ is indicated.

It should be noted that reversed flows can occur without vortex breakdown as demonstrated by So.⁵ This is principally a nozzle effect and may explain the reversed flow region noticed in the nozzle plume during cold gas flow through higher power arcjets at RRC.

Arc-Vortex Interaction

Interaction of the arc column and the vortex flow field must be modeled numerically to consider the individual and combined affects of swirl, turbulence, pressure gradients, heat addition and electric fields. The method outlined by Shaeffer⁴ is a reasonable approach. However, the momentum equations used in the swirl arc model have been simplified from the Navier-Stokes equations by assuming constant density. Compressibility effects have been limited to the continuity equation. The quasicylindrical assumption made limits applicability to constant or slowly changing area ducts. Body forces in the momentum equations have also been neglected.

Arc column stability is dependent on both the strength of radial pressure gradients generated by the swirl flow and on the electrical insulation of cooler gases flowing along the constrictor wall. Radial pressure gradients limit distortion or kinking of the arc column,

$$\text{radial pressure gradient, } \frac{\delta P}{\delta r} = \rho V_{\theta}^2 / r$$

$$\text{magnetic kinking force, } F = \mu_0 I^2 / 8 \pi \frac{2}{r_a} \frac{2}{r_k}$$

where:

μ_o = permeability of free space,
 r_k = kink radius,
 I = current,
and r_a = arc radius.

Stability occurs when the pressure gradient exceeds the arc kinking force at a given radius.

Both of the arc stabilizing influences degrade with axial distance down the constrictor due to heat addition. The insulation value of the outer gas layers is reduced as the bulk gas temperature rises and the swirl flow field decays as the viscosity of the gas is increased. An optimum constrictor length to diameter ratio will be short enough so that at worst case the arc kink radius will be equal to the constrictor radius just at the transition of the nozzle.

At some maximum swirl value the length to diameter ratio can no longer be increased without causing vortex breakdown. However, Escudier⁶ noted in his work on swirl combustors that heat addition significantly influences the swirl flow field and conclusions based on cold flow analyses may be misleading (i.e., stagnation and reversed flow may not occur or may be entirely different than anticipated).

APPENDIX B REFERENCES

1. Leibovich, S., "Vortex Stability and Breakdown: Survey and Extension", AIAA Journal, September 1984.
2. Hsu, C. T., "Inviscid Swirling Flows Through a Choked Nozzle", AIAA Journal, September 1983.
3. Maeger, A., "Incompressible Viscous Swirling Flow Through a Nozzle", AIAA Journal, April 1971.
4. Schaeffer, J. F., "Swirl Arc: A Model for Swirling, Turbulent, Radiative Arc Heater Flowfields", AIAA Journal, October 1978.
5. So, K. L., "Vortex Phenomena in a Conical Diffuser", AIAA Journal, June 1967.
6. Escudier, M. P., "Recirculation in Swirling Flow: A Manifestation of Vortex Breakdown", AIAA Journal, January 1985.

APPENDIX C

N_2H_4 Arcjet Performance Data

This appendix provides plots of the performance data taken on several N_2H_4 arcjet configurations as described in section 3.4, Performance Testing. Table C-1 lists the geometries tested, and Table C-2 gives an index to the plots.

Table C-1
PERFORMANCE TEST CONFIGURATIONS

<u>Test #</u>	<u>Constrictor Length (cm)</u>	<u>Constrictor Diameter (cm)</u>	<u>Gap Setting (cm)</u>	<u>Injector Port Area (cm²)</u>
9.2	.076	.076	.038	2.68
10.2	.000	.076	.038	2.03
12.1	.000	.076	.038	1.30
14.2	.051	.058	.025	2.68
16.2	.152	.076	.046	2.03
17.1	.076	.076	.046	1.30
18.4	.076	.076	.046	2.03

Nozzle half angle = 20^o, = 50

PERFORMANCE DATA FIGURE LIST

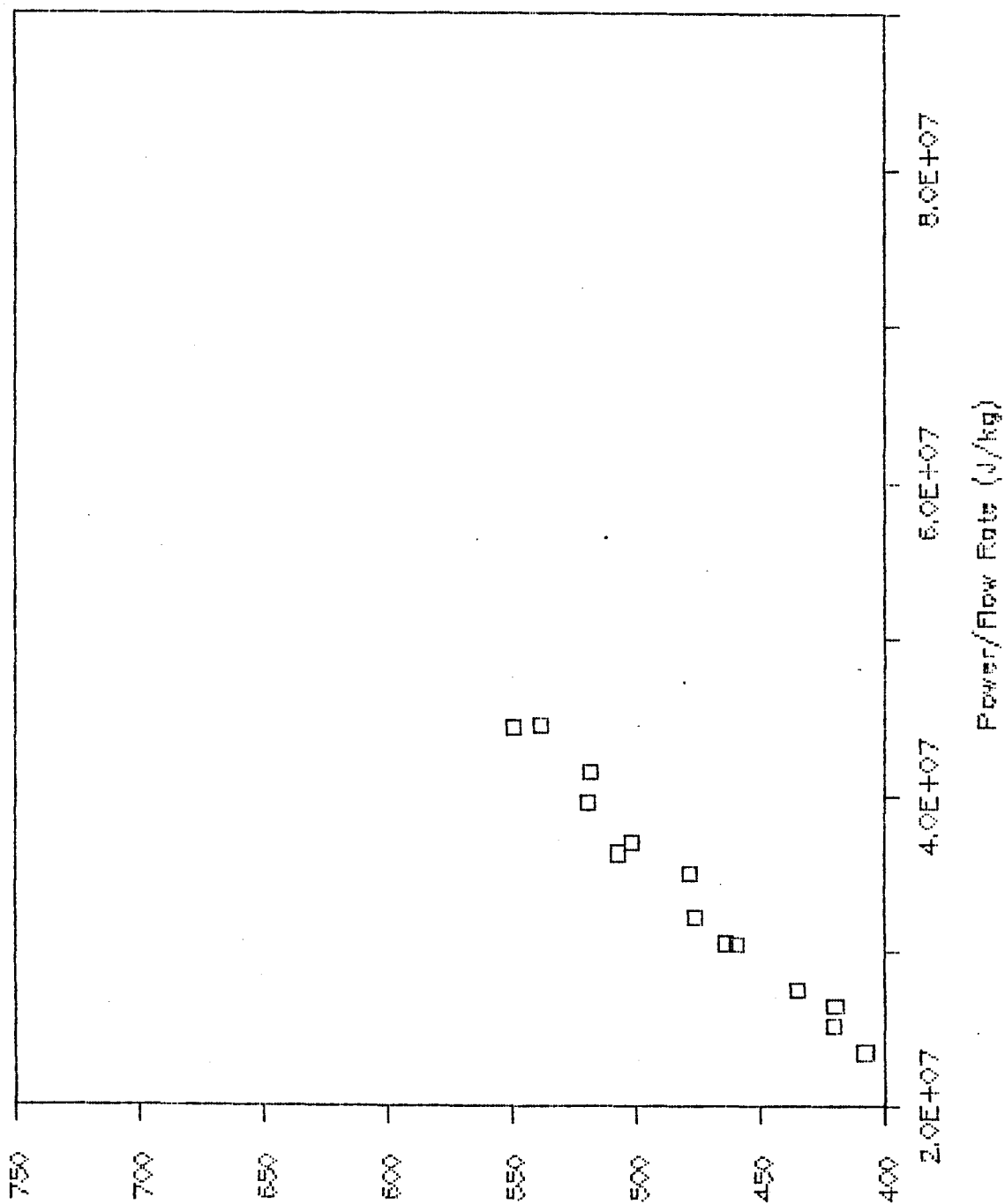
<u>#</u>	<u>Test</u>	<u>Description</u>
1	9.2	I_{sp} vs. P/\dot{m}
2	9.2	V vs. I
3	10.2	I_{sp} vs. P/\dot{m}
4	10.2	I_{sp} vs. P_c
5	10.2	I_{sp} vs. P_c
6	10.2	V vs. I
7	10.2	Th vs. P/\dot{m}
8	10.2	I_{sp} vs. Th/P
9	12.1	I_{sp} vs. P/\dot{m}
10	14.2	I_{sp} vs. P/\dot{m}
11	14.2	I_{sp} vs. P_c
12	14.2	V vs. I
13	14.2	Th vs. P/\dot{m}
14	14.2	Eff vs. P/\dot{m}
15	16.2	I_{sp} vs. P/\dot{m}
16	16.2	I_{sp} vs. P_c
17	16.2	V vs. I
18	17.1	I_{sp} vs. P/\dot{m}
19	17.1	I_{sp} vs. P_c
20	17.1	V vs. I
21	17.1	Th vs. P/\dot{m}
22	18.4	I_{sp} vs. P/\dot{m}

PERFORMANCE DATA FIGURE LIST (Continued)

<u>#</u>	<u>Test</u>	<u>Description</u>
23	18.4	I_{sp} vs. P_c
24	18.4	I_{sp} vs. Th/P
25	18.4	Eff vs. P/\dot{m}
26	18.4	Eff vs. P_c
27	18.4	V vs. I
28	18.4	Eff vs. V/I
29	18.4	Th vs. P/\dot{m}
30	9.2, 17.1, 18.4	V vs. I
31	14.2, 18.4	Eff vs. P/\dot{m}
32	9.2, 17.1, 18.4	I_{sp} vs. P/\dot{m}
33	10.2, 18.4, 16.2	V vs. I
34	14.2, 18.4	Th vs. P/\dot{m}

Specific Impulse vs. Power/Flow rate

Test 9.2



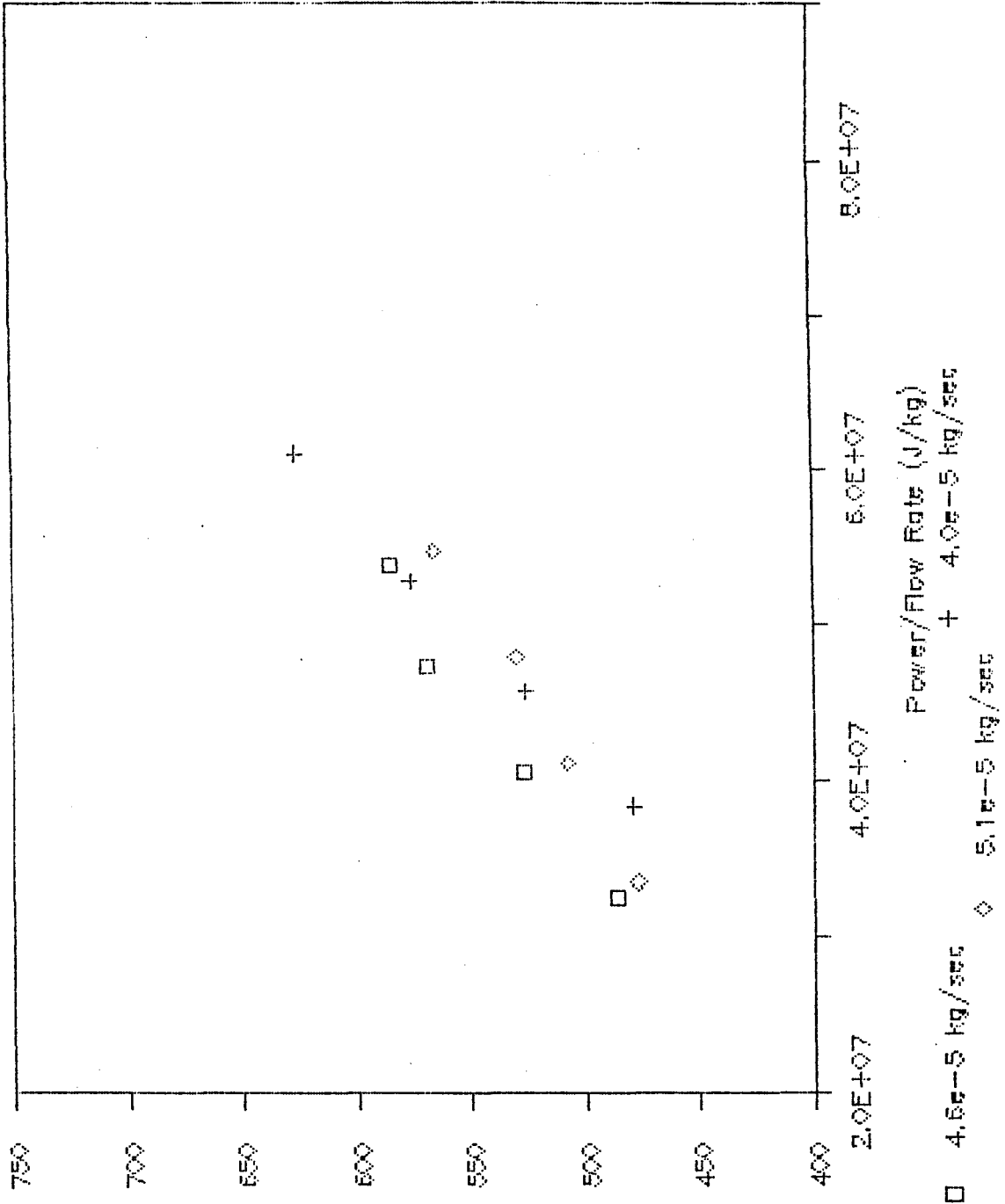
Specific Impulse (sec)

C-5

FIGURE C-1

Specific Impulse vs. Power/Flow Rate

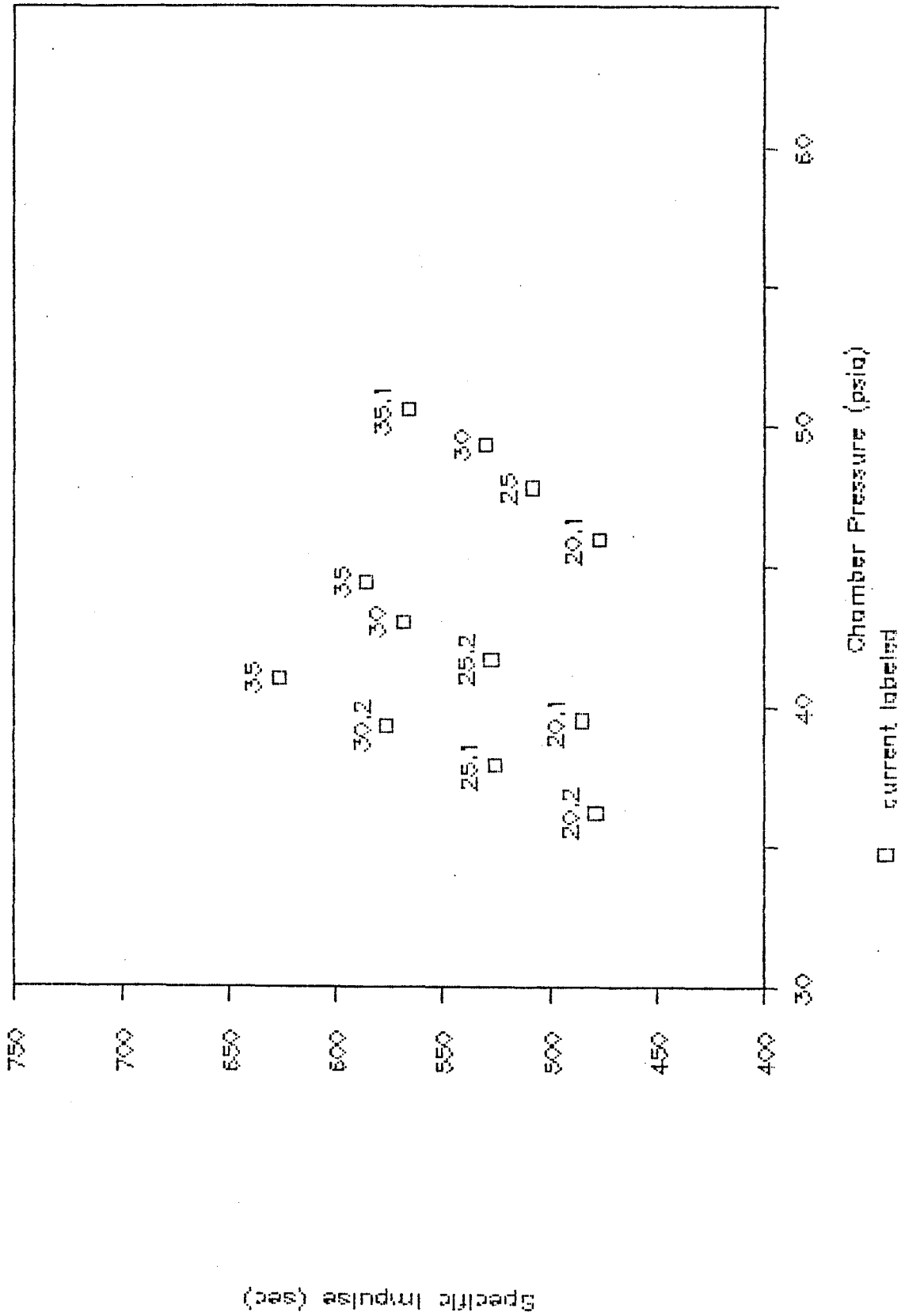
Test 10.2



Specific Impulse (sec)

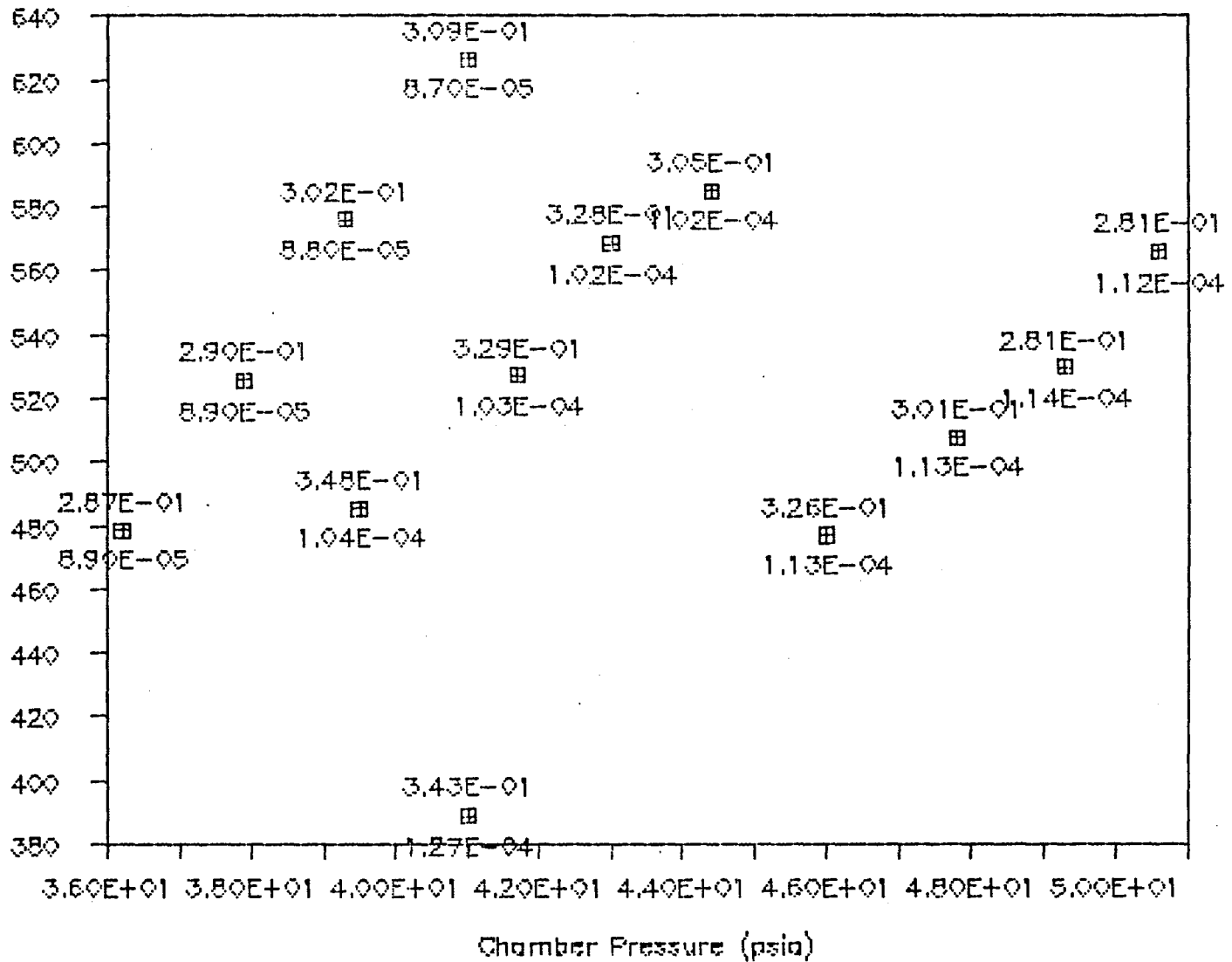
Specific Impulse vs. Chamber Pressure

Test 19.2



Isp vs. Pc

Test 10.2



- o Efficiency
- o Flow rate (lbm/s)

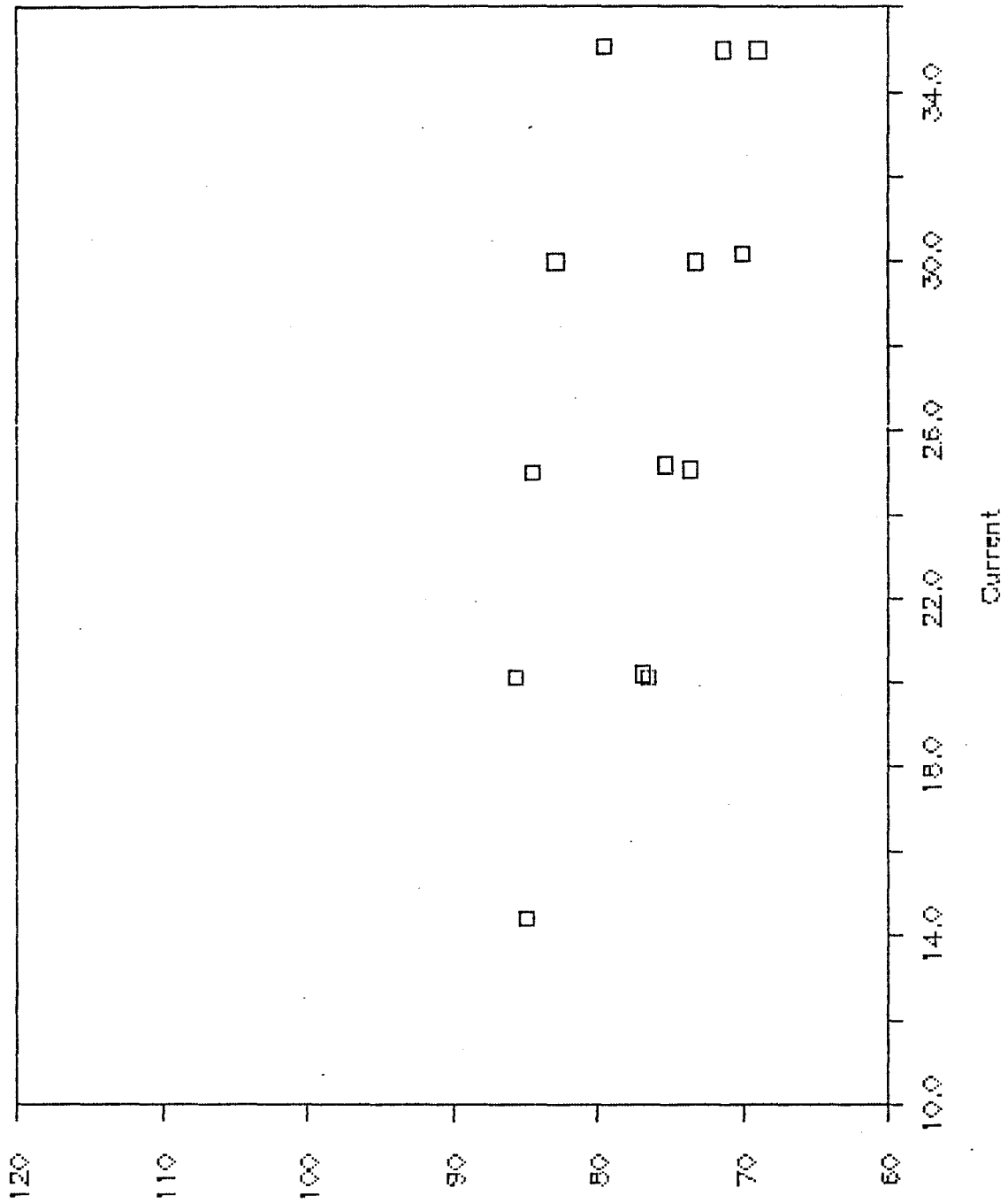
C-9

Specific Impulse

FIGURE C-5

Voltage vs. Current

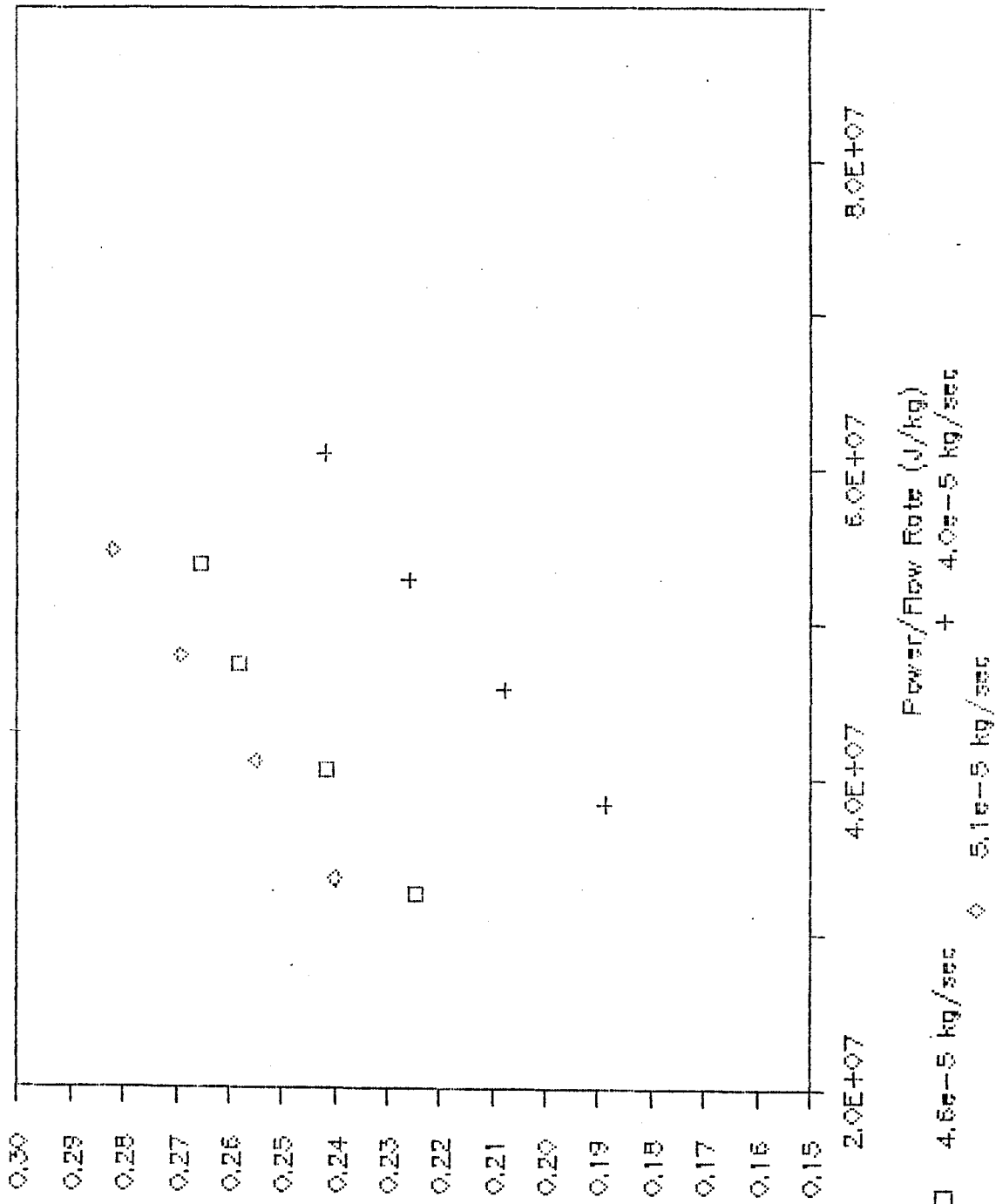
Test 10.2



Voltage

Thrust vs. Power/Flow Rate

Test 10.2

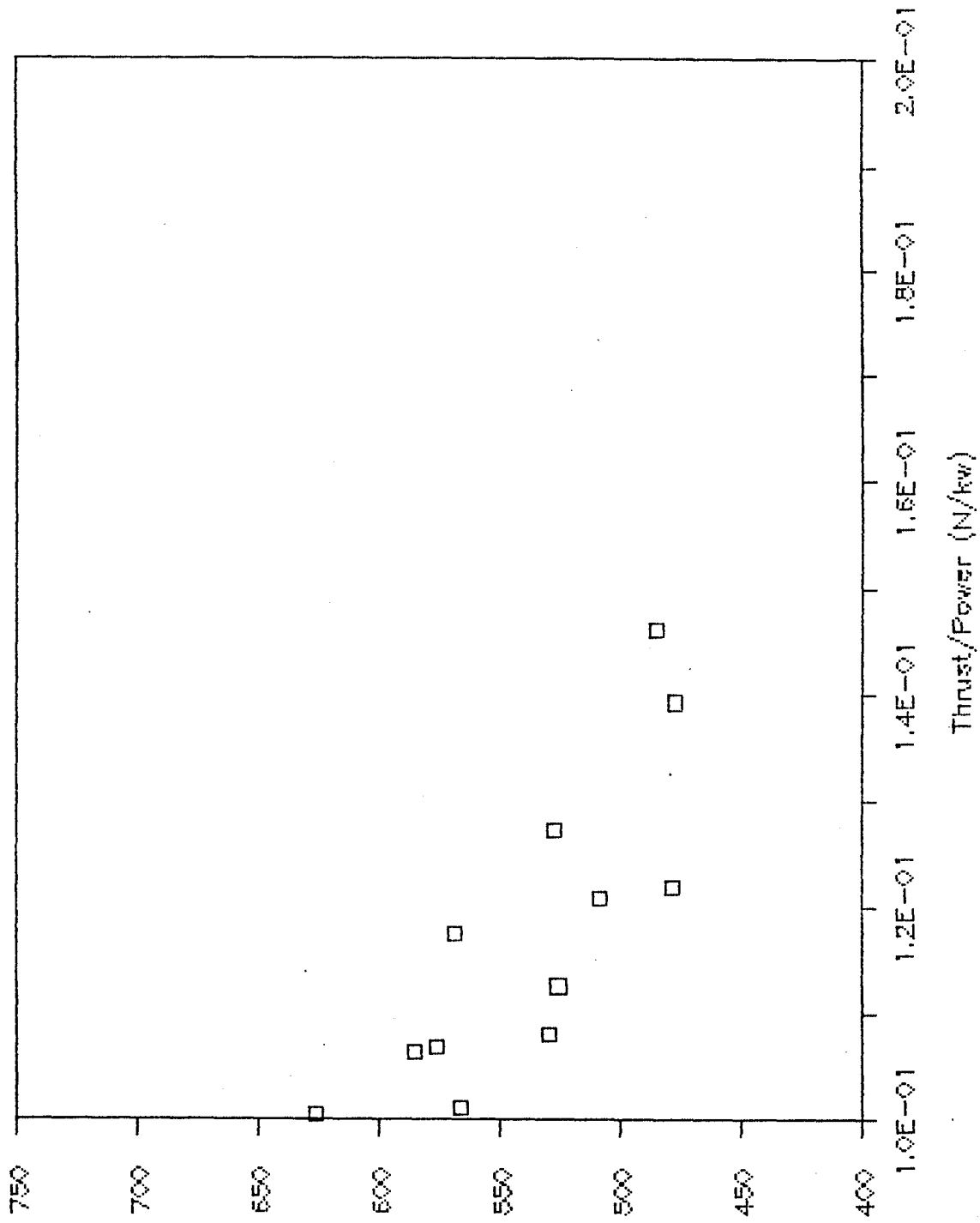


11-C-11
Thrust (N)

FIGURE C-7

Specific Impulse vs. Thrust/Power

Test 10.2



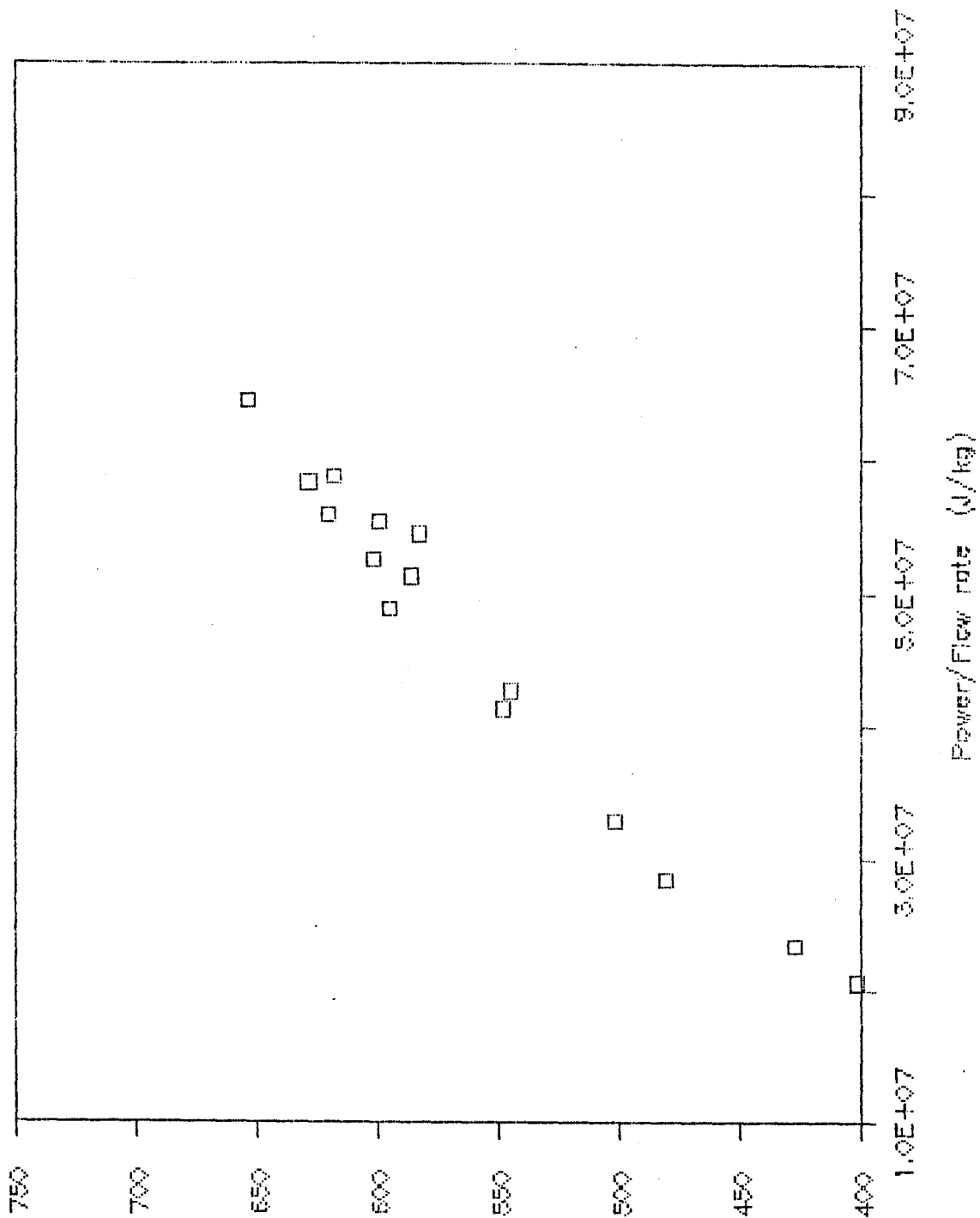
Specific Impulse (sec)

C-12

FIGURE C-8

Specific Impulse vs. Power/Mdot

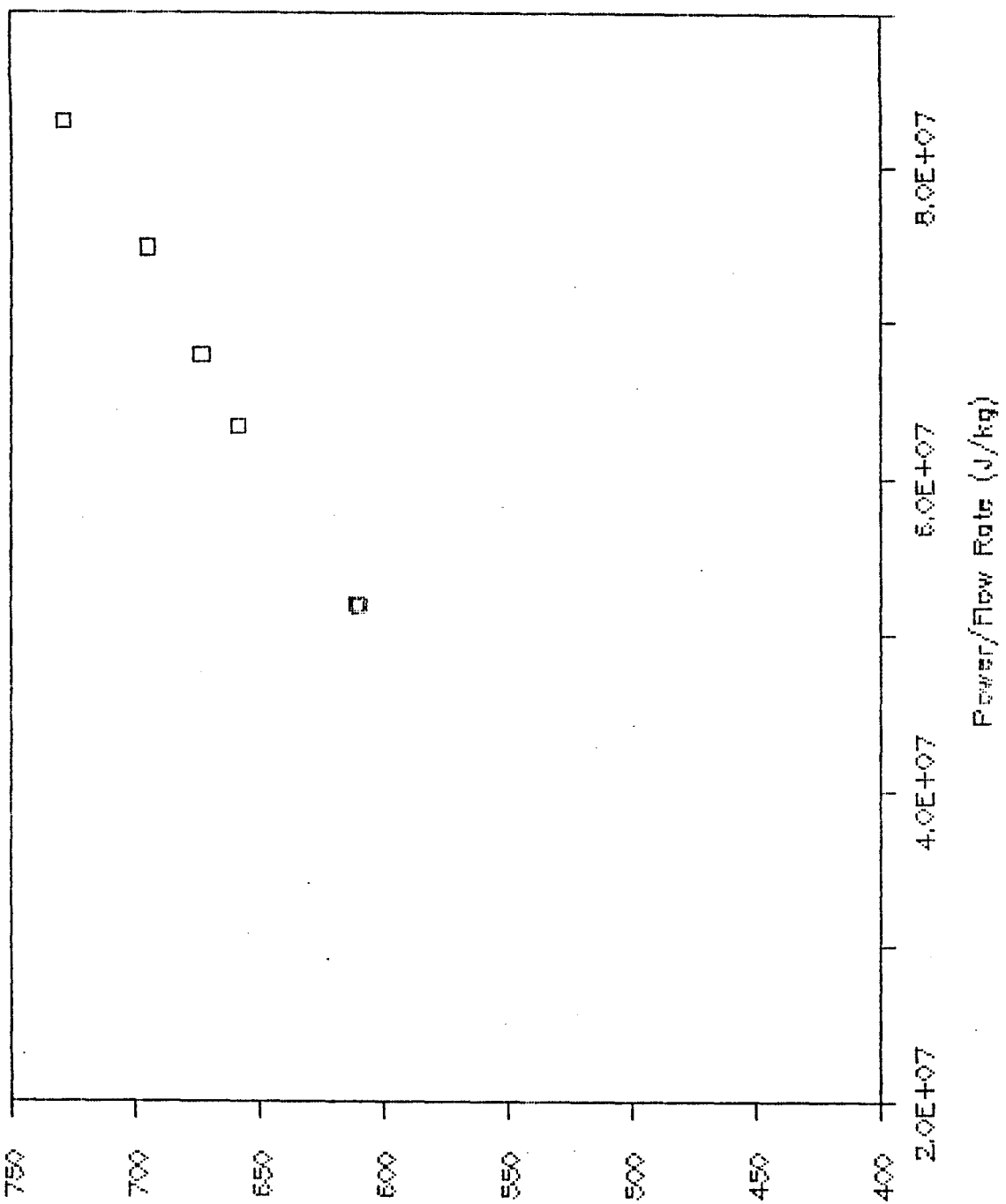
Test 12.1



Specific Impulse (sec)

Specific Impulse vs. Power/Flow Rate

Test 14.2

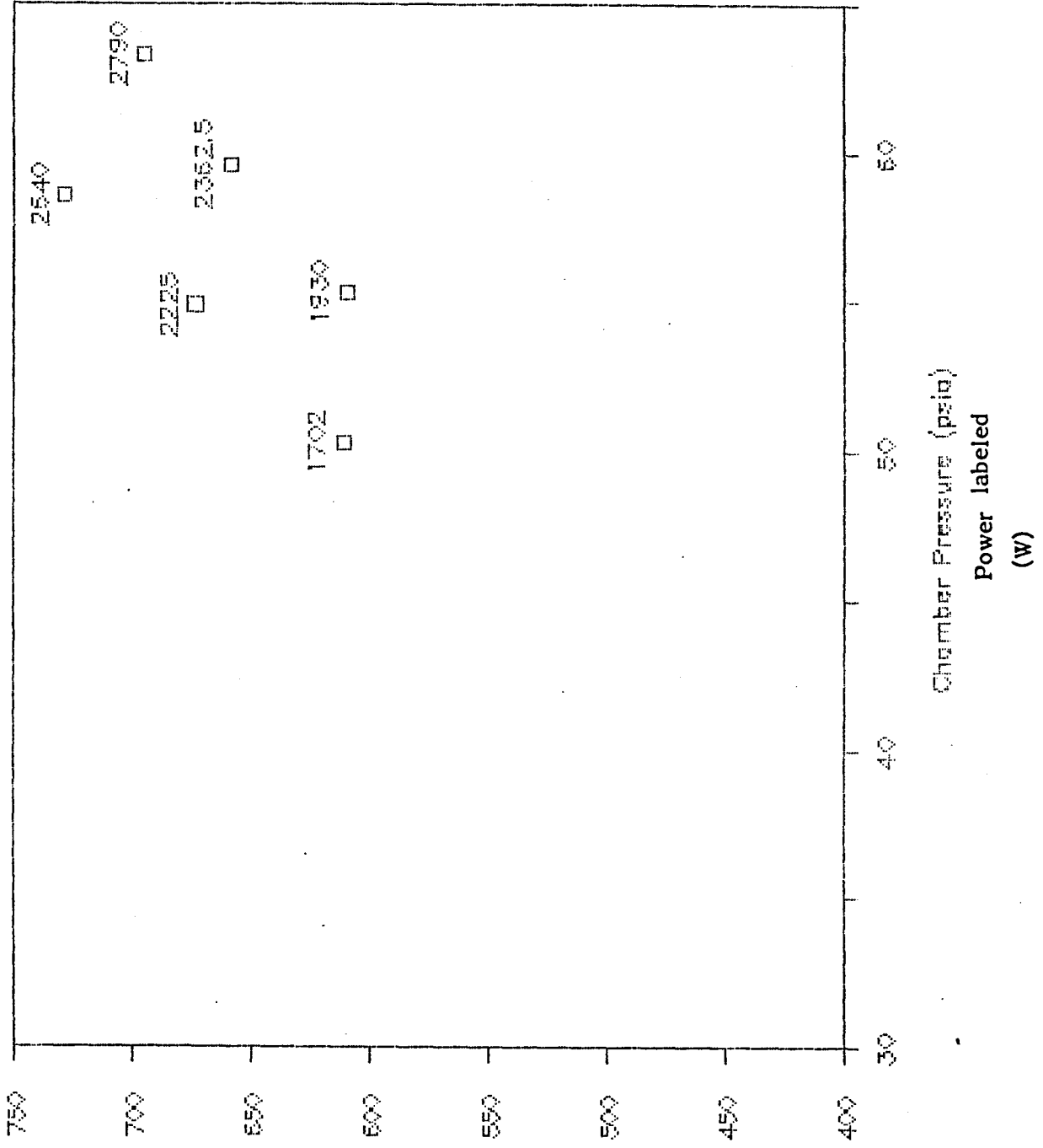


Specific Impulse (sec)
C-14

FIGURE C-10

Specific Impulse vs. Chamber Pressure

Test 14.2



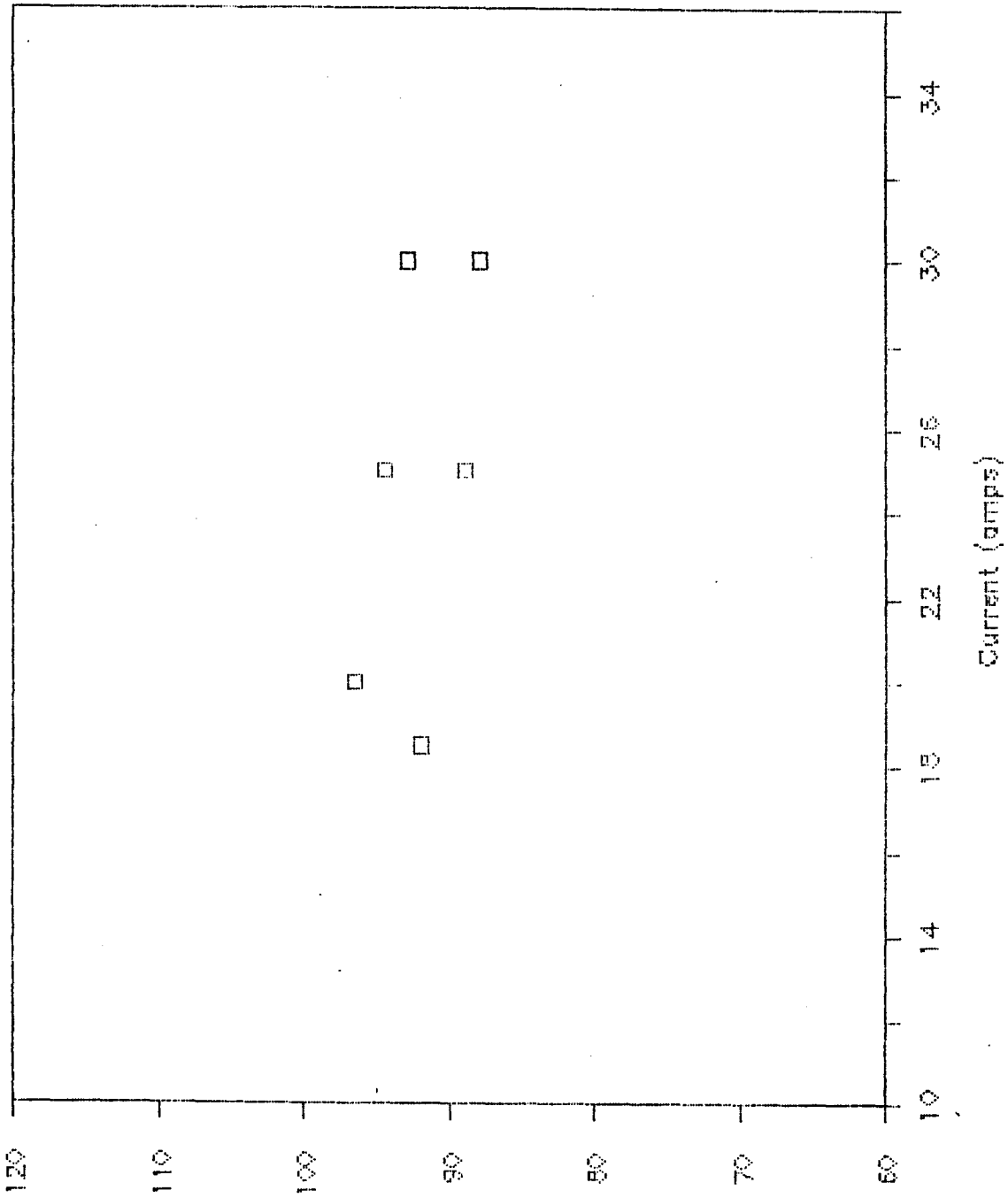
Specific Impulse (sec)

C-15

FIGURE C-11

Voltage vs. Current

Test 14.2



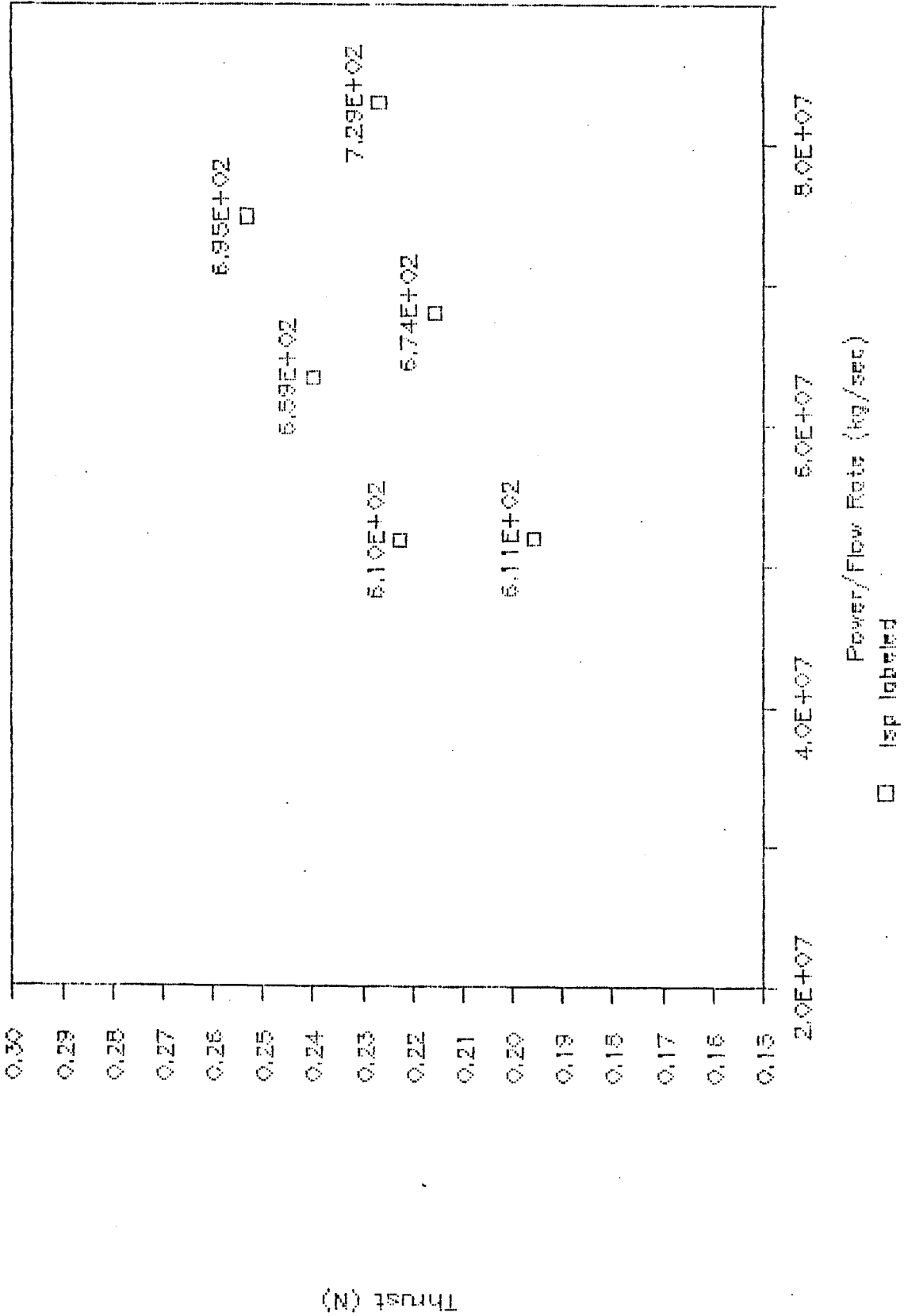
Voltage (V)

C-16

FIGURE C-12

Thrust vs. Power/Flow Rate

Test 14.2

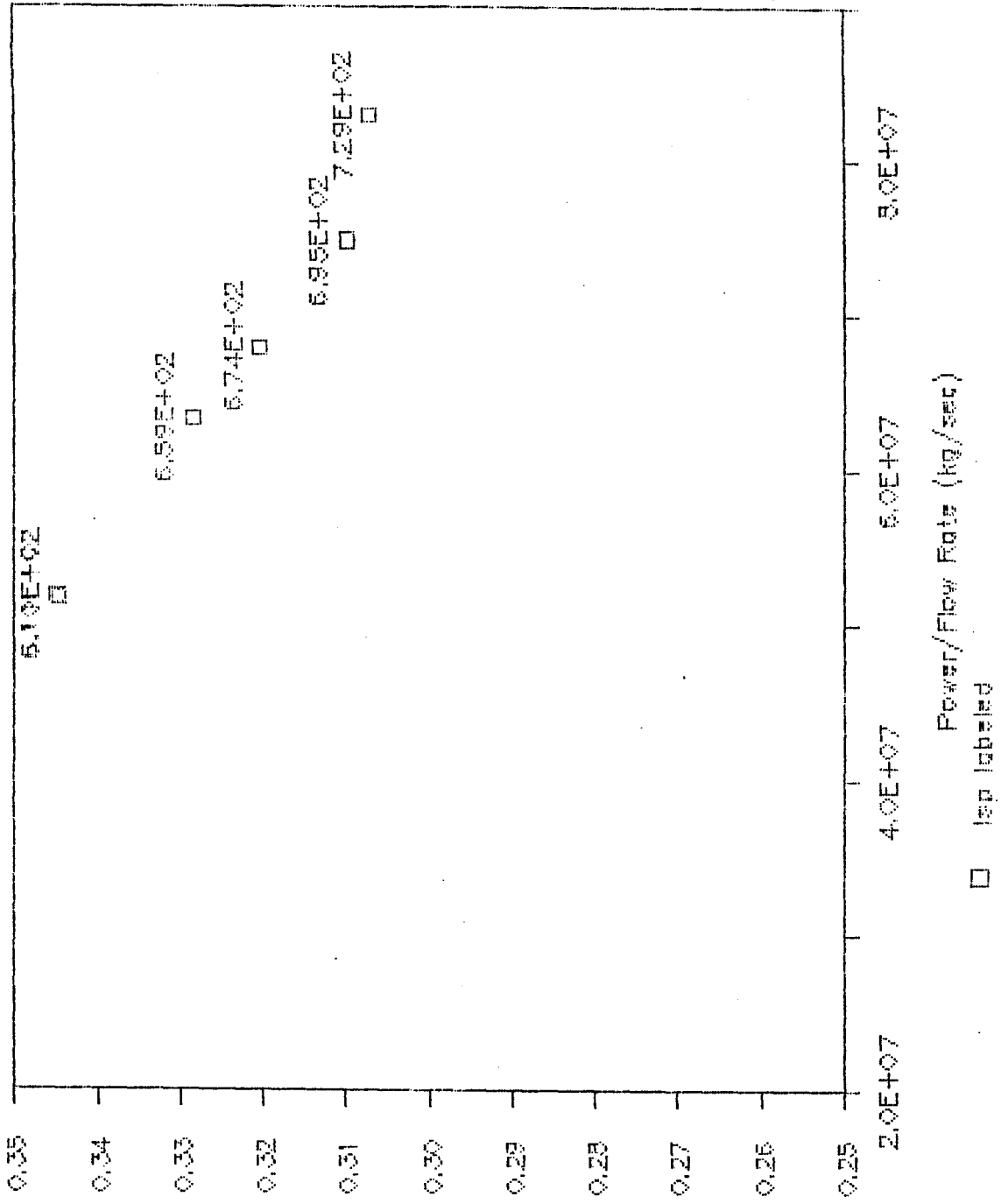


C-17
Thrust (N)

FIGURE C-13

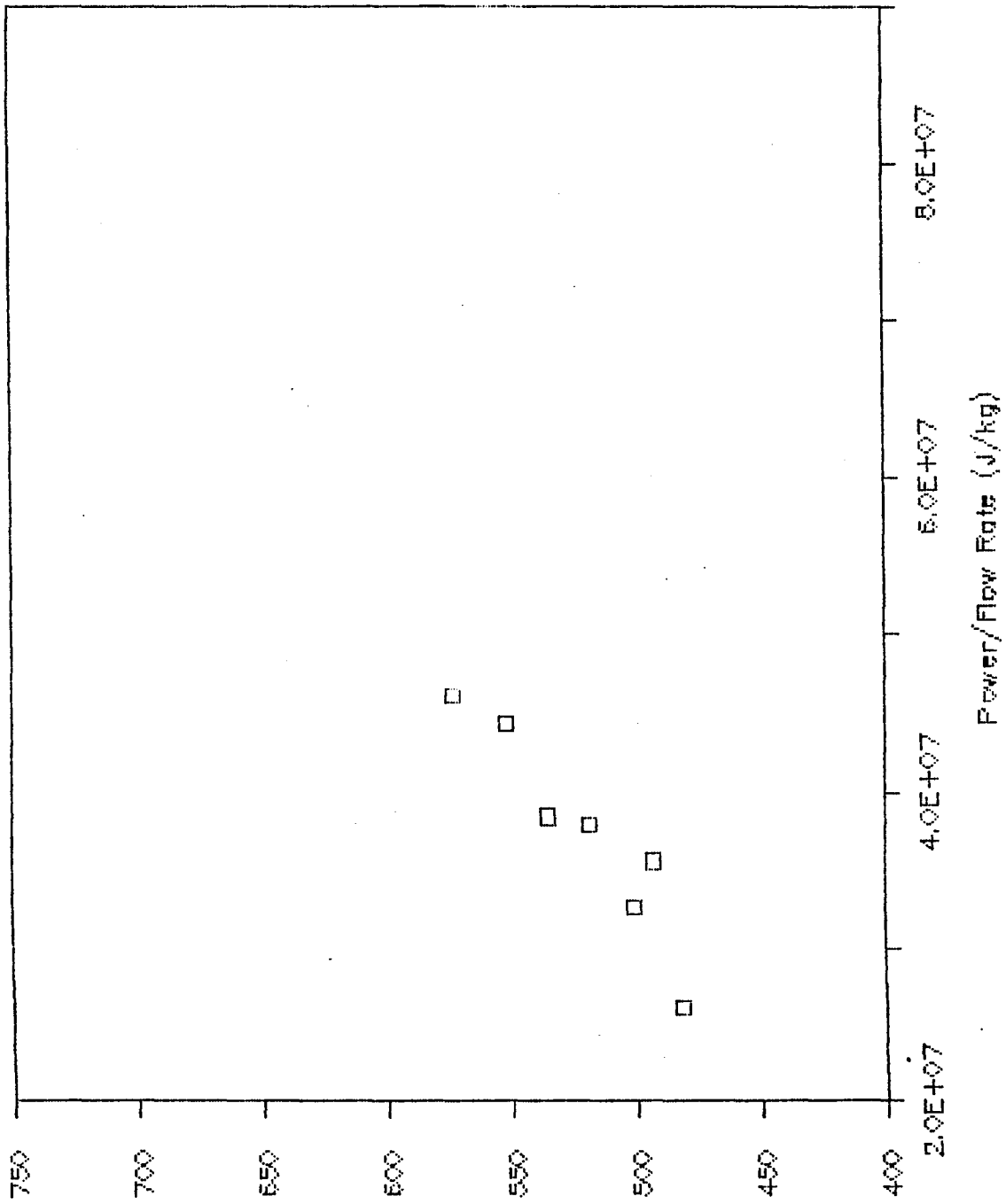
Efficiency vs. Power/Flow Rate

Test 14.2



Specific Impulse vs. Power/Flow Rate

Test 16.2



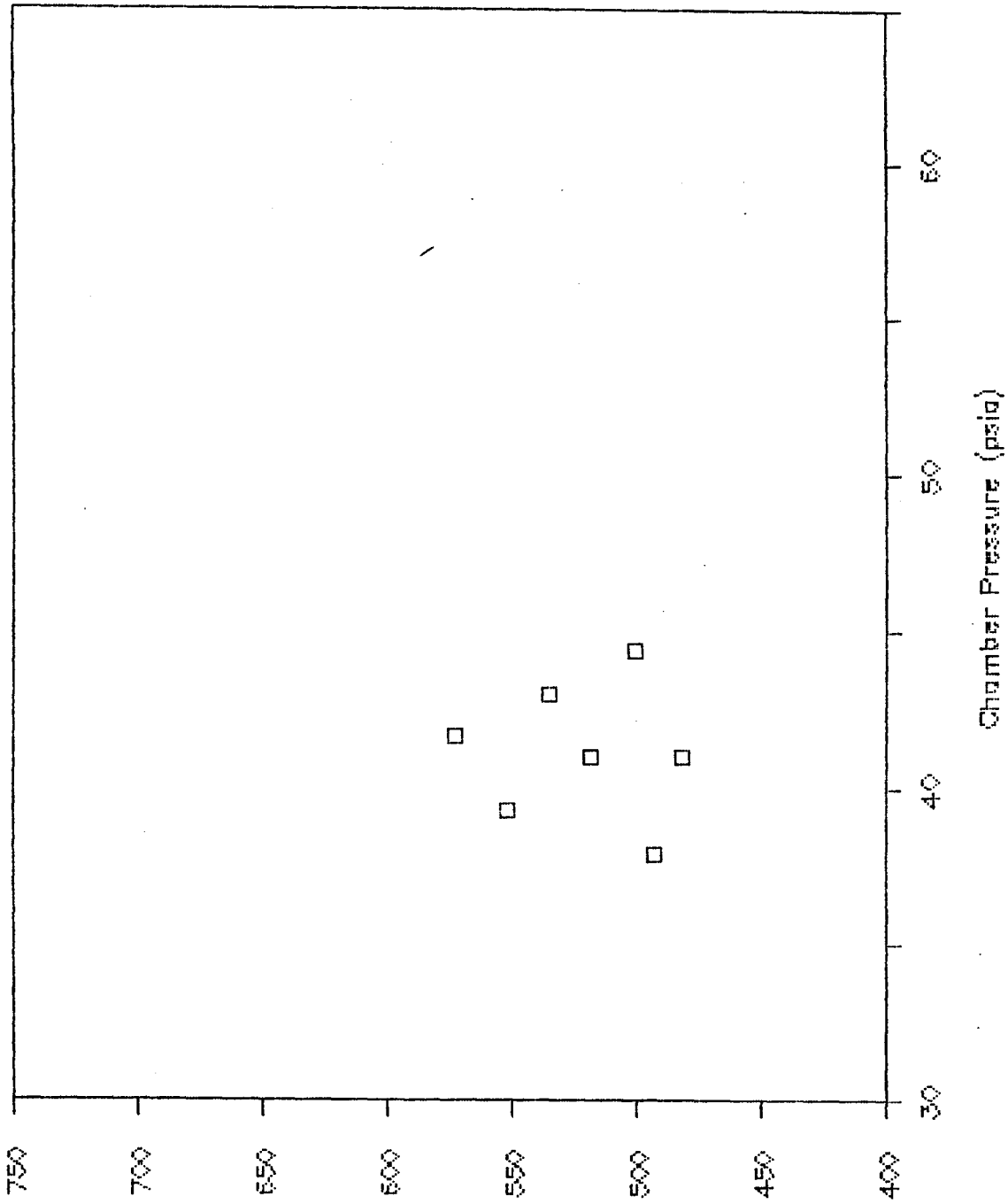
(sec) Specific Impulse

C-19

FIGURE C-15

Specific Impulse vs. Chamber Pressure

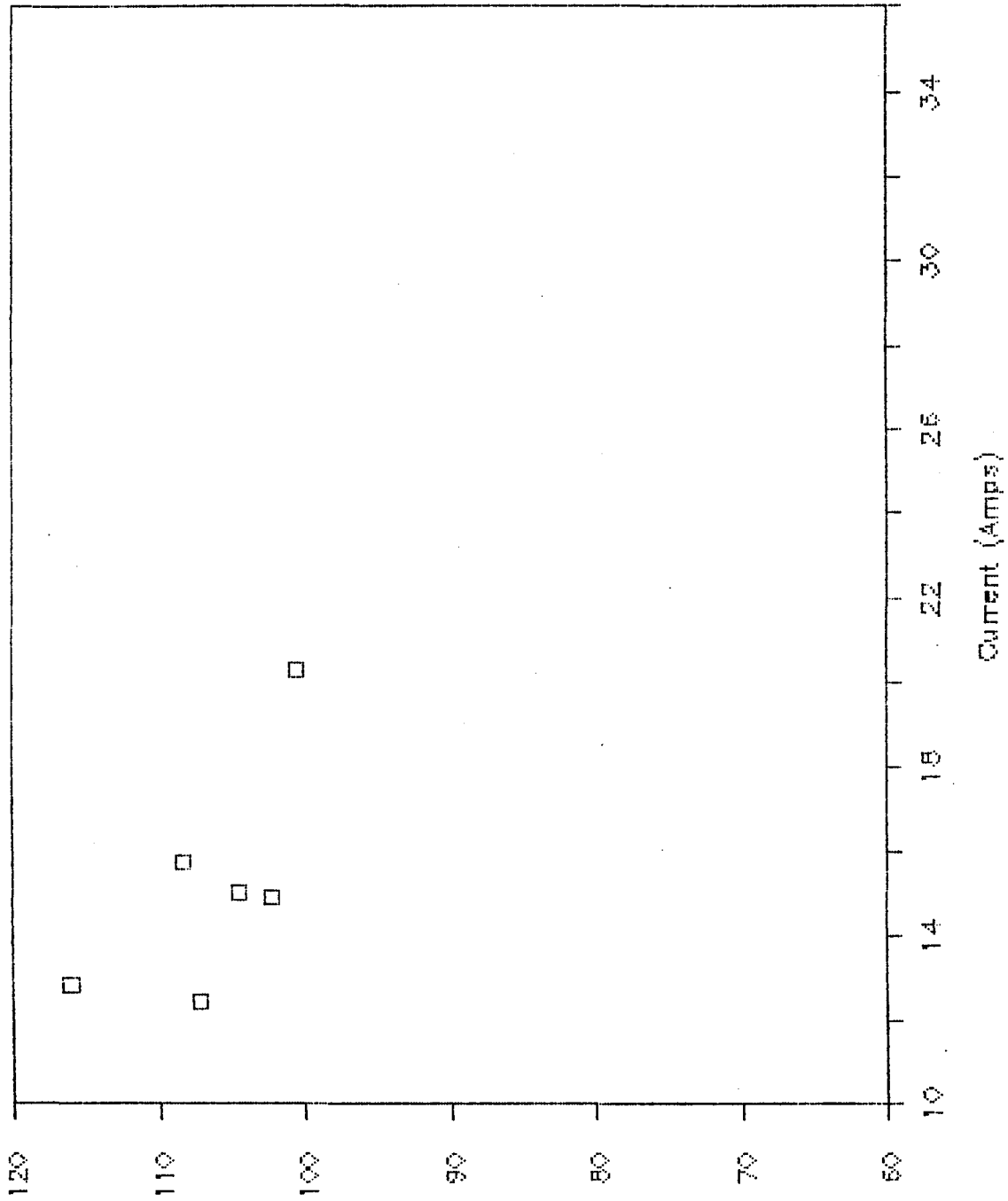
Test 16.2



Specific Impulse (sec)

Voltage vs. Current

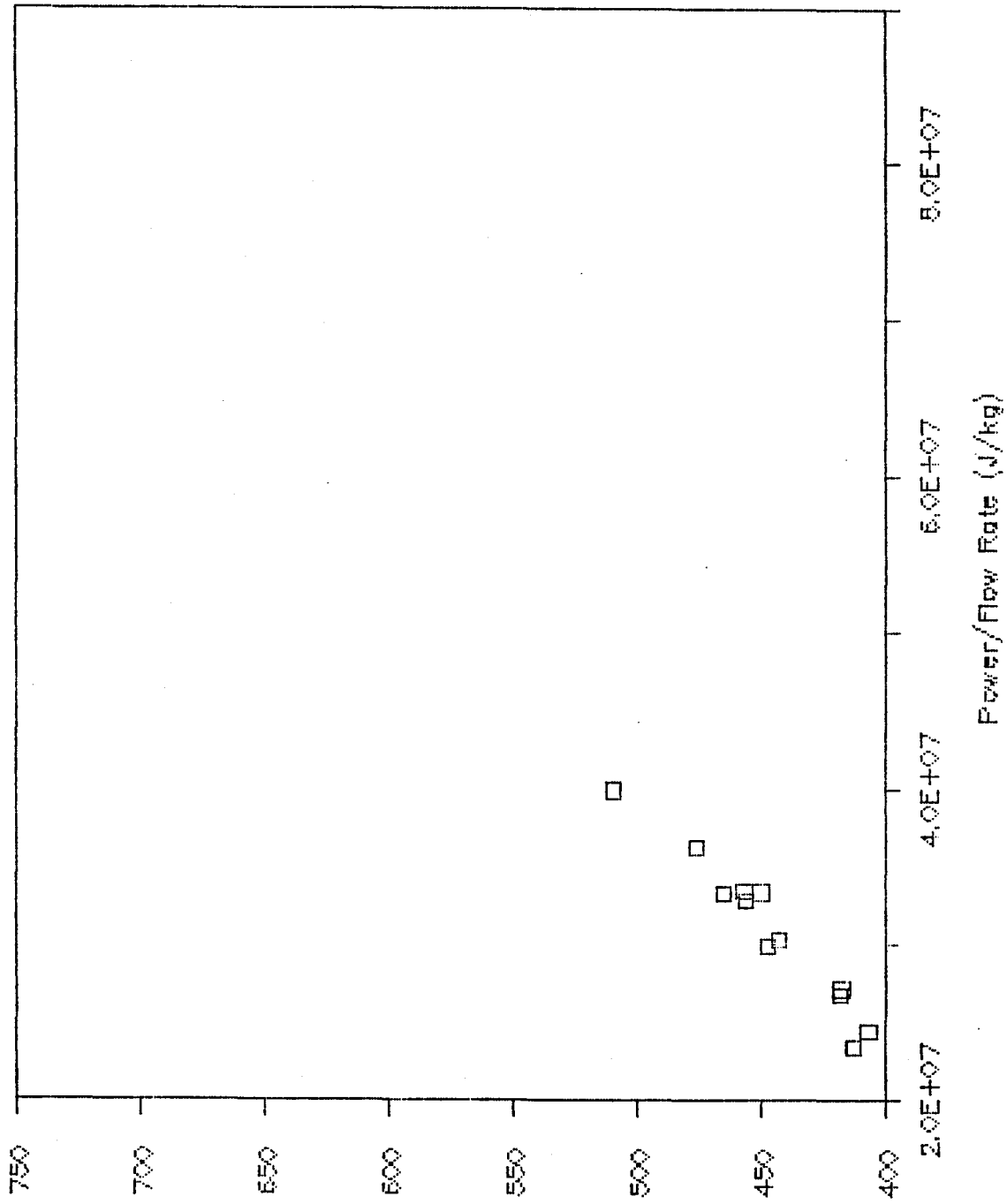
Test 16.2



Voltage (V)

Specific Impulse vs. Power/Flow Rate

Test 17.1

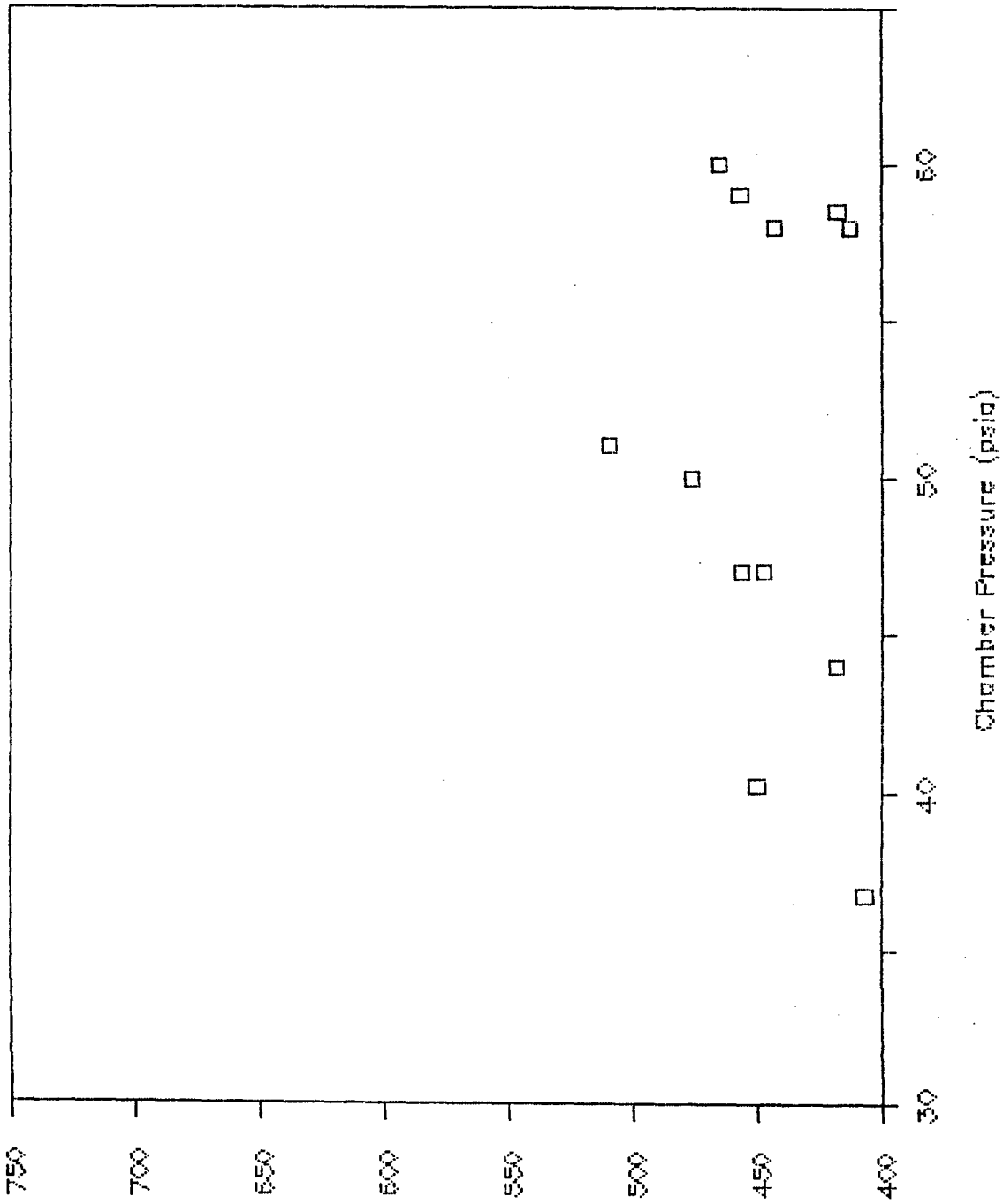


Specific Impulse (sec)

FIGURE C-18

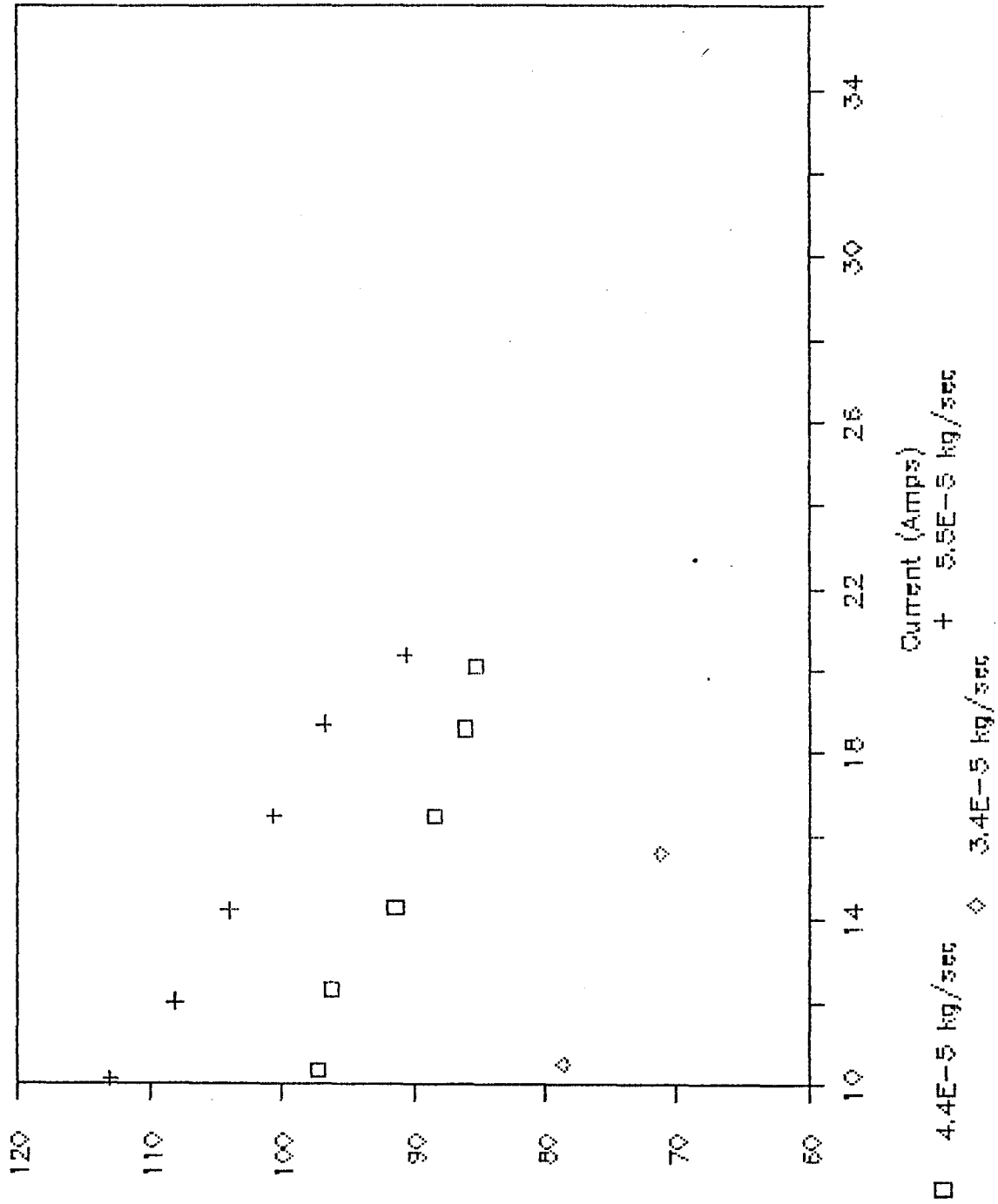
Specific Impulse vs. Chamber Pressure

Test 17.1



Voltage vs. Current

Test 17.1



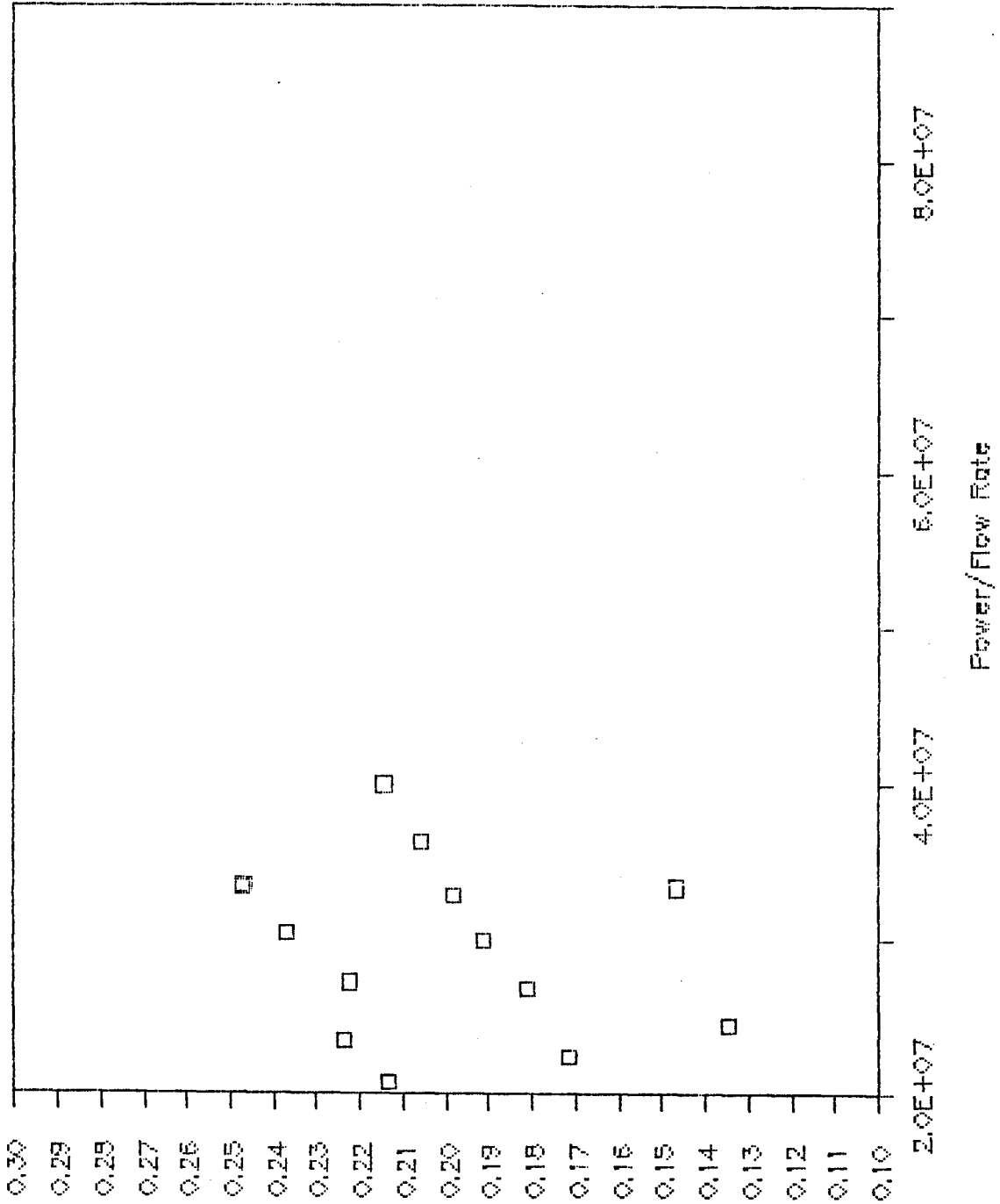
Voltage (V)

C-24

FIGURE C-20

Thrust vs. Power/Flow Rate

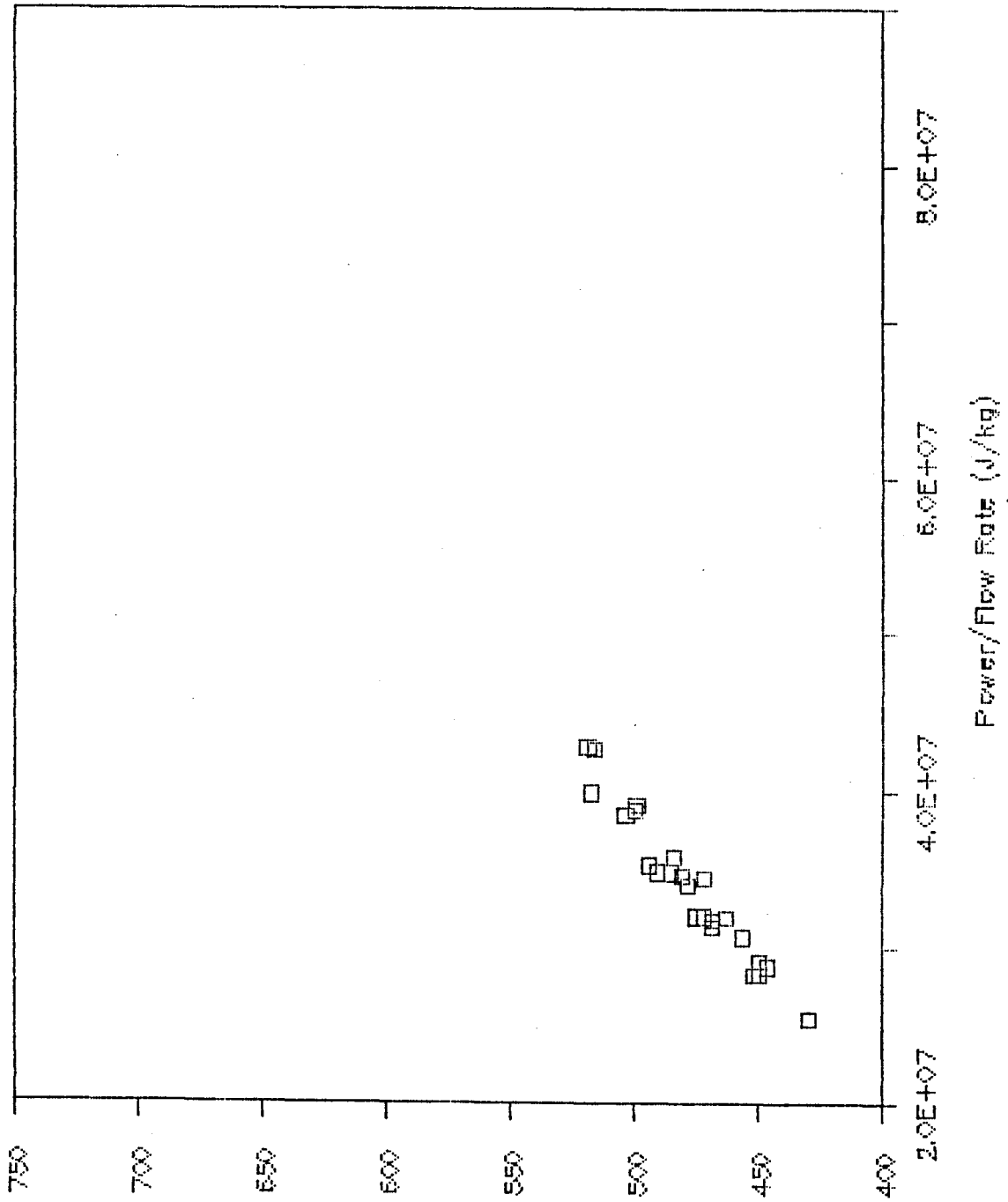
Test 17.1



Thrust (N)

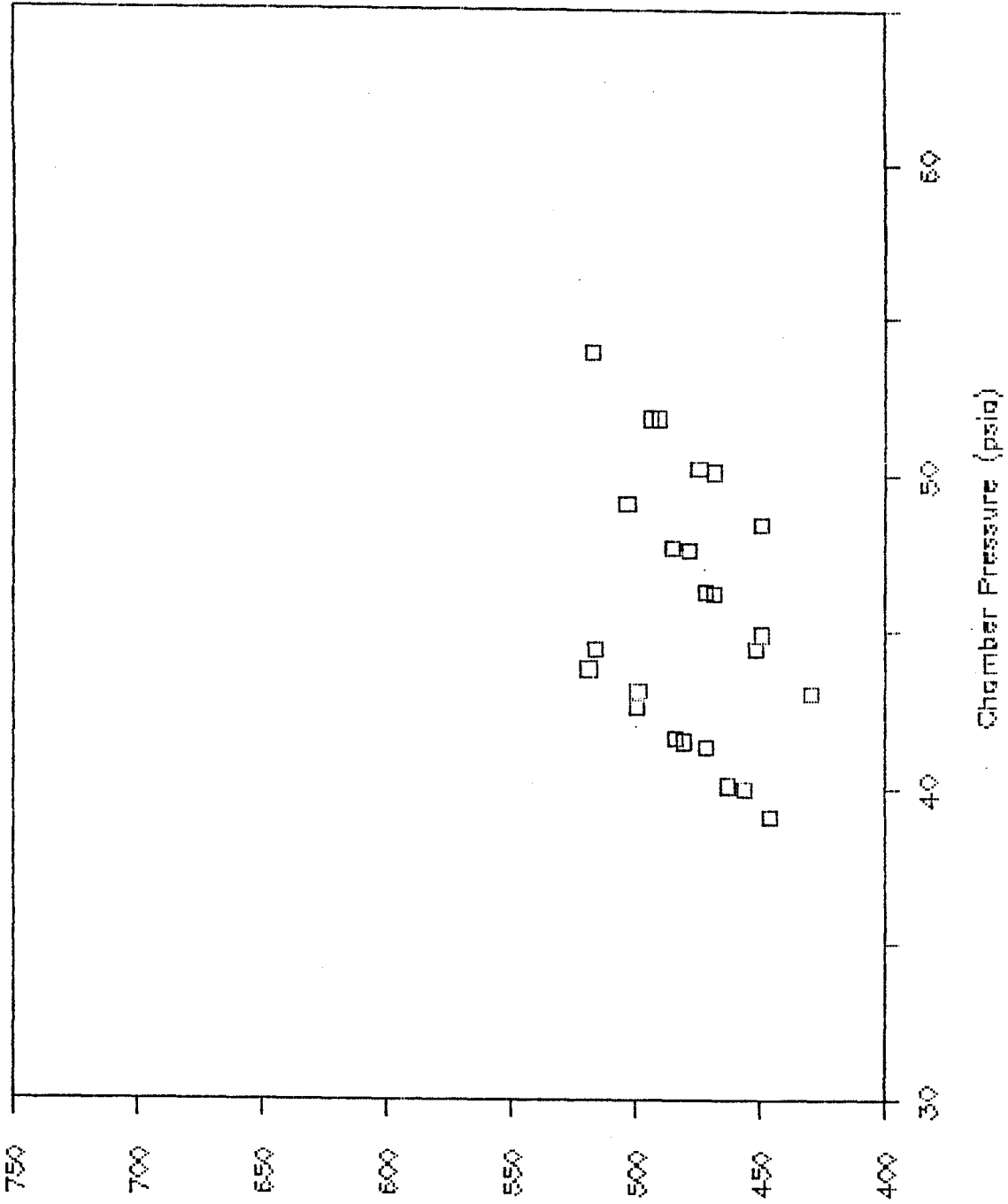
Specific Impulse vs. Power/Flow Rate

Test 18.4



Specific Impulse vs. Chamber Pressure

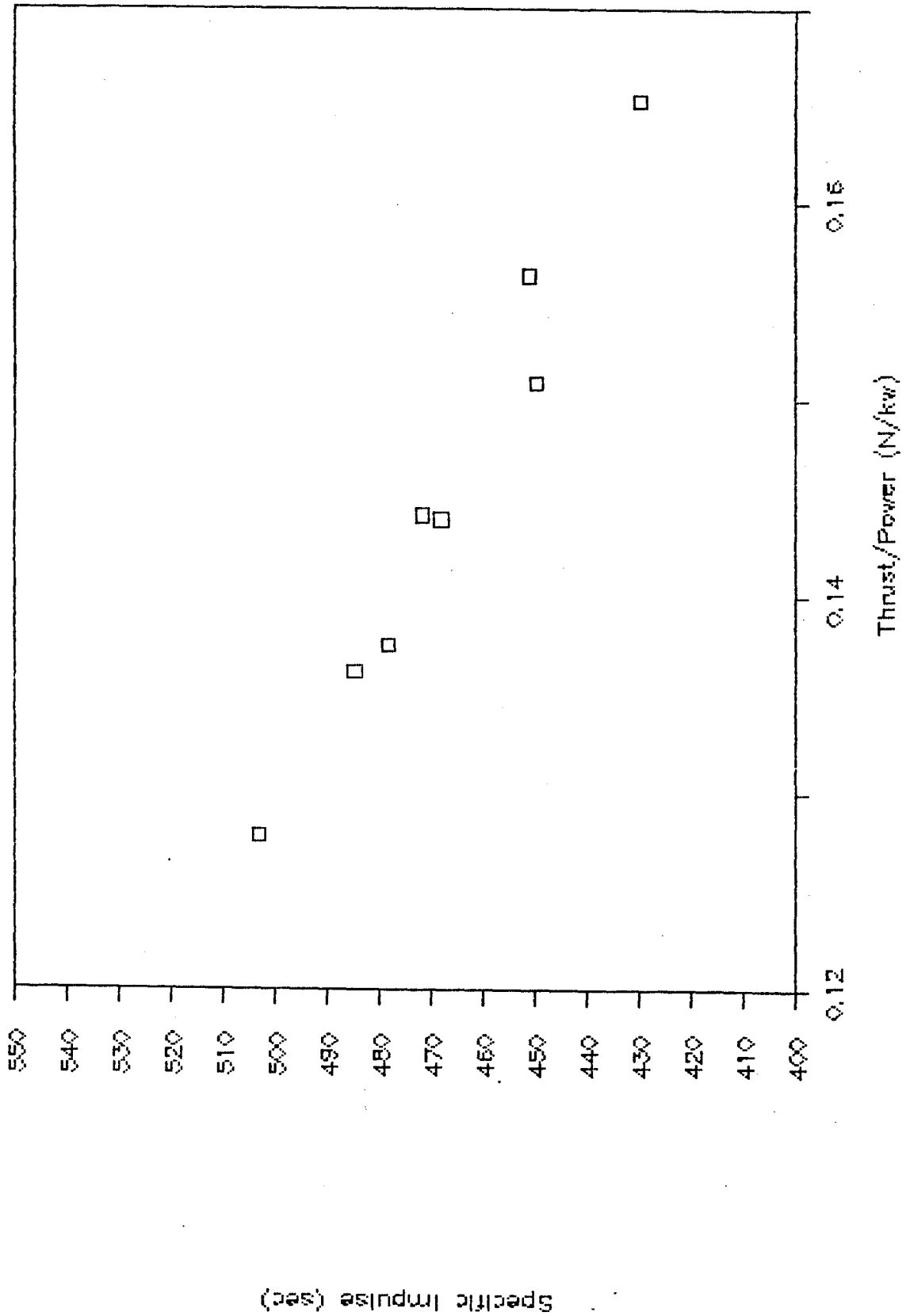
Test 18.4



Specific Impulse (sec)

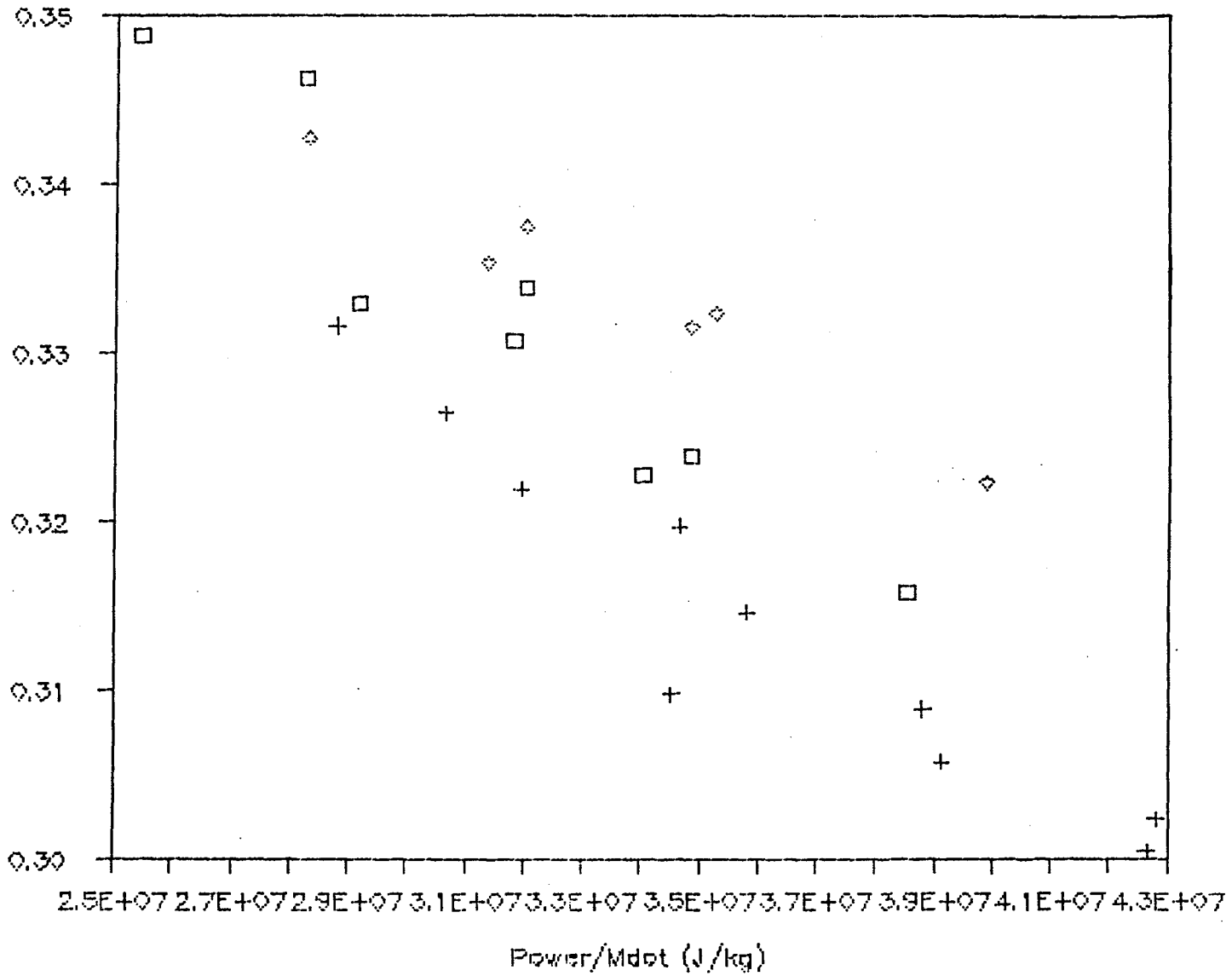
Specific Impulse vs. Thrust/Power

Test 18.4



Efficiency vs. Pow/Mdot

Test 18.4

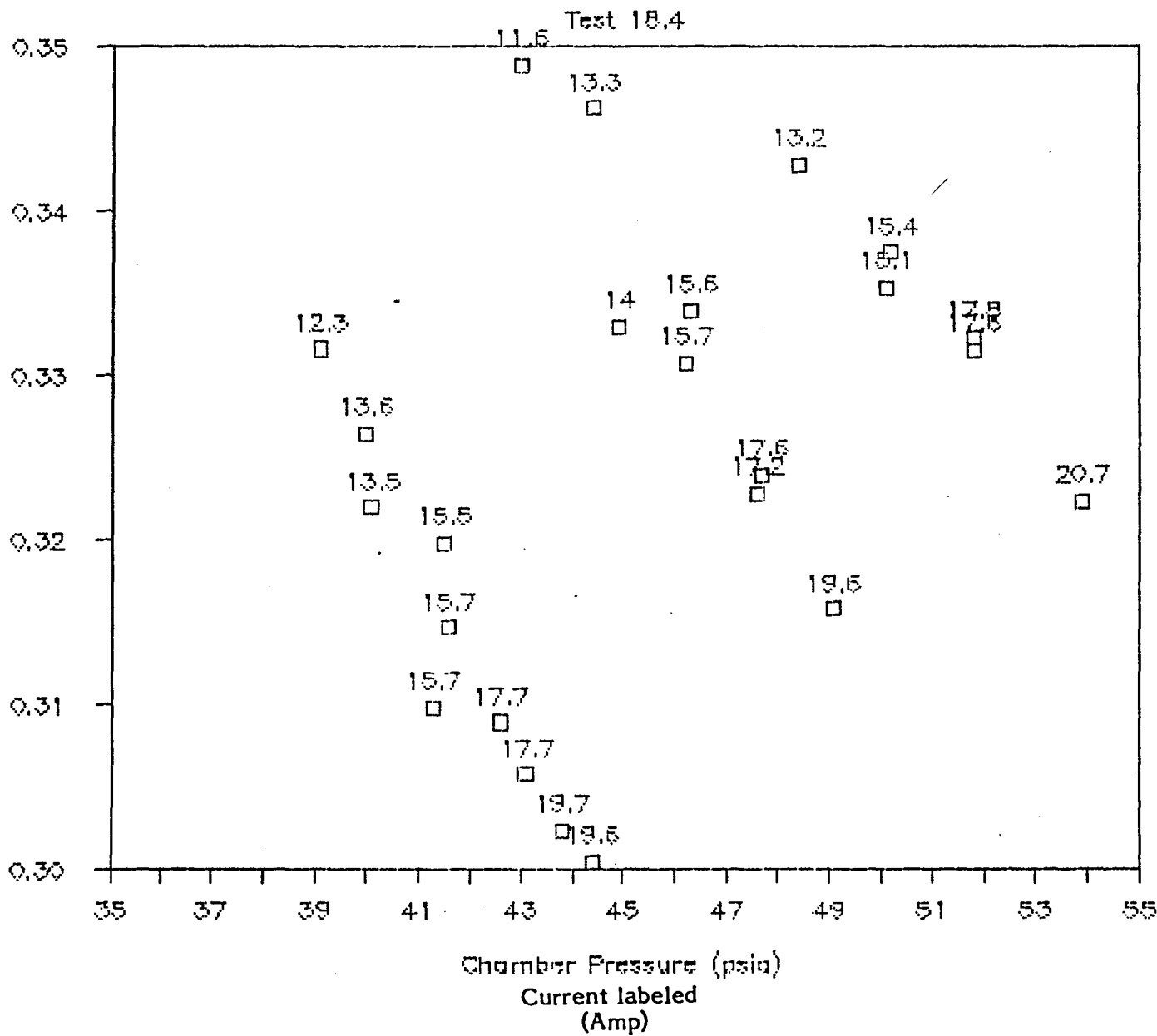


C-29

FIGURE C-25

Efficiency

Efficiency vs. Chamber Pressure

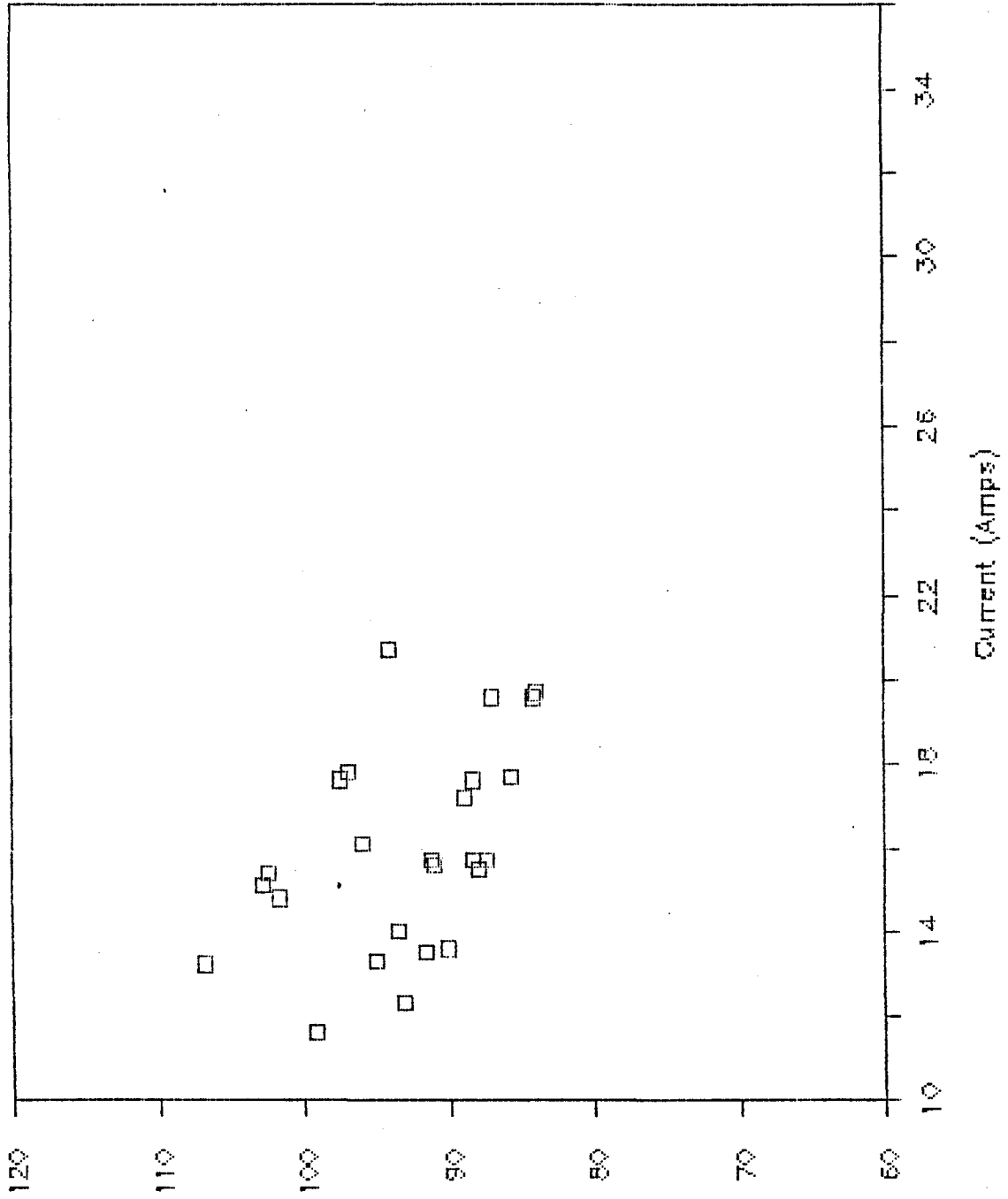


C-30
Efficiency

FIGURE C-26

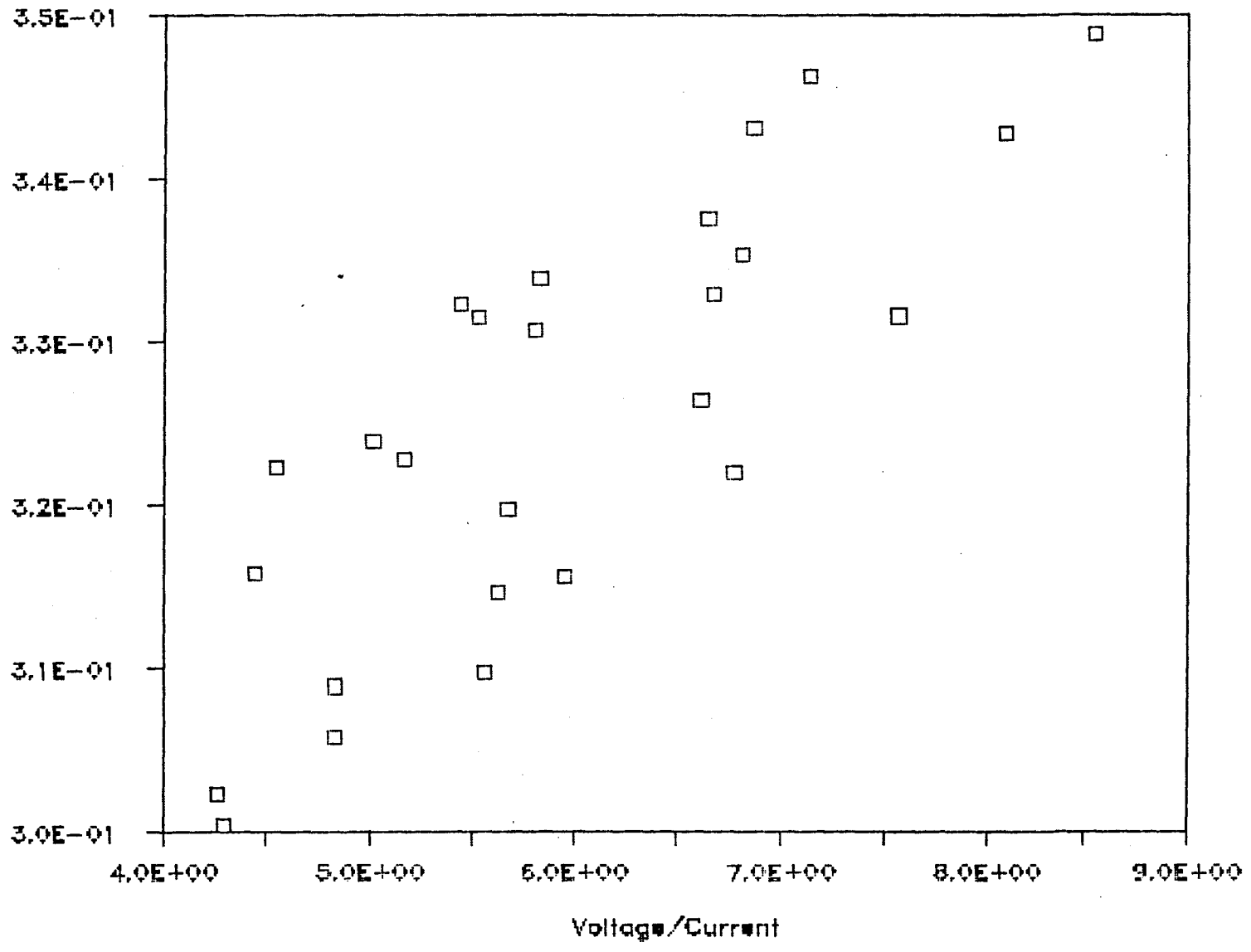
Voltage vs. Current

Test 18.4



Efficiency vs. V/I

Test 18.4

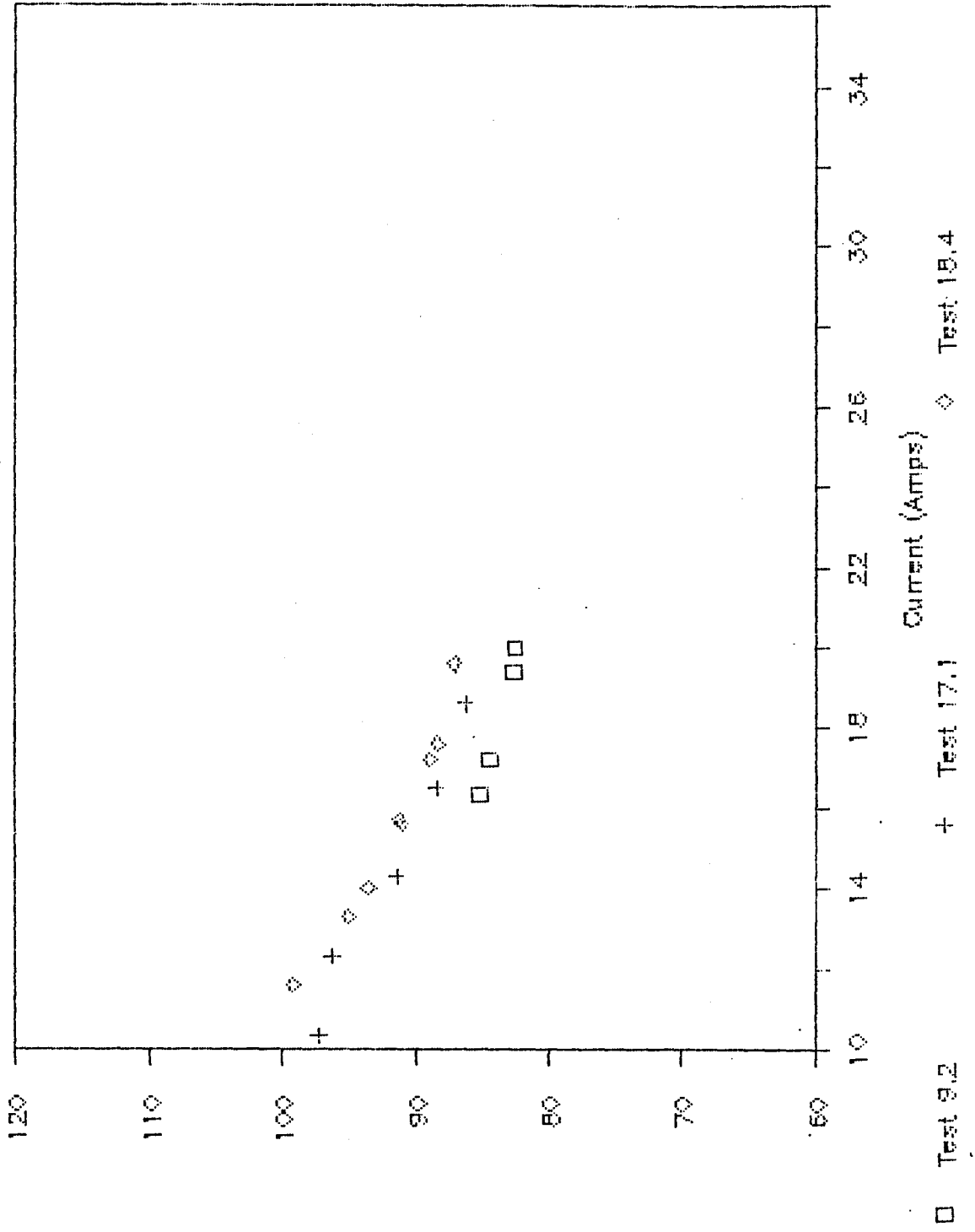


C-32
Efficiency

FIGURE C-28

Voltage vs. Current

Tests 9.2, 17.1, 18.4

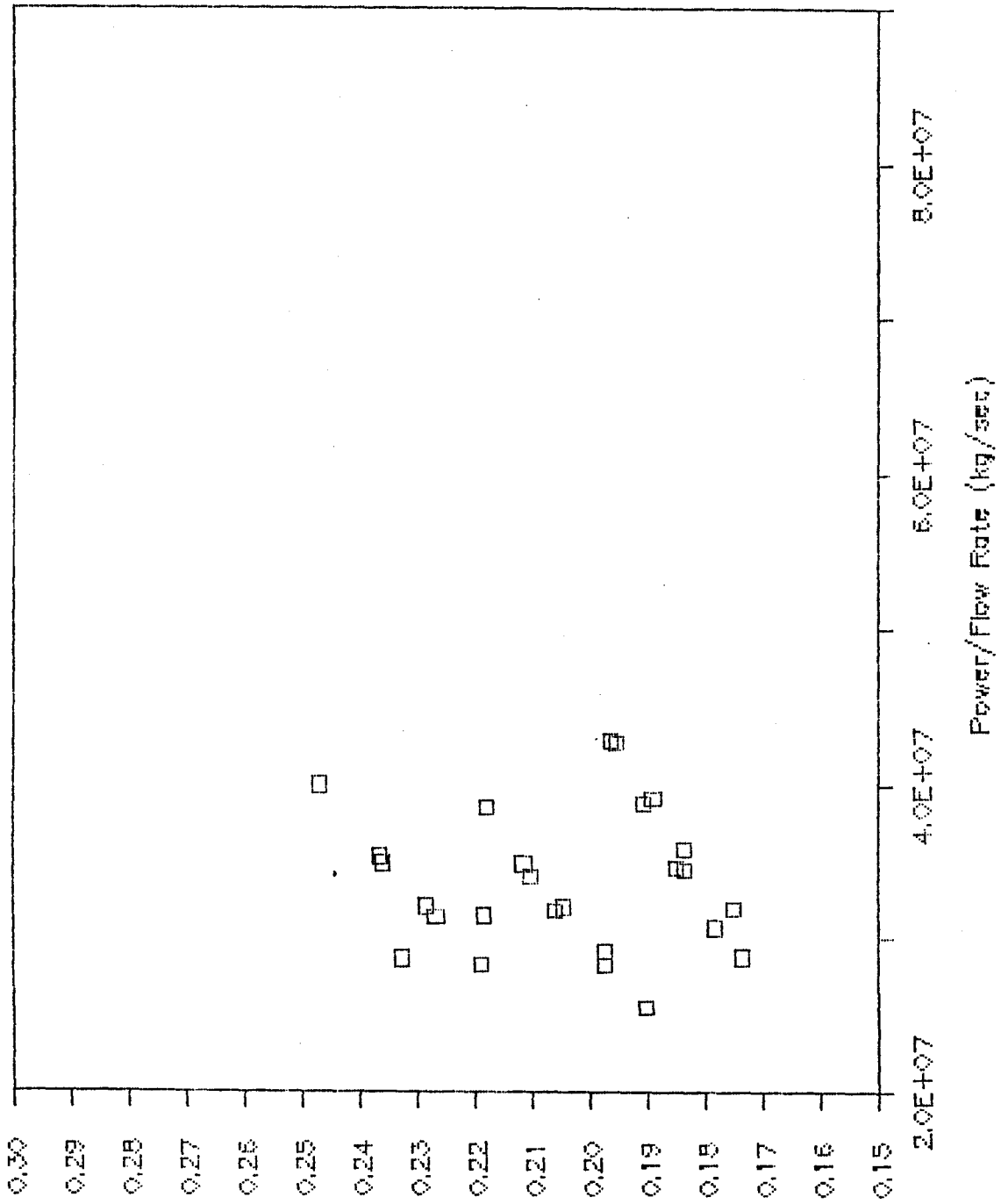


(A) Voltage (V)
C-34

FIGURE C-30

Thrust vs. Power/Flow Rate

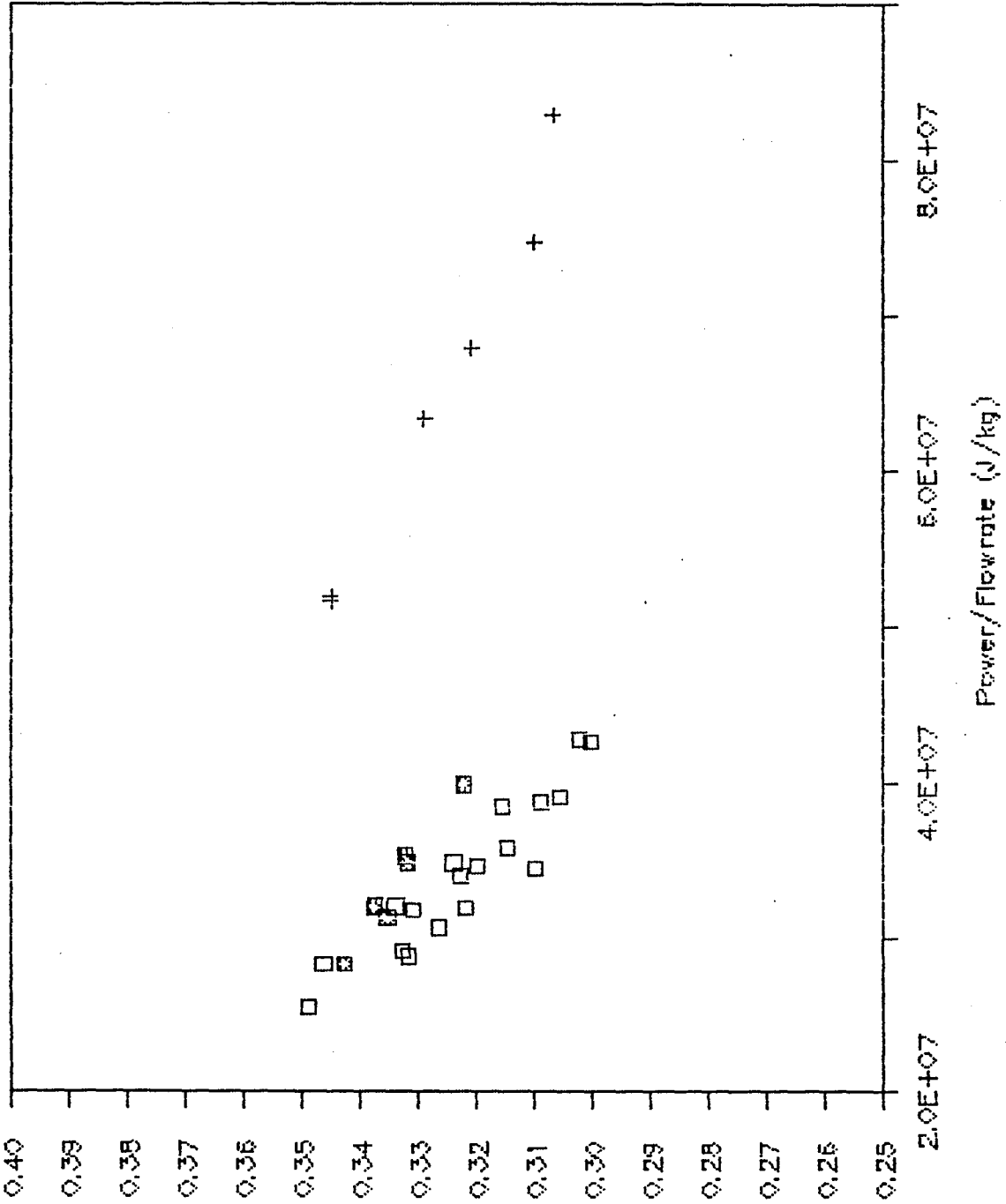
Test 18.4



Thrust (N)

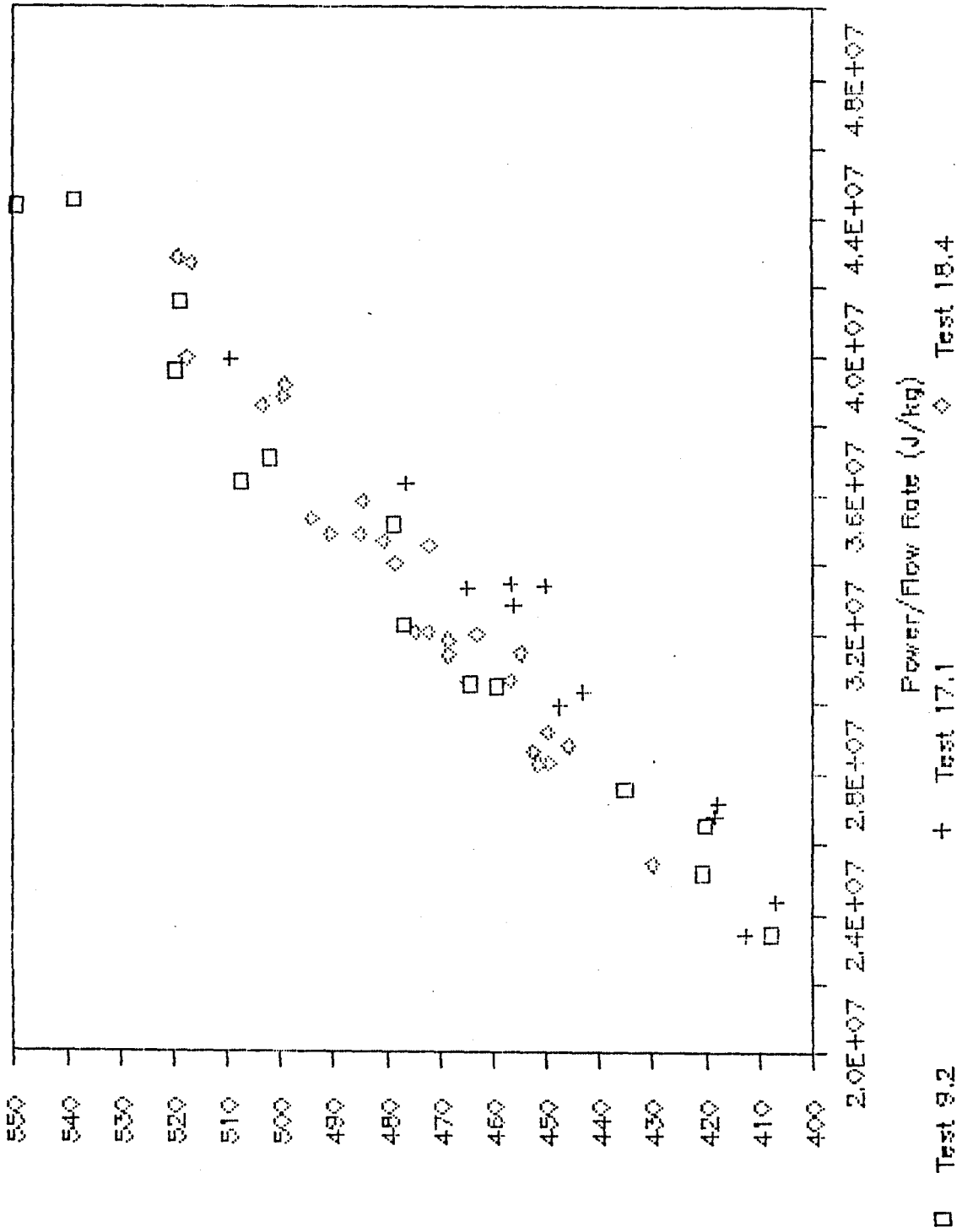
Efficiency vs. Power/Flowrate

Tests 14.2 & 18.4



Specific Impulse vs. Power/Flow rate

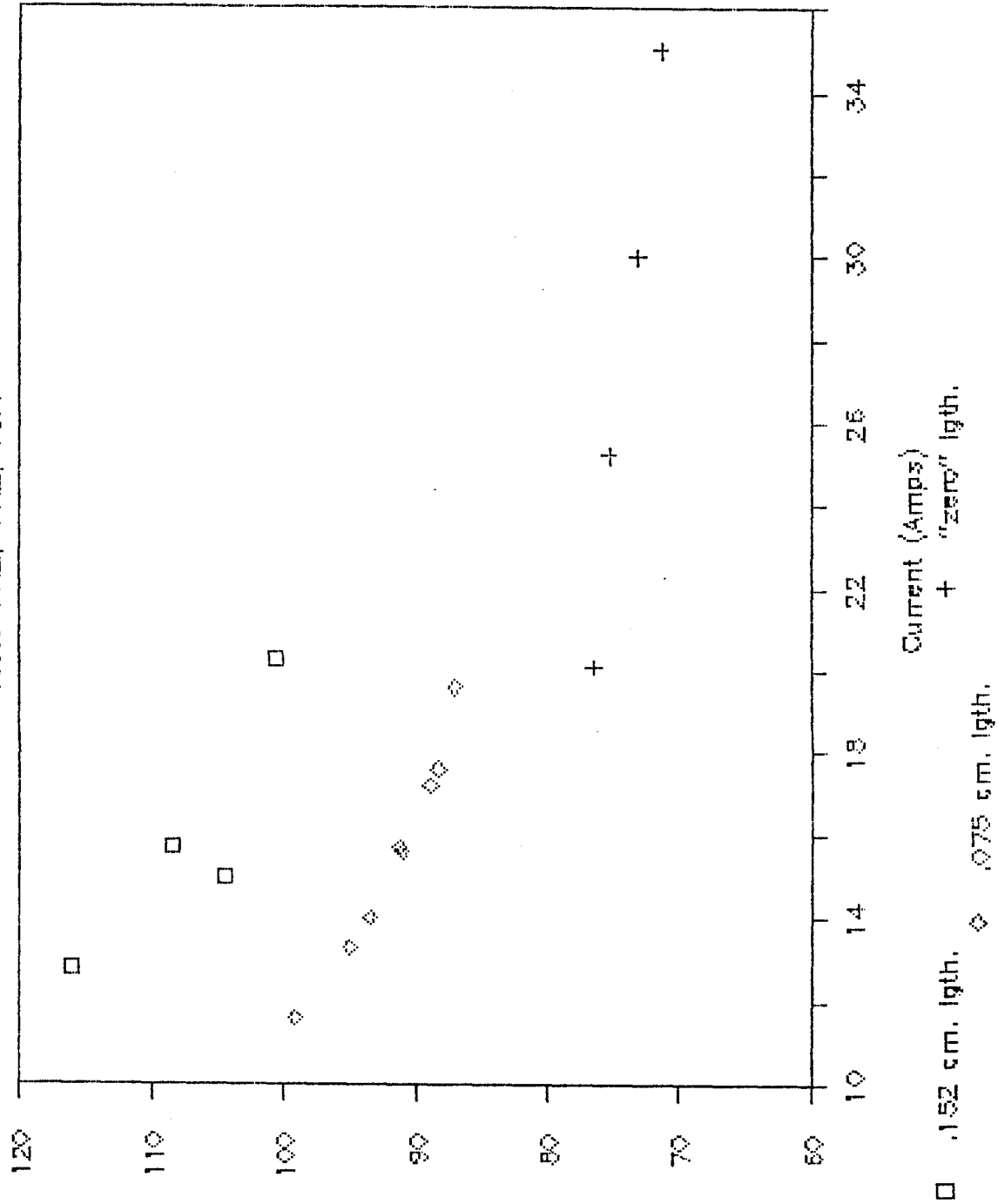
Tests 8.2, 17.1, 18.4



Specific Impulse (sec)

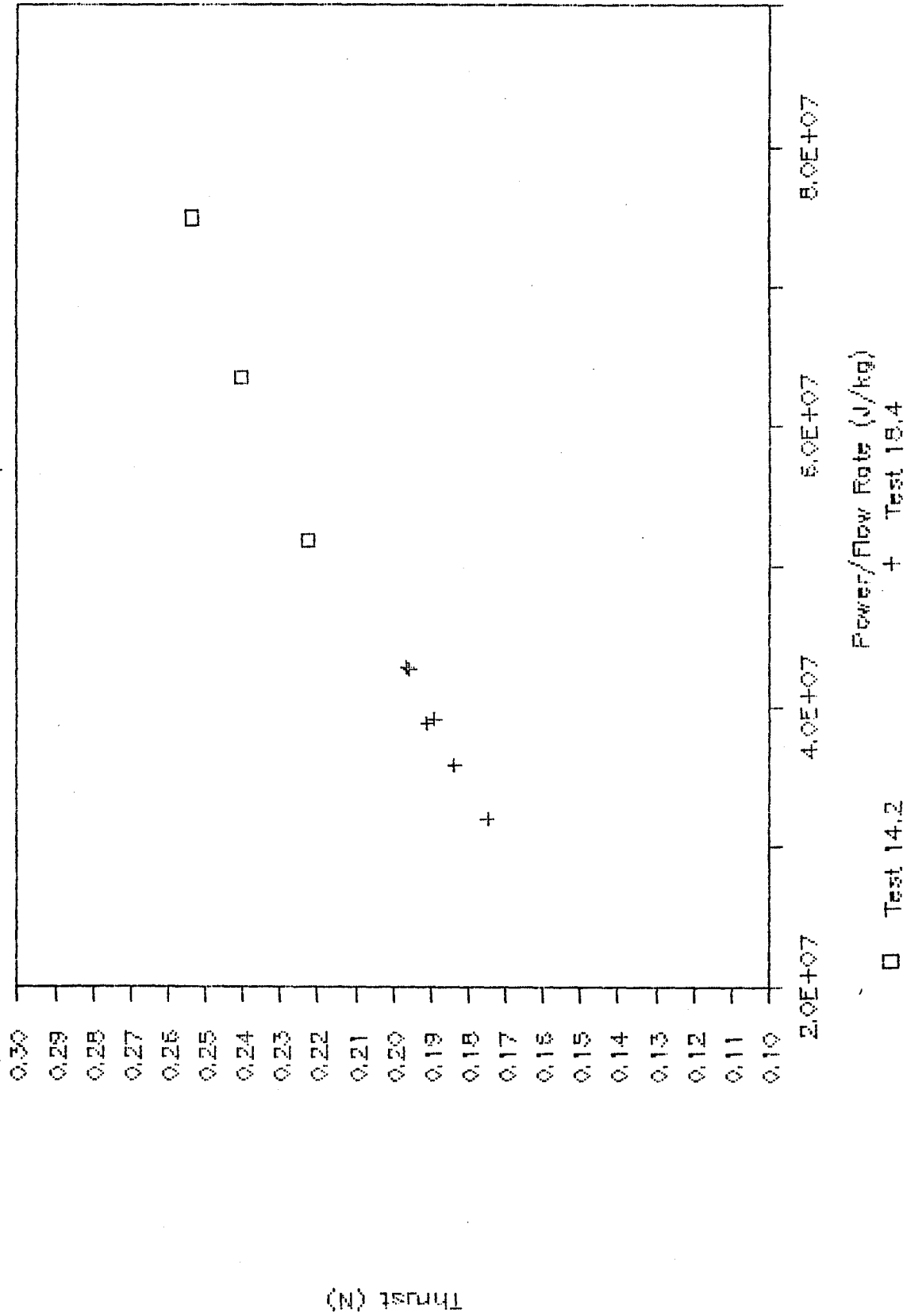
Voltage vs. Current.

Tests 10.2, 16.2, 18.4



Thrust vs. Power/Flow Rate

Test 14.2, 18.4



End of Document